Understanding HDL with Precision: From Isolation Methods to Structural and Functional Characterization

By

JINGYUAN ZHENG

DISSERTATION

Submitted in partial satisfaction of the requirements for the degree of

DOCTOR OF PHILOSOPHY

in

Nutritional Biology

in the

OFFICE OF GRADUATE STUDIES

of the

UNIVERSITY OF CALIFORNIA

DAVIS

Approved:

_____

Angela M. Zivkovic, Chair

_____

J. Bruce German

_____

Carlito B. Lebrilla

Committee in Charge

2024

Acknowledgement

My time in graduate school would not have been possible without the endless support and guidance from my mentor Dr. Angela M. Zivkovic. Thank you, Angela, for accepting my application and giving me an challenging and exciting project to work on, for going out of your way to support my skill development, and for exposing me to a greater world outside UC Davis. I would like to thank my colleagues in the Zivkovic lab, Brian V. Hong, Joanne K. Agus, Xinyu Tang, Eduardo Z. Romo, Susan Lei, Yanshan Jin, Betty Sun, and previous lab members Hannah E. Houts, Chenghao Zhu, Oscar Munoz and Jea Woo Kang. Thank you for being wonderful friends and lab partners that were around me to provide help, ideas, and celebrations.

I would like to sincerely thank my dissertation committee members, Dr. J. Bruce German and Dr. Carlito B. Lebrilla. Thank you, Bruce, for your inspiring mentorship and guidance as early as my undergraduate years that literally shaped my research ideology. And thank you, Carlito, for the important tips and suggestions on my research proposal. I would also like to thank all the collaborators who played critical roles in my completion of the program. Dr. Fei Guo, Dr. Wyatt N. Vreeland and Dr. Dean C. Ripple. My projects would not exist without your help and guidance. In addition, I would like to thank all the people who were essential to my career path: Dr. Junai Gan, Reedmond Fong, Jodi Ensunsa, Dr. Carl Keen, Dr. Javier Ottaviani, Dr. Ji Peng, Dr. Ken Hilt, Dr. James Cullor, and Dr. Tony Zilong Tan.

Lastly, I would like to thank my family. My mother Xi Song, and my father Xiangqi Zheng, who had never given up on me during my most mischievous years and provided me unconditional support. I want to thank my dear partner Yiyun Liu, for her love and encouragement, and the joy and happiness she brings into my life.

Table of Contents

ABSTRACT

The purpose of this dissertation is to update the current methodology in understanding the function and structure of high-density lipoprotein (HDL), to describe improved methods for HDL isolation and deep-learning-assisted particle size measurement, and to show how HDL size and function alter in *in vitro* treatments with antioxidant carotenoids and environmental insults, as well as in clinical samples from study participants with Alzheimer's disease (AD), mild cognitive impairment (MCI), or normal cognition. The dissertation is dived into four chapters with the corresponding objectives:

1. The first chapter is a literature review on recent updates and advancement of methods in understanding HDL characteristics, including physical properties, biological functions, and metabolism.
2. The second chapter reports an improved method for HDL isolation using ultracentrifugation followed by size exclusion chromatography. The isolated HDL fractions were evaluated on yield and purity, showing high HDL recovery and low levels of protein markers that are not HDL-associated. HDL fractions isolated using this method were further analyzed for HDL-associated protein markers, and we identified specific HDL-associated proteins that have preference for HDL subpopulations of specific size ranges.
3. The third chapter reports experiments to evaluate HDL's size and functional alterations under direct treatment with lutein, zeaxanthin, oxidants ($CuSO_4$, H_2O_2, HOCl), glycation, fructosylation, glycosylation removal (*N*-glycan, sialic acid), or acidic pH, as well as HDL pre-treated with antioxidant carotenoids (lutein or zeaxanthin) and then treated with H_2O_2 oxidant. We showed that HDL functions,

including cholesterol efflux capacity (CEC), lecithin-cholesterol acyltransferase (LCAT) activity, and paraoxonase-1 (PON1) activity were altered by the treatment. Pre-incubating HDL with lutein attenuated the negative effects on HDL function caused by H_2O_2 treatment.

4. The fourth chapter reports an innovative method to use transmission electron microscopy followed by deep-learning-assisted particle detection for HDL particle size measurement of isolated HDL particles. The method showed improved precision and repeatability compared to a common image analysis software ImageJ on the specific task of HDL particle size measurement. We further use the method to characterize HDL particle size distribution from a large-scale data set from 183 study participants with AD, MCI, or normal cognition (age matched) and discovered a specific shift of HDL size from large to small in participants with dementia, with *APOE* genotype-dependent effects.

Chapter 1: Methodology Advancement in Understanding HDL Characteristics

Jingyuan Zheng[a], Brian V. Hong[a], Angela M. Zivkovic[a]

[a] Department of Nutrition, University of California, Davis, CA. U.S.A. 95616

1. ABSTRACT

While the association between high density lipoprotein (HDL) cholesterol concentrations and disease risk has been a focus for decades, emerging evidence suggests that HDL's physical properties, biological functions, and compositional makeup play crucial roles in disease development. This review paper synthesizes the latest advancements in understanding HDL through various methods. Methods such as transmission electron microscopy (TEM), atomic force microscopy (AFM), and 2-dimensional gel electrophoresis (2DGE) have elucidated the diverse sizes and shapes of HDL particles, providing insights into their structural characteristics and functional implications. Advancements in measuring HDL's biological functions, including cholesterol efflux capacity (CEC), antioxidant properties, and inflammatory index (HII), have offered insights for clinical assessment and risk prediction. Novel assays like nanoparticle-based probes and cell-free assays show potential for enhancing our understanding of HDL's dynamic metabolism and its role in disease pathogenesis. By integrating physical and functional, a multidisciplinary approach is essential for a comprehensive understanding of HDL biology.

2. INTRODUCTION

The prevalent consumption of high-fat, high-cholesterol, high-sugar diets - commonly referred to as Western-type diets - is linked to an increased risk for chronic metabolic diseases, especially in genetically susceptible individuals. The links between Western-type diets and disease risk have been shown to be associated with high-density lipoprotein (HDL) cholesterol concentrations. Epidemiological studies have shown an inverse relationship between HDL cholesterol and adverse cardiovascular events [1–3], type 2 diabetes [4], cancer [5,6], Alzheimer's disease [7], and kidney failure [8]. However, it is becoming clearer that many, if not all, of the associations shown may not be direct. For example, in several studies the association between HDL cholesterol and adverse cardiovascular events diminished or disappeared after adjustment for low-density lipoprotein (LDL) cholesterol and apolipoprotein B concentrations [9], or statin treatments [10,11]. Genetic studies in humans also provide conflicting evidence of the role of HDL in the development of metabolic disease. Some genetic variants that are associated with increased HDL cholesterol, but not other lipids, are not associated with reduced risk for coronary heart disease [12]. Similarly, people with certain mutations in the gene coding for apolipoprotein A-I, the main structural protein for HDL, showed very low levels of HDL cholesterol without increased risks to cardiovascular risk [13].

At the same time, increasing HDL cholesterol pharmaceutically has so far not been successful in reducing disease risk. Both high-dose niacin and cholesterol ester transfer protein (CETP) inhibitors have been shown to increase HDL cholesterol , however, this has not been accompanied by reductions in disease risk [14,15] It is important to point out that in those cases, the unfortunate reason for the lack of benefit on cardiovascular outcomes appears to be off-target effects of the drugs. For example, it was recently shown that a downstream metabolite of niacin,

which is formed in some individuals even at levels consistent with intake at the recommended dietary allowance (RDA) for this nutrient, directly promotes vascular inflammation [16]. In the case of the CETP inhibitors, the first generation drugs were associated with increased mortality in phase III trials due to an off-target effect on blood pressure regulation [17].

Several recent epidemiological studies are now showing a U-shaped relationship between HDL cholesterol and all-cause mortality [18–20]. Together this evidence suggests a complex relationship between HDL and disease risk that cannot be easily addressed with the simple measurement of HDL-cholesterol concentrations. With this realization, new research has been conducted to understand the role of HDL particle size distribution, structure, and function in the relationship between HDL and disease risk. HDL composition, including the proteins, lipids, as well as small RNA, is also an important factor in HDL's effects on disease outcomes, but this topic has been reviewed extensively elsewhere [21,22]. In this review, we focus on the advantages and disadvantages of common methods of characterizing HDL particle size, structure and function, and summarize recent advancements in these methods in the last decade to provide better insights about HDL in its role in various chronic diseases.

3. Methods in understanding the physical properties of HDLs

The physical size and shape of HDLs have been linked to the risk of several conditions. Small HDL particles are inversely associated with the risk of cardiovascular disease (CVD) and all-cause mortality, whereas medium-to-large, large, and very-large HDLs are directly associated with CVD and all-cause mortality [23,24]. Moreover, the small HDL subclass was found to be reduced in Alzheimer's disease patients and the concentration of small HDLs correlated with cognitive performance [25,26]. However, the "small HDLs" defined by these studies may not be the

same as “small HDLs” defined by other separation techniques [27]. For example, non-denaturing gel electrophoresis identified 5 HDL subspecies separable on the basis of particle diameter: 7.2 to 7.8 nm, 7.8 to 8.2 nm, 8.2 to 8.8 nm, 8.8 to 9.7 nm, and 9.7 to 12.9 nm [27,28], whereas the ion mobility technique defines HDL in two subspecies with more generous cutoffs: small HDL (7.0 to 10.5 nm) and large HDL (10.5 to 14.5 nm) [26]. The relationship between HDL size and risks of Alzheimer’s disease may require analysis with higher precision. Common methods for characterizing HDL size are transmission electron microscopy (TEM), atomic force microscopy (AFM), 2-dimentional gel electrophoresis (2DGE).

3.1. Transmission Electron Microscopy (TEM)

TEM was one of the first methods used to measure the diameter of HDL particles as early as 1968 [29]. The protocol has since been updated by various groups to reduce artifact and to improve image contrast [30,31]. The most common use of the data from this method is to confirm gel electrophoresis results from different HDL isolation techniques [32,33]. The advantage of using negative stained (NS)-TEM as an HDL size measurement tool is underappreciated, for it provides accurate diameter data on every HDL particle captured by the micrograph. This reduces the level of measurement error compared to other sizing methods, such as gel electrophoresis, dynamic light scattering, and ion mobility. However, it is important to point out that sizing of HDL particles by NS-TEM necessitates their isolation from plasma, thus if the isolation method used results in the loss of certain particles or their modification, then the sizing results may not be representative of the particles that were in the original plasma sample.

Advancements in NS-TEM relies on the improvement of camera, sample preparation techniques, and computer algorithms in analyzing the data [30,34,35]. To date, these advanced NS-TEM methods have not been applied to explore the epidemiological relationships between HDL size and

disease risk, but instead have been more geared toward the structural characterization of HDL *per se*.

Cryogenic electron microscopy (cryo-EM) is different from NS-TEM in that samples are kept in a cryogen (e.g. liquid nitrogen) and the biological structure of the sample is preserved as much as possible. Because of low background noise, cryo-EM can be used to generate data for biomolecule 3D structure reconstructions. Cryo-EM single particle analysis (SPA) and cryo-electron tomography (cryo-ET) are two approaches to analyze 3D structures [36]. The field of cryo-EM has undergone rapid evolution as recent improvements in the development and commercialization of direct electron detectors [37].

Both SPA and cryo-ET approaches have been applied to understand the structure of lipoproteins [35,38–40], and provide in-depth detail on particle structure that confirms or rejects prior hypotheses on the structural characteristics of lipoproteins. For example, the Gang group reported their observations that human plasma very-low density lipoprotein (VLDL, [40]), intermediate-density lipoproteins (IDL, [35]) and low-density lipoproteins (LDL, [41]) are polyhedral, countering the common belief and NS-TEM observations that they are spherical particles. These observations are significant since flat surfaces have different hydrophobicity compared to round surfaces, which may explain some of the differences in lipid metabolism between VLDL, IDL, LDL, and HDL.

However, advancements in 3D reconstruction of HDLs has lagged behind the ApoB lipoproteins. One obstacle is the fact that human plasma HDLs are varied in size and composition, making it difficult to perform SPA. On the other hand, while challenges in class-averaging can be solved by individual-particle cryo-ET, an approach that has been successfully used to resolve the 3D structure of IDLs [35], a group of similarly heterogeneous lipoprotein, individual HDL particles do

not have great contrast from the cryo-EM background due to small particle size. Reconstituted HDL, which are more homogeneous in particle size and composition, has been a great model for HDL 3D structure characterization. Zhu et al. [34] combined cryo-EM SPA with Monte Carlo bias simulation using existing X-ray crystal structures of ApoA-I to create the first sub-10 nm density map for discoidal synthetic HDL. The model showed an elongated or oval shape of discoidal HDL, countering some previous conclusions that discoidal HDLs are circular on the top view. Yet, there are fundamental differences between reconstituted HDL and human plasma HDL, and many gaps in understanding remain. For example, reconstituted HDLs do not possess the same number and variety of HDL-associated proteins found in human HDLs.

3.2. Atomic Force Microscopy

AFM enables the characterization of particle size, shape, and stiffness. Gan et al. [42] showed that AFM can be used to measure the biophysical mechanical properties (e.g. Young's modulus and adhesive force) of HDL and suggest possible ways to distinguish HDL from other nanoparticles using these unique variables. Recently, Ridolfi et al. [43] utilized AFM as a particle profiling technique to distinguish and quantify HDL from other lipoprotein and nanoparticles and based on a combination of physical properties including size and mechanical stiffness. Plochberger et al. [44] combined high-speed AFM and fluorescence correlation spectroscopy to observe the integration of HDL into a synthetic membrane lipid bilayer. Investigations of the effects of oxidized/damaged LDL using AFM have yielded novel observations on the changes of particle size, stiffness, and stickiness due to oxidation and acidification treatments [45,46]. Understanding of HDL biology could potentially be improved by using AFM. However, HDL particles are at the very edge of the capabilities of AFM. While it is possible to image them with AFM, they are

almost the same size as the smallest available probe so they are in the range of the instrument where there is a lot of noise.

3.3. 2-dimensional gel electrophoresis

2DGE was used to show for the first time 12 distinct ApoA-I-containing HDL subpopulations [47]. In 2DGE, HDL particles are first separated by charge in agarose gel in one dimension, followed by a size-based separation with polyacrylamide gel in the perpendicular dimension. The technique has since been used to annotate different subpopulations with distinctive functions as well as linking different subpopulations with disease risk. For example, in a study cohort of 155 male participants, those with coronary heart disease had significantly lower concentrations of the large (pre-α_1, pre-α_2, and pre-α_3) HDL subpopulations [48]. Patients with the homozygous genetic Tangier disease were found to only have the smallest pre-β_1 HDL subpopulation [49]. The 2DGE technique continues to be used to characterize HDL subpopulation profile in different disease models, such as chronic kidney disease [50], obesity [51], CVD and diabetes [52]. However, the technique only remains in use in a small number of laboratories, as it has been largely displaced by more high-throughput approaches such as NMR and ion mobility-MS. In addition, a limitation of the 2DGE technique is the lack of nanoparticle size- and charge-based standards. The size of HDL particles is derived from their electrophoretic mobility in a gel compared to that of globular proteins, whose electrophoretic mobility may be affected by different factors in addition to size compared to HDL particles, which are multimolecular complexes of lipids, proteins, and even RNA and glycans.

4. Advancements in HDL biological function measurement

4.1. HDL functional measurements

The measurement of HDL particle number across HDL subpopulations has shown promise for the development of markers of disease, but the function of HDL, particularly cholesterol efflux capacity (CEC), has emerged as a robust predictor of CVD risk across numerous cohorts [53–55]. HDL cholesterol efflux is the initial step of the reverse cholesterol transport pathway, where HDL ApoA-I interacts with peripheral tissues to remove free cholesterol and cellular phospholipid for biliary excretion [56].

Traditionally, HDL CEC has been evaluated in an ex-vivo setting by loading cells with radiolabeled or fluorescently-labeled cholesterol, followed by the addition of apolipoprotein-B (ApoB) precipitated serum [57], ApoB-precipitated plasma [58], or isolated HDL [59] as cholesterol acceptors. However, no gold standard exists for the use of cell types, cholesterol acceptors, or treatment duration, leading to challenges in comparing CEC results across studies.

Recent studies have explored alternative methods to measure HDL's CEC. For example, a cost-efficient nanoparticle-based probe named ezFlux has been developed, formulated with BODIPY-cholesterol or ^{3}H-cholesterol, and measured in a 96-well plate format [60].

While HDL CEC demonstrates potential as a predictor of disease risk, other metrics of the reverse cholesterol transport pathway have also exhibited strong predictive capabilities. A new cell-free assay to measure HDL-specific phospholipid efflux using plasma or serum has been demonstrated to predict cardiovascular disease risk across three clinical cohorts compared to HDL-C and ApoA-I [61], providing additional information about the efflux function of HDL. The advantage of this method lies not only in its cell-free nature, which minimizes batch effects, but

also in its ability to be applied in a clinical setting without requiring HDL isolation or ApoB precipitation [61]. Further work is needed to explore whether specific HDL subclasses efflux phospholipid more effectively, particularly in disease conditions.

Another functional measurement in the reverse cholesterol transport pathway is HDL lecithin-cholesterol acyltransferase (LCAT) activity. HDL LCAT is a key enzyme that esterifies free cholesterol to cholesterol ester [62]. The activity of LCAT influences HDL cholesterol carrying capacity and its maturation, and loss of function has been observed in sepsis [63] and Alzheimer's disease patients [59,64]. A kit-based fluorescent assay compatible with serum [63], plasma [58], and isolated HDL obtained by ultracentrifugation [64] or sequential flotation ultracentrifugation followed by size-exclusion chromatography [59] has been developed for measuring HDL LCAT activity.

4.2. Antioxidant measurements

In addition to their ability to efflux cholesterol and phospholipids, HDL particles also serve multiple additional functions, including their ability to prevent or attenuate oxidation. Paraoxonase-1 (PON1), an HDL-associated protein, demonstrates atheroprotective effects by hydrolyzing oxidized LDL particles and modulating the oxidative state of macrophages [65,66]. The specific arylesterase activity of PON1 in ApoB-depleted serum or in isolated HDL can be measured using a photometric assay that quantifies the hydrolysis of phenylacetate. This activity has been observed to be decreased in COVID-19 patients and those with gestational hypertension [67,68]. The measurement of arylesterase activity can be performed in various isolated HDL subclasses, for example, HDL particles which have been precipitated from plasma using dextran sulfate-Mg^{2+}, as well as HDL subclasses isolated by ultracentrifugation(i.e. HDL_2 and HDL_3) [69]. Importantly, this method offers the advantage of high-throughput analysis in a 96-well format.

Additionally, recent studies have explored the use of non-denaturing polyacrylamide gel separation of HDL subclasses coupled with the zymogram method to evaluate PON1 arylesterase activity directly in the gel, providing a means for in situ assessment [70,71]. However, one drawback of this approach is that since HDL subclass PON1 arylesterase activity is measured in the gel, it is unable to correlate with functional and compositional markers specific to those HDL subclasses.

Recent advancements have allowed for the assessment of HDL's antioxidant properties through various techniques. Both isolated HDL via a two-step density gradient and ApoB-depleted serum have demonstrated antioxidant properties, as measured by their ability to prevent the oxidation of dihydrorhodamine, a substrate used in the antioxidant assay, which has been shown to decrease in allergic rhinitis [72]. An advantage of this method is its applicability in a 384-well plate, requiring as little as 10 ug of isolated HDL protein or 1 uL of ApoB-depleted serum [67,68,72].

4.3. HDL inflammatory index (HII)

ApoAI, PON1, and other antioxidative HDL-associated proteins of minor abundance (e.g. plate activating factor acetylhydrolase, LCAT, apoJ, and glutathione peroxidase) prevent the oxidation of phospholipids in LDL, human artery wall cells [73,74]. These oxidized phospholipids are important signals for inflammatory responses. During acute phase responses, serum amyloid A replaces apoA-I in HDLs, reduces the abundance of PON1 and other antioxidative proteins on HDLs, and turns HDLs from anti-inflammatory into pro-inflammatory agents [75]. HDL inflammatory index (HII) is a measurement to address this dual-role nature of HDLs in immunomodulation. Dunbar et al. [76] showed the oral ApoA-I mimetic D-4F lowered the HII by ~25% compared to a sucrose placebo in 8 hours, and by ~50% compared to baseline in a cohort of 62 participants. Ajala et al [77] reported a 12-month treatment of rosuvastatin decreased HII by a

mean of 5.3% (n = 517) compared to 1.3% reduction in the placebo group (n = 517) in a nested case-control study of the JUPITER trial. HII has also been reported to be positively correlated with sequential organ failure assessment in a study of 88 sepsis patients [78], to adjusted hazard ratio for death in 189 hemodialysis patients [79], and, in multiple studies, to CVD risk [80–82]. On the other hand, HII showed negative correlation with moderate- and vigorous-intensity physical activity duration in a study with 642 participants [83].

HII is most commonly measured as HDL's effect on adhesion of monocyte to, and migration through, the endothelial cell layer induced by LDL [84], and reported as an index compared to standard LDL or standard LDL+HDL [85]. However, variations of HII determination exist. For example, instead of measuring adhesion of monocytes, one study measured the fluorescence of oxidized phospholipid on LDL with or without HDL [77,83,86]. It is not entirely clear which methods are more robust for HII measurement, but the validity and reproducibility of the results are significantly affected by the specific methods used. Lemmers et al. [84] reviewed 13 research publications reporting on the relationships between HDL inflammatory function and T2DM and concluded that many studies could be biased by low sample size, the criteria for the control group, the selection of specific HDL subgroups, the selection of specific endpoints, and potential publication bias. Standardizing these potential confounders may be the key to make HII a more robust biomarker for disease prediction.

4.4. HDL metabolism studies with labeled tracers

Tracer studies of HDL-associated proteins allow investigators to reveal their metabolism, which improves understanding of how HDL functional capacity changes throughout their course in the blood circulation. There are exogenous and endogenous tracer labeling methods. In exogenous

labeling, radio-labeled ApoA-I or HDL (tracers) are prepared *ex vivo* and then injected into study participants, and the movement of the tracer into different HDL subpopulations is monitored by collecting blood over a study duration. In endogenous tracer labeling, stable isotope-labeled amino acids are injected into the study participants, and traced as the labeled amino acids are taken up by tissues, and incorporated into nascent proteins and HDLs [87]. Advancements in tracer studies have benefited from replacement of radioisotope to stable isotope amino acid tracers, improvements in chromatography methods and MS detection sensitivity, and improvements in HDL isolation techniques. Andraski et al. [87] provided a detailed summary of the progress of HDL protein tracer studies. For example, stable isotope (endogenous) tracer studies revealed that the fractional catabolism rate of both ApoA-I and ApoA-II was slower than if they were measured using radio (exogenous) labeling methods [87]. The review highlights the advantage of endogenous tracer studies in which the HDL particles of interest are endogenously synthesized by organs, rather than reconstituted *ex vivo* and then injected subsequently into the study participants [87]. With finer technique in separation of HDL subpopulations, unique protein metabolism and activity were found in distinctive HDL subpopulations. For example, Singh et al. [88] showed that phospholipid transfer protein (PLTP) on medium α2-HDL is transferred to the large α1- and α0-HDLs. It was also shown that CETP and LCAT remain on HDLs until the HDLs are cleared from the circulation [88]. Tracer studies also allow investigators to identify the origin of HDL-associated proteins. Andraski et al. [89] showed that ApoA-IV on HDLs originated from distinct sources, suggesting that the ApoA-IV in small HDLs may be derived from the small intestine, while the ApoA-IV in large HDLs may be transferred from other small intestine-derived lipoproteins, such as chylomicrons.

5. CONCLUSION

In conclusion, the landscape of HDL research has evolved significantly, challenging traditional views and opening new avenues for therapeutic intervention. While the focus on HDL cholesterol content has dominated, recent investigations emphasize the importance of understanding HDL's physical properties, biological functions, and compositional makeup.

Methods like TEM and cryo-TEM, AFM, and 2DGE have revealed the diverse sizes and shapes of HDL particles and providing new ways for deeper functional insights. Advancements in measuring HDL's biological functions, such as CEC, antioxidant properties, and HII, offer promising avenues for clinical assessment and risk prediction. Novel assays like nanoparticle-based probes and cell-free assays show potential for enhancing our understanding of HDL's dynamic metabolism and its role in disease pathogenesis. In essence, a multidisciplinary approach integrating physical and functional is essential for a comprehensive understanding of HDL biology.

6. REFERENCES

1. Castelli, W. P. *et al.* Incidence of coronary heart disease and lipoprotein cholesterol levels: the Framingham Study. *Jama* **256**, 2835–2838 (1986).
2. Mackey, R. H. *et al.* High-density lipoprotein cholesterol and particle concentrations, carotid atherosclerosis, and coronary events: MESA (multi-ethnic study of atherosclerosis). *J. Am. Coll. Cardiol.* **60**, 508–516 (2012).
3. Assessment, R. Major lipids, apolipoproteins, and risk of vascular disease. *Jama* **302**, 1993–2000 (2009).
4. Abbasi, A. *et al.* Role of HDL cholesterol and estimates of HDL particle composition in future development of type 2 diabetes in the general population: the PREVEND study. *J. Clin. Endocrinol. Metab.* **98**, E1352–E1359 (2013).
5. Loosen, S. H., Kostev, K., Luedde, M., Luedde, T. & Roderburg, C. Low blood levels of high-density lipoprotein (HDL) cholesterol are positively associated with cancer. *J. Cancer Res. Clin. Oncol.* **148**, 3039–3046 (2022).
6. Revilla, G. *et al.* LDL, HDL and endocrine-related cancer: From pathogenic mechanisms to therapies. in vol. 73 134–157 (Elsevier, 2021).
7. Pedrini, S., Chatterjee, P., Hone, E. & Martins, R. N. High-density lipoprotein-related cholesterol metabolism in Alzheimer's disease. *J. Neurochem.* (2020).
8. Bowe, B., Xie, Y., Xian, H., Balasubramanian, S. & Al-Aly, Z. Low levels of high-density lipoprotein cholesterol increase the risk of incident kidney disease and its progression. *Kidney Int.* **89**, 886–896 (2016).
9. Otvos, J. D. *et al.* Low-density lipoprotein and high-density lipoprotein particle subclasses predict coronary events and are favorably changed by gemfibrozil therapy in the Veterans Affairs High-Density Lipoprotein Intervention Trial. *Circulation* **113**, 1556–1563 (2006).
10. Barter, P. *et al.* HDL cholesterol, very low levels of LDL cholesterol, and cardiovascular events. *N. Engl. J. Med.* **357**, 1301–1310 (2007).
11. Ridker, P. M. *et al.* HDL cholesterol and residual risk of first cardiovascular events after treatment with potent statin therapy: an analysis from the JUPITER trial. *The Lancet* **376**, 333–339 (2010).
12. Voight, B. F. *et al.* Plasma HDL cholesterol and risk of myocardial infarction: a mendelian randomisation study. *The Lancet* **380**, 572–580 (2012).
13. Sirtori, C. R. *et al.* Cardiovascular status of carriers of the apolipoprotein A-IMilano mutant: the Limone sul Garda study. *Circulation* **103**, 1949–1954 (2001).
14. Rosenson, R. S. The high-density lipoprotein puzzle: why classic epidemiology, genetic epidemiology, and clinical trials conflict? *Arterioscler. Thromb. Vasc. Biol.* **36**, 777–782 (2016).
15. Tall, A. R. HDL in morbidity and mortality: a 40+ year perspective. *Clin. Chem.* **67**, 19–23 (2021).
16. Ferrell, M. *et al.* A terminal metabolite of niacin promotes vascular inflammation and contributes to cardiovascular disease risk. *Nat. Med.* 1–11 (2024).
17. Tall, A. R. & Rader, D. J. Trials and tribulations of CETP inhibitors. *Circ. Res.* **122**, 106–112 (2018).
18. Stensvold, I. *et al.* High-density lipoprotein cholesterol and coronary, cardiovascular and all cause mortality among middle-aged Norwegian men and women. *Eur. Heart J.* **13**, 1155–1163 (1992).

19. Mazidi, M., Mikhailidis, D. P. & Banach, M. Associations between risk of overall mortality, cause-specific mortality and level of inflammatory factors with extremely low and high high-density lipoprotein cholesterol levels among American adults. *Int. J. Cardiol.* **276**, 242–247 (2019).
20. Oh, I.-H. *et al.* Very high high-density lipoprotein cholesterol is associated with increased all-cause mortality in South Koreans. *Atherosclerosis* **283**, 43–51 (2019).
21. Vickers, K. C., Palmisano, B. T., Shoucri, B. M., Shamburek, R. D. & Remaley, A. T. MicroRNAs are transported in plasma and delivered to recipient cells by high-density lipoproteins. *Nat. Cell Biol.* **13**, 423–433 (2011).
22. Davidson, W. S., Shah, A. S., Sexmith, H. & Gordon, S. M. The HDL proteome watch: compilation of studies leads to new insights on HDL function. *Biochim. Biophys. Acta BBA-Mol. Cell Biol. Lipids* **1867**, 159072 (2022).
23. Jin, Q. *et al.* High-density lipoprotein subclasses and cardiovascular disease and mortality in type 2 diabetes: analysis from the Hong Kong Diabetes Biobank. *Cardiovasc. Diabetol.* **21**, 293 (2022).
24. Li, R. *et al.* Associations of lipoprotein subclasses with risk of all-cause and cardiovascular disease mortality in individuals with type 2 diabetes: A prospective cohort study. *Diabetes Obes. Metab.* **25**, 3259–3267 (2023).
25. Pedrini, S. *et al.* Plasma high density lipoprotein small subclass is reduced in Alzheimer's disease patients and correlates with cognitive performance. *J. Alzheimers Dis.* **77**, 733–744 (2020).
26. Martinez, A. E. *et al.* The small HDL particle hypothesis of Alzheimer's disease. *Alzheimers Dement.* (2022).
27. Rosenson, R. S. *et al.* HDL measures, particle heterogeneity, proposed nomenclature, and relation to atherosclerotic cardiovascular events. *Clin. Chem.* **57**, 392–410 (2011).
28. Blanche, P. J., Gong, E. L., Forte, T. M. & Nichols, A. V. Characterization of human high-density lipoproteins by gradient gel electrophoresis. *Biochim. Biophys. Acta BBA-Lipids Lipid Metab.* **665**, 408–419 (1981).
29. Forte, G., Nichols, A. & Glaeser, R. Electron microscopy of human serum lipoproteins using negative staining. *Chem. Phys. Lipids* **2**, 396–408 (1968).
30. Zhang, L., Tong, H., Garewal, M. & Ren, G. Optimized negative-staining electron microscopy for lipoprotein studies. *Biochim. Biophys. Acta BBA-Gen. Subj.* **1830**, 2150–2159 (2013).
31. Zhang, L. *et al.* An optimized negative-staining protocol of electron microscopy for apoE4• POPC lipoprotein. *J. Lipid Res.* **51**, 1228–1236 (2010).
32. Chapman, M., Goldstein, S., Lagrange, D. & Laplaud, P. A density gradient ultracentrifugal procedure for the isolation of the major lipoprotein classes from human serum. *J. Lipid Res.* **22**, 339–358 (1981).
33. Zheng, J. J. *et al.* Isolation of HDL by sequential flotation ultracentrifugation followed by size exclusion chromatography reveals size-based enrichment of HDL-associated proteins. *Sci. Rep.* **11**, 1–15 (2021).
34. Zhu, L. *et al.* Structures of apolipoprotein AI in high density lipoprotein generated by electron microscopy and biased simulations. *Biochim. Biophys. Acta BBA-Gen. Subj.* **1861**, 2726–2738 (2017).

35. Lei, D. *et al.* Single-molecule 3D imaging of human plasma intermediate-density lipoproteins reveals a polyhedral structure. *Biochim. Biophys. Acta BBA-Mol. Cell Biol. Lipids* **1864**, 260–270 (2019).
36. Danev, R., Yanagisawa, H. & Kikkawa, M. Cryo-electron microscopy methodology: current aspects and future directions. *Trends Biochem. Sci.* **44**, 837–848 (2019).
37. McMullan, G., Faruqi, A. & Henderson, R. Direct electron detectors. *Methods Enzymol.* **579**, 1–17 (2016).
38. Zhang, L. *et al.* Structural basis of transfer between lipoproteins by cholesteryl ester transfer protein. *Nat. Chem. Biol.* **8**, 342–349 (2012).
39. Zhang, M. *et al.* HDL surface lipids mediate CETP binding as revealed by electron microscopy and molecular dynamics simulation. *Sci. Rep.* **5**, 1–8 (2015).
40. Yu, Y. *et al.* Polyhedral 3D structure of human plasma very low density lipoproteins by individual particle cryo-electron tomography1 [S]. *J. Lipid Res.* **57**, 1879–1888 (2016).
41. Ren, G. *et al.* Model of human low-density lipoprotein and bound receptor based on cryoEM. *Proc. Natl. Acad. Sci.* **107**, 1059–1064 (2010).
42. Gan, C., Ao, M., Liu, Z. & Chen, Y. Imaging and force measurement of LDL and HDL by AFM in air and liquid. *FEBS Open Bio* **5**, 276–282 (2015).
43. Ridolfi, A. *et al.* Particle profiling of EV-lipoprotein mixtures by AFM nanomechanical imaging. *J. Extracell. Vesicles* **12**, 12349 (2023).
44. Plochberger, B. *et al.* HDL particles incorporate into lipid bilayers–a combined AFM and single molecule fluorescence microscopy study. *Sci. Rep.* **7**, 1–10 (2017).
45. Wang, K., Li, Y., Luo, C. & Chen, Y. Dynamic AFM detection of the oxidation-induced changes in size, stiffness, and stickiness of low-density lipoprotein. *J. Nanobiotechnology* **18**, 1–10 (2020).
46. Wang, K. *et al.* AFM detects the effects of acidic condition on the size and biomechanical properties of native/oxidized low-density lipoprotein. *Colloids Surf. B Biointerfaces* **208**, 112053 (2021).
47. Asztalos, B. F., Sloop, C. H., Wong, L. & Roheim, P. S. Two-dimensional electrophoresis of plasma lipoproteins: recognition of new apo AI-containing subpopulations. *Biochim. Biophys. Acta BBA-Lipids Lipid Metab.* **1169**, 291–300 (1993).
48. Asztalos, B. F. *et al.* Distribution of ApoA-I–Containing HDL Subpopulations in Patients With Coronary Heart Disease. *Arterioscler. Thromb. Vasc. Biol.* **20**, 2670–2676 (2000).
49. Asztalos, B. F. *et al.* High-density lipoprotein subpopulation profile and coronary heart disease prevalence in male participants of the Framingham Offspring Study. *Arterioscler. Thromb. Vasc. Biol.* **24**, 2181–2187 (2004).
50. Gliwińska, A. *et al.* Changes in the size and electrophoretic mobility of HDL subpopulation particles in chronic kidney disease. *J. Nephrol.* **36**, 115–124 (2023).
51. Tang, H. *et al.* Potential role of anti-inflammatory HDL subclasses in metabolic unhealth/obesity. *Artif. Cells Nanomedicine Biotechnol.* **49**, 564–574 (2021).
52. Davidson, W. S., Cooke, A. L., Swertfeger, D. K. & Shah, A. S. The Difference Between High Density Lipoprotein Subfractions and Subspecies: an Evolving Model in Cardiovascular Disease and Diabetes. *Curr. Atheroscler. Rep.* **23**, 23 (2021).
53. Khera, A. V. *et al.* Cholesterol Efflux Capacity, High-Density Lipoprotein Function, and Atherosclerosis. *N. Engl. J. Med.* **364**, 127–135 (2011).
54. Khera, A. V. *et al.* Cholesterol Efflux Capacity, High-Density Lipoprotein Particle Number, and Incident Cardiovascular Events: An Analysis From the JUPITER Trial (Justification for

the Use of Statins in Prevention: An Intervention Trial Evaluating Rosuvastatin). *Circulation* **135**, 2494–2504 (2017).
55. Rohatgi, A. *et al.* HDL cholesterol efflux capacity and incident cardiovascular events. *N. Engl. J. Med.* **371**, 2383–2393 (2014).
56. Phillips, M. C. Molecular Mechanisms of Cellular Cholesterol Efflux. *J. Biol. Chem.* **289**, 24020–24029 (2014).
57. Davidson, W. S. *et al.* The effects of apolipoprotein B depletion on HDL subspecies composition and function. *J. Lipid Res.* **57**, 674–686 (2016).
58. Hong, B. V. *et al.* Seasonal Factors Are Associated with Activities of Enzymes Involved in High-Density Lipoprotein Metabolism among Pregnant Females in Ghana. *Curr. Dev. Nutr.* **7**, 102041 (2023).
59. Hong, B. V. *et al.* High-Density Lipoprotein Changes in Alzheimer's Disease Are APOE Genotype-Specific. *Biomedicines* **10**, 1495 (2022).
60. Ravodina, A. M., Badgeley, M. A., Rajagopalan, S., Fedyukina, D. V. & Maiseyeu, A. Facile Cholesterol Loading with a New Probe ezFlux Allows for Streamlined Cholesterol Efflux Assays. *ACS Omega* **5**, 23289–23298 (2020).
61. Sato, M. *et al.* Cell-free, high-density lipoprotein–specific phospholipid efflux assay predicts incident cardiovascular disease. *J. Clin. Invest.* **133**, e165370 (2023).
62. Asztalos, B. F. *et al.* Role of LCAT in HDL remodeling: investigation of LCAT deficiency states. *J. Lipid Res.* **48**, 592–599 (2007).
63. Reisinger, A. C. *et al.* Impact of Sepsis on High-Density Lipoprotein Metabolism. *Front. Cell Dev. Biol.* **9**, (2022).
64. Khalil, A., Berrougui, H., Pawelec, G. & Fulop, T. Impairment of the ABCA1 and SR-BI-mediated cholesterol efflux pathways and HDL anti-inflammatory activity in Alzheimer's disease. *Mech. Ageing Dev.* **133**, 20–29 (2012).
65. Aviram, M. & Rosenblat, M. Paraoxonases 1, 2, and 3, oxidative stress, and macrophage foam cell formation during atherosclerosis development. *Free Radic. Biol. Med.* **37**, 1304–1316 (2004).
66. Mackness, M. I., Arrol, S. & Durrington, P. N. Paraoxonase prevents accumulation of lipoperoxides in low-density lipoprotein. *FEBS Lett.* **286**, 152–154 (1991).
67. Stadler, J. T. *et al.* Low HDL Cholesterol Efflux Capacity Indicates a Fatal Course of COVID-19. *Antioxid. Basel Switz.* **11**, 1858 (2022).
68. Stadler, J. T. *et al.* Gestational Hypertension and High-Density Lipoprotein Function: An Explorative Study in Overweight/Obese Women of the DALI Cohort. *Antioxidants* **12**, 68 (2022).
69. Valencia C, S. Y. *et al.* Arylesterase activity of paraoxonase 1 (PON1) on HDL3 and HDL2: Relationship with Q192R, C-108T, and L55M polymorphisms. *Biochem. Biophys. Rep.* **26**, 100971 (2021).
70. Gugliucci, A., Caccavello, R., Kotani, K., Sakane, N. & Kimura, S. Enzymatic assessment of paraoxonase 1 activity on HDL subclasses: A practical zymogram method to assess HDL function. *Clin. Chim. Acta* **415**, 162–168 (2013).
71. Miljkovic, M. *et al.* Activity of paraoxonase 1 (PON1) on HDL2 and HDL3 subclasses in renal disease. *Clin. Biochem.* **60**, 52–58 (2018).
72. Trakaki, A. *et al.* Allergic rhinitis is associated with complex alterations in high-density lipoprotein composition and function. *Biochim. Biophys. Acta BBA - Mol. Cell Biol. Lipids* **1864**, 1280–1292 (2019).

73. Navab, M. *et al.* Normal high density lipoprotein inhibits three steps in the formation of mildly oxidized low density lipoprotein: step 1. *J. Lipid Res.* **41**, 1481–1494 (2000).
74. Navab, M. *et al.* Normal high density lipoprotein inhibits three steps in the formation of mildly oxidized low density lipoprotein: steps 2 and 3. *J. Lipid Res.* **41**, 1495–1508 (2000).
75. Navab, M. *et al.* HDL and the inflammatory response induced by LDL-derived oxidized phospholipids. *Arterioscler. Thromb. Vasc. Biol.* **21**, 481–488 (2001).
76. Dunbar, R. L. *et al.* Oral apolipoprotein A-I mimetic D-4F lowers HDL-inflammatory index in high-risk patients: a first-in-human multiple-dose, randomized controlled trial. *Clin. Transl. Sci.* **10**, 455–469 (2017).
77. Ajala, O. N. *et al.* Anti-Inflammatory HDL Function, Incident Cardiovascular Events, and Mortality: A Secondary Analysis of the JUPITER Randomized Clinical Trial. *J. Am. Heart Assoc.* **9**, e016507 (2020).
78. Guirgis, F. W. *et al.* HDL inflammatory index correlates with and predicts severity of organ failure in patients with sepsis and septic shock. *PLoS One* **13**, e0203813 (2018).
79. Kalantar-Zadeh, K., Kopple, J., Kamranpour, N., Fogelman, A. & Navab, M. HDL-inflammatory index correlates with poor outcome in hemodialysis patients. *Kidney Int.* **72**, 1149–1156 (2007).
80. Dod, R., Rajendran, A., Kathrotia, M., Clarke, A. & Dodani, S. Cardiovascular disease in south asian immigrants: a review of dysfunctional HDL as a potential marker. *J. Racial Ethn. Health Disparities* **10**, 1194–1200 (2023).
81. Takata, K. *et al.* Associations of high-density lipoprotein functionality with coronary plaque characteristics in diabetic patients with coronary artery disease: integrated backscatter intravascular ultrasound analysis. *Biomolecules* **13**, 1278 (2023).
82. Endo, Y., Fujita, M. & Ikewaki, K. HDL functions—current status and future perspectives. *Biomolecules* **13**, 105 (2023).
83. Viadas, R. *et al.* Association of physical activity with high-density lipoprotein functionality in a population-based cohort: the REGICOR study. *Rev. Esp. Cardiol. Engl. Ed.* **76**, 86–93 (2023).
84. Lemmers, R. F. *et al.* The anti-inflammatory function of high-density lipoprotein in type II diabetes: A systematic review. *J. Clin. Lipidol.* **11**, 712–724 (2017).
85. Navab, M. *et al.* High-density lipoprotein: antioxidant and anti-inflammatory properties. *Curr. Atheroscler. Rep.* **9**, 244–248 (2007).
86. Patel, P. J., Khera, A. V., Jafri, K., Wilensky, R. L. & Rader, D. J. The anti-oxidative capacity of high-density lipoprotein is reduced in acute coronary syndrome but not in stable coronary artery disease. *J. Am. Coll. Cardiol.* **58**, 2068–2075 (2011).
87. Andraski, A. B., Sacks, F. M., Aikawa, M. & Singh, S. A. Understanding HDL Metabolism and Biology Through In Vivo Tracer Kinetics. *Arterioscler. Thromb. Vasc. Biol.* **44**, 76–88 (2024).
88. Singh, S. A. *et al.* Metabolism of PLTP, CETP, and LCAT on multiple HDL sizes using the Orbitrap Fusion Lumos. *JCI Insight* **6**, (2021).
89. Andraski, A. B. *et al.* The distinct metabolism between large and small HDL indicates unique origins of human apolipoprotein A4. *JCI Insight* **8**, (2023).

Chapter 2: Isolation of HDL by sequential flotation ultracentrifugation followed by size exclusion chromatography reveals size-based enrichment of HDL-associated proteins

Jack Jingyuan Zheng[a], Joanne K. Agus[a], Brian V. Hong[a], Xinyu Tang[a], Christopher H. Rhodes[a], Hannah E. Houts[a], Chenghao Zhu[a], Jea Woo Kang[a], Maurice Wong[b], Yixuan Xie[b], Carlito B. Lebrilla[b], Emily Mallick[c], Kenneth W. Witwer[c], Angela M. Zivkovic[a*]

[a] Department of Nutrition, University of California, Davis, California, United States of America.

[b] Department of Chemistry, University of California, Davis, California, United States of America.

[c] Department of Molecular and Comparative Pathobiology, Johns Hopkins University School of Medicine, MD, USA

1. ABSTRACT

High-density lipoprotein (HDL) particles have multiple beneficial and cardioprotective roles, yet our understanding of their full structural and functional repertoire is limited due to challenges in separating HDL particles from contaminating plasma proteins and other lipid-carrying particles that overlap HDL in size and/or density. Here we describe a method for isolating HDL particles using a combination of sequential flotation density ultracentrifugation and fast protein liquid chromatography with a size exclusion column. Purity was visualized by polyacrylamide gel electrophoresis and verified by proteomics, while size and structural integrity were confirmed by transmission electron microscopy. This HDL isolation method can be used to isolate a high yield of purified HDL from a low starting plasma volume for functional analyses. This method also enables investigators to select their specific HDL fraction of interest: from the least inclusive but highest purity HDL fraction eluting in the middle of the HDL peak, to pooling all of the fractions to capture the breadth of HDL particles in the original plasma sample. We show that certain proteins such as lecithin cholesterol acyltransferase (LCAT), phospholipid transfer protein (PLTP), and clusterin (CLUS) are enriched in large HDL particles whereas proteins such as alpha-2HS-glycoprotein (A2HSG), alpha-1 antitrypsin (A1AT), and vitamin D binding protein (VDBP) are enriched or found exclusively in small HDL particles.

2. INTRODUCTION

High Density Lipoprotein (HDL) particles are the primary cholesterol scavenging vehicles most known for their role as mediators of cardiovascular health and their involvement in attenuating the progression and pathogenesis of cardiovascular disease (CVD) [1]. Epidemiological studies have shown a negative correlation between serum HDL-cholesterol levels and the risk of coronary heart disease [2]. Despite HDL's well-known clinical significance, basic research on HDL function and composition has produced many confusing and inconsistent results. This is in part due to the difficulty of isolating functional HDL from plasma that represents the diversity of HDL particles, preserves particle integrity, and is uncontaminated by other plasma components [3]. There is a renewed interest in lipoprotein particles due to the recent discovery that they are carriers of extracellular RNA [4]. The extracellular RNA carriers in plasma (i.e. lipoprotein particles and extracellular vesicles (EVs)) span the range from as small as 7 nm in radius to as large as 1 micron in radius, and from a density of 1.21 g/mL to close to plasma density at 1.006 g/mL (Figure 2.1). Classically, HDL is isolated by ultracentrifugation (UC) based on the finding that HDL particles float in the density range of 1.063 – 1.210 g/mL, which allows their separation from less dense lipoprotein particles such as chylomicrons, very-low density lipoprotein (VLDL), intermediate-density lipoprotein (IDL), and low-density lipoprotein (LDL), and denser serum proteins [5]. However, if HDL particles are separated by density alone, they overlap the density range of some LDL (1.019-1.063 g/mL, Figure 2.1) and if they are isolated by size alone, they overlap the size range of many plasma proteins (e.g. ferritin at about 12 nm radius). A plethora of additional isolation strategies have been reported including size exclusion chromatography (SEC) [6,7], immunoaffinity precipitation [8-10], chemical precipitation [11,12],

asymmetrical flow field flow fractionation (AF4) [13], and approaches combining these techniques [4,14,15].

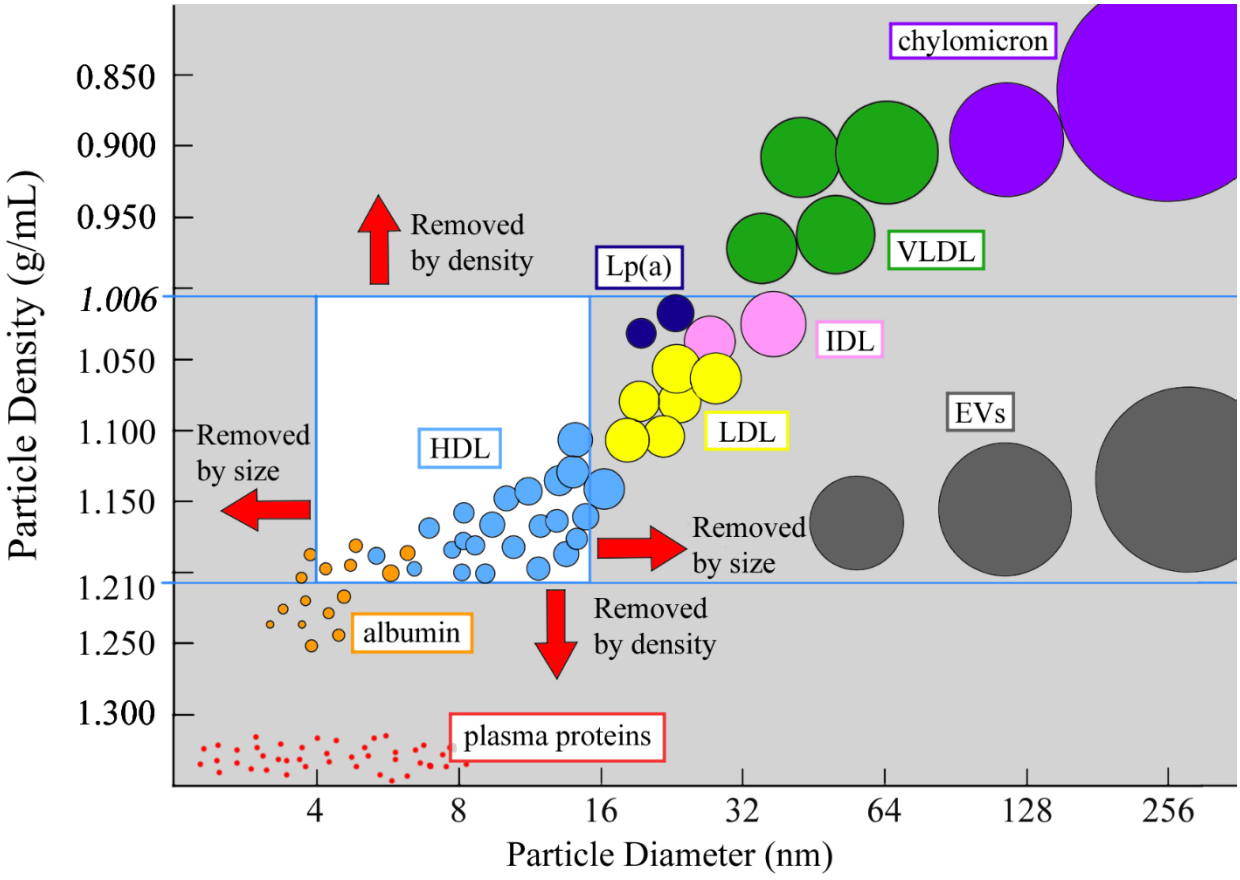

Figure 2.1. Schematic of the size and density range of lipoproteins and low-density plasma components. The white box indicates the density and size of high density lipoprotein (HDL) particles captured by this HDL isolation method, as well as the particle diameter (nm) and particle density (g/mL) of the other lipoprotein particles – chylomicrons, very low density lipoproteins (VLDL), intermediate density lipoproteins (IDL), low density lipoproteins (LDL), lipoprotein (a) (Lp(a)), and extracellular vesicles (EVs) present in plasma that are simultaneously isolated as part of this method.

Careful selection of HDL isolation method is critical as different isolation methods can produce starkly different yields and experimental results. For example, depending on the isolation method, the HDL proteome has been reported to contain as many as >100 proteins [3], or as few as a dozen [15]. Given that each HDL isolation method has its own advantages and disadvantages, and that the results of a study will vary based on the method, there are a number of variables to consider when choosing an isolation method. For example, while UC-based HDL isolation has the advantage of being scalable to yield high quantities of HDL, prolonged UC duration can damage particle structure and result in the loss of certain attached proteins [16,17]. On the other hand, while direct SEC-based separation from plasma is a gentler extraction procedure, without further clean-up there can be extensive contamination with LDL and serum proteins [6]. Immunoaffinity-based HDL isolation using antibodies to HDL proteins can offer a high degree of both sensitivity and specificity but produces low yields and is expensive. One of the newest and most promising methods for HDL isolation is asymmetric-flow field-flow fractionation (AF4), which has the advantages of gentle extraction and excellent reproducibility [13]. However, the method requires advanced instrumentation and technical expertise that is not yet widely available. Many of these techniques also lack adjustability. Depending on the research question and logistical limitations of the particular research project, the parameters that need to be optimized by the HDL isolation method may differ because often maximizing for certain parameters necessitates compromising on other parameters. For example, maximizing for purity typically means loss of particle diversity, whereas maximizing yield often means loss of purity.

Here we report an HDL isolation method, suitable for the purpose of isolating HDL from human plasma samples for multiple simultaneous structural, compositional, and functional assays. The method combines sequential flotation UC followed by SEC, based on a previously

published method using density gradient UC followed by SEC [15]. The method described here separates the HDL first by density from triglyceride-rich particles and serum proteins, then isolates the HDL by size from LDL and albumin (Figure 2.2). The method yields highly purified HDL fractions verified by polyacrylamide gel electrophoresis (PAGE), transmission electron microscopy (TEM), and proteomics. The advantages of this method include: 1) ability to fine tune the HDL fraction(s) of interest, from the least inclusive but purest fraction to pooling multiple fractions in order to capture particle heterogeneity; 2) preservation of particle integrity due to minimal centrifugation duration (a total of 4 h) and lack of introduction of chemical or other modifying agents, making it amenable for *in vitro* functional assays and particle size and structural analysis; 3) a low starting plasma volume requirement (500 uL or less but with lower HDL yield), making it suitable for clinical studies with limited sample availability such as studies using samples from biorepositories or previously conducted cohort studies; 4) high yield – a concentrated 100 uL aliquot of HDL fractions at a concentration of on average 4 mg/ml protein (400 µg total protein) which can be divided into several aliquots for multiple simultaneous compositional and functional analyses; 5) high throughput – separation of 8 samples within 12 h; and 6) high purity – a demonstrated minimal contamination from serum proteins and other lipoprotein particles including LDL. In addition, this method simultaneously allows for the isolation of chylomicrons/VLDL, IDL, LDL, serum proteins, and lipidated albumin from the same starting plasma, which means that precious samples can be maximally mined.

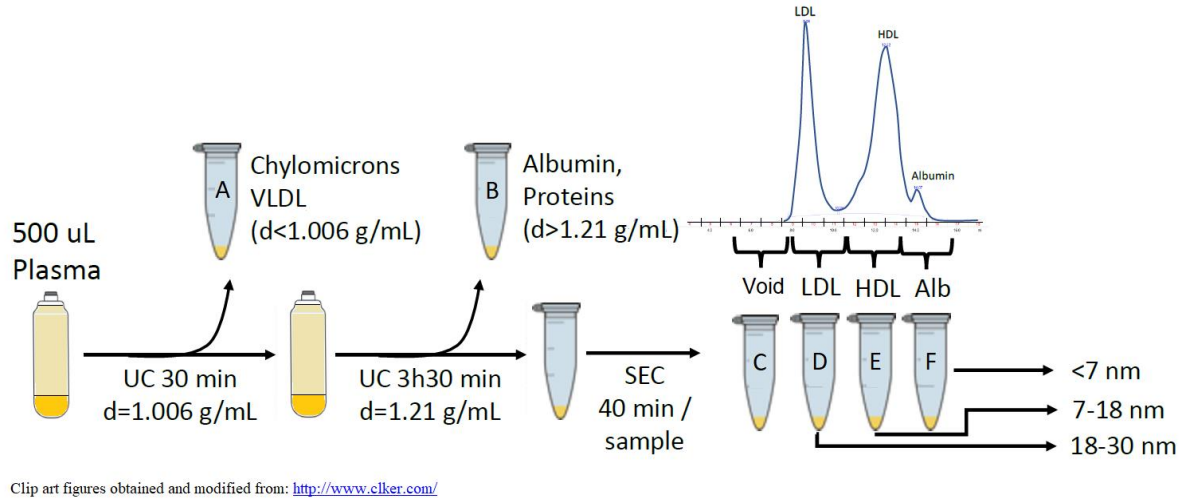

Figure 2.2. Visual abstract of the isolation method. A starting plasma volume of 500uL is first subjected to sequential flotation ultracentrifugation (UC) at a density of d=1.006 g/mL to float off the chylomicrons and very low density lipoproteins (VLDL) (A: particles with density d<1.006 g/mL), followed by a second UC at a density of d=1.21 g/mL to precipitate out the albumin and other plasma proteins (B: proteins with density d>1.21 g/mL). The resulting supernatant of density in the range of 1.006–1.21 g/mL is then separated by size exclusion chromatography (SEC) to yield intermediate density lipoproteins (IDL)) (C: size range of 30-200nm in diameter), low density lipoproteins (LDL) (D: size range of 18-30nm in diameter), high density lipoproteins (HDL) (E: size range of 7-18nm in diameter), and albumin (F: size <7nm in diameter).

3. MATERIALS AND METHODS

The objective of this method is to isolate HDL particles via a 2-step process including a sequential flotation UC step to remove triglyceride-rich particles and plasma proteins by density, followed by SEC using an FPLC system to separate the lipoproteins by size. The aim of the UC step is to isolate plasma particles in the density range of 1.006-1.210 g/ml, which includes IDL,

LDL, HDL, and albumin, but excludes chylomicrons, VLDL, and plasma proteins. The aim of the SEC step is to isolate the HDL particles from both the larger particles (i.e. LDL) and the smaller particles (i.e. albumin) using a SEC column. Figure 2.1 illustrates the size (radius in nm) and density ranges (in g/mL) of plasma proteins and lipoproteins, and indicates the specific density and size range that this UC-SEC method achieves for HDL isolation and purification.

Biological sample collection

Pooled human plasma samples from a previously conducted trial were used for the method development in this study. The trial was a cross-over, double blinded investigation of the effects of 4 weeks supplementation with a dietary fiber supplement vs. placebo. Only the baseline (i.e. pre-intervention) plasma samples were used to generate the plasma pool. The subjects were young healthy individuals meeting the following inclusion and exclusion criteria: between 18 and 45 years of age, body mass index ranging from 23.0 to 32.0 kg/m^2, non-smokers, not pregnant or breastfeeding, have not started or changed birth control in the last 6 months, have not taken antibiotics in the last 6 months, not taking prescription medications including statins and blood pressure medications, no history of chronic disease including diabetes, thyroid disease, metabolic syndrome, irritable bowel syndrome, Crohn's disease, ulcerative colitis, any inflammatory disease, hypertension, cancer, or cardiovascular events, do not have anemia or difficulty with blood draws, typically consume one or less alcoholic drinks per day and participate in binge drinking (more than three alcoholic drinks in one episode) at most one day per month, agree to abstain from alcohol for two days before their blood draw, had not experienced any immunosuppression at the time of enrollment, and had not experienced cold or flu two weeks prior to the blood draw. The subject characteristics including their lipid profiles are summarized in Supplementary Table 2.1. The study was approved by the Institutional

Review Board of UC Davis. The study followed all approved guidelines for the protection of subjects and is registered with ClinicalTrials.gov with NCT #03785860. Participants who qualified for the study were enrolled in the study and provided written informed consent. After consent subjects were scheduled for a visit to the Ragle Human Nutrition Research Center on the UC Davis campus. A fasting blood draw was performed from the antecubital vein into ethylenediaminetetraacetic acid (EDTA) evacuated tubes, immediately centrifuged (1500*g*, 10 min, 4 ℃), portioned into aliquots, and stored at -80 ℃. Baseline plasma from the first ten subjects recruited into this study were used to generate a plasma pool. Frozen plasma samples were thawed on ice for 2 h, combined in a sterile 50 ml falcon tube (Fisher Scientific), stir-mixed, separated into 500 microliter aliquots, and stored at -80℃ until analysis.

Supplementary Table 2.1. Anthropometrical and metabolic biomarker measurements of participants recruited for plasma pool generation. Average +/- standard deviation values for glucose, insulin, total cholesterol, HDL-cholesterol, LDL-cholesterol, and triglyceride of the 20 individuals whose plasma was pooled to generate the pooled plasma sample used in this study.

Measurement	average	standard deviation
Age (y.o.)	27.2	6.0
Weight (kg)	75.5	10.1
Height (m)	169.3	8.9
BMI	26.3	2.8
Systolic BP (mmHg)	113.5	7.5
Diastolic BP (mmHg)	74.1	5.6
Glucose (mg/dL)	83.1	6.9
Insulin (µU/mL)	6.4	3.8
total cholesterol (mg/dL)	171.0	23.5
HDL-cholesterol (mg/dL)	51.8	10.1
LDL-cholesterol (mg/dL)	106.7	20.6
Chol:HDL	3.4	0.7
TG (mg/dL)	63.0	33.7
non-HDL-cholesterol (mg/dL)	119.3	23.8

Additional samples were used to demonstrate the repeatability of the method. These samples are pooled plasma from the Extracellular RNA Communication Consortium (ERCC2) project, which is an NIH Common Fund project aimed at the development of isolation and characterization methods for extracellular RNA carriers (https://commonfund.nih.gov/exrna), including extracellular vesicles and lipoproteins. Plasma was obtained from healthy adult participants in San Diego, CA under an approved IRB from the University of California San Diego. Frozen, de-identified plasma from 25 individuals (men and women) was thawed on ice for 2 h, combined in a sterile 50 ml falcon tube (Fisher Scientific), stir-mixed, separated into 500 microliter aliquots, and stored at -80℃ until analysis.

Ultracentrifugation for separation of chylomicron/VLDL and plasma proteins

Density solutions were prepared at 1.0060 g/ml (1.095% potassium bromide (KBr) w/w in HPLC grade water), 1.2100 g/ml (9.439% KBr w/w in HPLC grade water), and 1.3400 g/ml (59.112% KBr w/w in HPLC grade water), (±0.0005 g/ml) using anhydrous KBr (Sigma-Aldrich, MO, USA). The density of prepared KBr solutions was measured at ambient temperature (22.8 ℃) with a Densito 30PX Densitometer (Mettler Toledo, OH, USA) in triplicate. The density solutions were filtering through a 0.22 µm filter into a sterile bottle. Plasma samples in 500 µL aliquots were thawed at 4 ℃ for 16 h followed by pipet-mixing. The 500 µL homogeneous plasma was underlaid beneath 4.1 mL 1.0060 g/mL KBr density solution in a 4.7 mL OptiSeal tube (Beckmann-Coulter, IN, USA). Extra 1.0060 g/mL KBr solution was added to the top of the tube until the surface meniscus reached the neckline of the OptiSeal tube. The filled OptiSeal tube was then sealed with a disposable plug that is complementary with the OptiSeal tube, and securely locked by a spacer (Beckmann-Coulter). The layered solution was

then loaded onto a fixed angle rotor (TLA-110 Fixed-Angle Rotor, k factor = 13, Beckman-Coulter) and centrifuged at 110,000 RPM (657,272*g*) in a Beckman Optima MAX-TL ultracentrifuge (Beckmann-Coulter) at 14 ℃ for 30 minutes. After centrifugation, the top 1 mL layer was removed with the tip of a pipette drawing solution from the surface while rotating the OptiSeal tube, then the tube was cut below the neck with tubing cutter to expose the remaining solution for accessibility, and 3 additional milliliters were removed to ensure floating particles were removed. The removed 4 mL layer containing chylomicron and VLDL could be saved for future use. To isolate the plasma proteins, the remaining 700 µL fraction containing HDL, LDL, albumin, and plasma proteins was then fully mixed with 1.1 mL 1.340 g/mL KBr density solution by pipetting. The 1.9 mL homogeneous solution was then underlaid carefully beneath 2.8 mL 1.210 g/mL KBr density solution in an OptiSeal tube. Extra 1.210 g/mL KBr solution was added from the top to fill the solution until the surface meniscus reached the neckline of the OptiSeal tube. The OptiSeal tube was sealed and locked as described above, and steadily loaded onto the same rotor, and centrifuged using the same parameters for 3.5 h.

In order to assess the effectiveness of the SEC purification step of this method, an additional UC-only isolation, using the same equipment and supplies as described above, was carried out on a subset of 2 individuals at 2 time points (a total of 4 samples). The samples were first adjusted to the LDL density cutoff of 1.063 g/mL with KBr solution (d = 1.340 g/mL) and the adjusted plasma was overlaid with KBr solution (d = 1.063), followed by ultracentrifugation at 110,000 rpm for 3 h 10 min to isolate the combined chylomicron, VLDL and LDL fraction, and removal by aspiration of the supernatant. The remaining fraction was then adjusted to 1.210 g/ml with KBr solution (d = 1.34 g/mL) and overlaid with KBr solution (d = 1.210 g/mL),

followed by a second ultracentrifugation at 110,000 rpm for 3 h 20 min. The HDL fraction (1.063-1.210 g/mL) was then carefully collected by pipette from the top of the tube.

Dialysis and size-exclusion chromatography

After the second UC step, the top 2 ml of the solution was collected carefully by pipette while slowly turning the tube and mixed with 2 ml of molecular grade 1X Phosphate Buffered Saline (1XPBS, [NaCl]: 137mM; [KCl]: 2.7; [Na_2HPO_4]: 10 mM; [KH_2PO_4]: 1.8 mM) (Sigma-Aldrich). The mixture was filtered through an Amicon Ultra-4 50kDa centrifugal filter (Millipore) at 4,500 RPM (1,100*g*) for 8 minutes using a Sorvall Legend XF centrifuge (Thermo Fischer Scientific, MA, USA). The HDL fraction was reconstituted to 250 µL with millipure water and then transferred to an amber glass vial for FPLC analysis.

Samples were separated with a single Superdex 200 Increase 10/300 GL agarose-crosslinked column (GE Healthcare) on an AKTA P-920 FPLC (Amersham Biosciences). Two hundred microliters of each sample were injected into the system under isocratic elution (1.0 mL/min, 1XPBS.), the first 6.5 mL were discarded, then a 1.5 mL-fraction (including a 0.5 mL void volume) was collected (F0), followed by collection of 6 1-mL fractions (F1-F6) and 1 0.5-mL fraction (F7, excluding a 0.5 mL void volume). The elution was measured continuously at 280nm UV absorbance, and temperature, conductivity and pH were recorded. UV absorbance was used as a proxy for particle concentration to visually confirm fractionation of the LDL, HDL, and albumin peaks. The eight collected fractions correspond to the pre-LDL fraction (F0), the LDL peak (F1–F2), the HDL peak (F3–F6) and the albumin peak (F7). Each fraction was dialyzed in an Amicon Ultra-4 50kDa centrifugal filter (Millipore) at 4,500 RPM (1,100*g*) for 8 minutes.

In order to evaluate the reproducibility of our method across different subjects with different lipid profiles, individual plasma samples from three healthy participants whose plasma was used to generate the plasma pool was selected, and their HDL isolated using a fractionation plan manually adjusted to the elution volume at which the troughs between the LDL and HDL peaks, and between the HDL and albumin peaks were present. This was a different fractionation plan compared to the 1-mL fractionation described above, and it was set this way to maximize HDL yield and minimize the inclusion of albumin and other small molecules. For these three individual subjects the LDL fractions (F1 and F2) were manually set at between 8.85 mL and 9.78 mL, the HDL fractions (F3 and F4) were manually set at between 9.78 mL to 13.26 mL, and the albumin fraction (F5) was manually set at between 13.26 mL and 15.00 mL (Supplementary Figure 2.2).

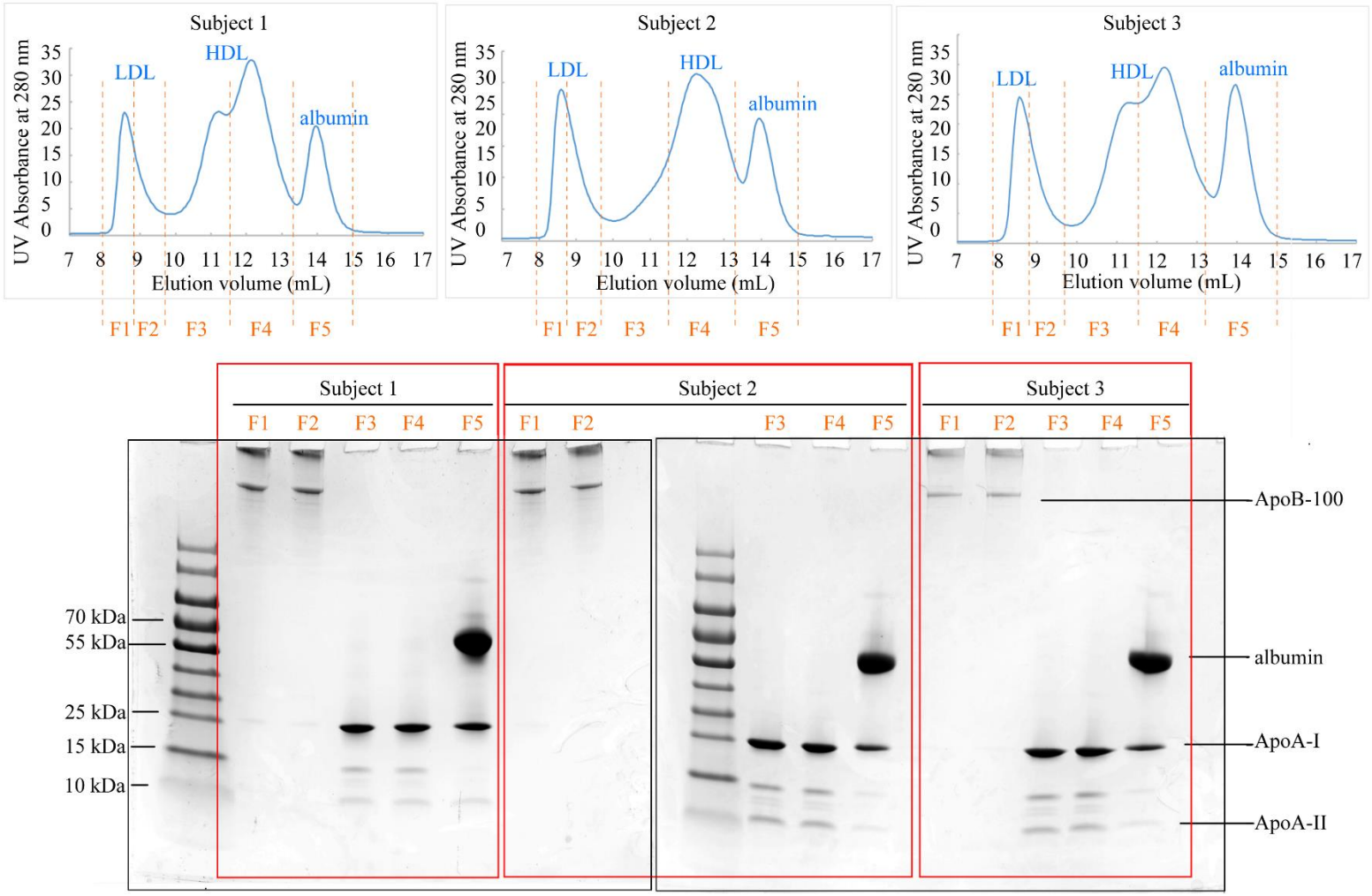
Subject 1
Subject 2
Subject 3
UV Absorbance at 280 nm
Elution volume (mL)
LDL
HDL
albumin
F1
F2
F3
F4
F5
70 kDa
55 kDa
25 kDa
15 kDa
10 kDa
ApoB-100
albumin
ApoA-I
ApoA-II

Figure S2.2: SEC chromatograms and SDS-PAGE images for the isolated LDL fractions, HDL fractions, and albumin fraction from plasma samples from three healthy subjects. Fractionation was slightly adjusted to include two LDL fractions, 7.95-8.85 mL (F1) and 8.85-9.78 mL (F2), two HDL fractions, 9.78 – 11.52 mL (F3) and 11.52 – 13.26 mL (F4), and one albumin fraction, 13.26 – 15.00 mL (F5). Two separate SDS-PAGE gel images are shown in the lower panel. The first gel included Fraction 1-5 from subject 1 and Fraction 1-2 from subject 2. The second gel included Fraction 3-5 from subject 2 and Fraction 1-5 from subject 3. The lanes corresponding to each subject is indicated by the red boxes, and each individual gel is indicated by the black boxes. SDS-PAGE separates the isolates into clear bands of ApoB for LDL fractions, ApoA-I and ApoA-II for HDL fractions, and albumin and ApoA-I in albumin fractions.

In order to evaluate the repeatability of the method over time, we used plasma samples pooled from the ERCC2 project as described above to serve as a quality control standard. This plasma quality control is isolated every 10 samples when running a large batch of samples, representing chromatograms of the same sample over several weeks of individual runs. The elution volume for LDL, HDL, and albumin was determined at the max 280nm UV absorbance for each peak.

Protein Concentration Measurement

Fraction F3-F6 were selected as HDL fractions, and the total protein concentration in these fractions were used to assess the yield of HDL by our isolation method. Protein concentration was determined using a commercially available microBCA Protein Assay kit (Thermo Scientific). Briefly, a standard curve of bovine serum albumin (BSA) with the

concentration of 200, 40, 20, 10, 5, 2.5, 1, 0.5, and 0 µg/mL was prepared in duplicate. One-hundred and fifty microliters of BSA standard or HDL samples were loaded on a clear-bottom 96-well microplate (Greiner Bio-One), and mixed with 150 µL Working Reagent (provided) for a 2-hour incubation at 37°C. After the incubation, the absorbance of the solution was measured at 562 nm and recorded by a SpectraMax M5 microplate reader (Molecular Devices). The absorbance data for the BSA standard were plotted against the BSA concentration to obtain a standard curve. The molar extinction coefficient was determined by the "Trendline" function in Microsoft Excel. The protein concentration in HDL fractions F3-F6 were then calculated by dividing the adjusted absorbance by the molar extinction coefficient of the BSA standards according to Beer's Law.

Verification of purity of the isolated HDL fractions

Detailed protein composition in each SEC fraction was identified by proteomics, which was chosen as an unbiased evaluation of the protein composition of isolated HDL fractions. The isolated HDL fractions were reconstituted with 50 µL of 50 mM ammonium bicarbonate and denatured with the additional 2 uL of 550 µM dithiothreitol. It was then added to the samples and incubated for 50 minutes at 55 °C. The free thiol groups were then alkylated with 4 µL of 450 mM iodoacetamide for 25 minutes at room temperature in the dark. The mixture was digested by adding 2 µg trypsin in 200 µL of 50 mM ammonium bicarbonate and incubated for 18 h at 37 °C. The digested peptides were purified by solid-phase extraction with Supelclean C18 cartridges containing 500 mg sorbent materials (Sigma-Aldrich), and the samples were dried in vacuo using a miVac sample concentrator (SP Scientific, PA, USA). Tryptic digested samples were reconstituted with 20 µL of water and directly characterized using UltiMate WPS-3000RS nanoLC

980 system coupled to the Nanospray Flex ion source of an Orbitrap Fusion Lumos Tribrid Mass Spectrometer (MS) system (Thermo Fisher Scientific). One microliter of the sample was injected, and the analytes were separated on an Acclaim PepMap 100 C18 LC Column (3 µm, 0.075 mm x 150 mm). A binary gradient was applied using 0.1% (v/v) formic acid in (A) water and (B) 80% acetonitrile: 0–90 min, 4–47% (B); 90–100 min, 47–70% (B); 100–101 min, 70%-100% (B); 116–117 min, 100–4% (B). The instrument was run in data-dependent mode with 1.8kV spray voltage, 275 °C ion transfer capillary temperature, and the acquisition was performed with the full MS scanned from 375 to 2000 in positive ionization mode. Higher-energy C-trap dissociation at 35% was applied to obtain tandem MS/MS spectra with *m/z* values starting from 120.

The proteins were identified using Byonic software (Protein Metrics, CA, USA), and the *Homo sapiens* (Human) protein database from UniProt (UP000005640) was used for the protein database file. Carbamidomethyl modification at cysteine residues (set as fixed) and oxidation at methionine (set as variable) were assigned as the modification. The resulting files were further loaded to Byologic software (Protein Metrics) for protein quantification. Proteins detected by a minimum of two unique peptides were used in the analysis. Known typical contaminants of the proteomics process including keratin (K1C14, K2C6B, K2C1, K1C10, K2C5, K1C9, K22E, K2C1B) trypsin (TRY1, TRY3, and TRY6), and protein shroom 3 (SHRM3) were manually excluded from analysis. For each identified protein, the peptide with the highest signal and without any post-translational modifications was chosen as the quantitation peptide. The intensity from the extracted ion chromatogram (XIC) was used for protein quantification.

For SDS-PAGE, samples from each SEC fraction were first adjusted to about 0.4 mg/mL concentration with water. Fifteen microliters of each SEC fraction (F0–F7) were mixed with 15 µl of Lane Marker Reducing Sample Buffer (Thermo Fisher Scientific) and heated on a heat

block (100 °C) for five minutes. Then, the unfolded and reduced fractions were loaded into a 4-20% Mini-PROTEAN Precast polyacrylamide gel (BioRad), with Page Ruler Prestained Protein Ladder (Thermo Fisher Scientific). The gels were run at 120V for about 60 minutes, then removed from the plastic casing, stained with InstantBlue (Sigma-Aldrich) protein stain for 45 minutes, and ChemiDoc MP imaging instrument (Bio-Rad) The image of the gel was then cropped using the Image Lab software.

For native-condition PAGE, the isolated fractions were first diluted into 0.4 mg/mL with water. The solutions were then mixed with native sample buffer (BioRad) in 1:1 (v/v) ratio. Then, 20 mL containing about 5 µg protein from each fraction was loaded into a 4-20% Mini-PROTEAN Precast polyacrylamide gel (Biorad). The sample in each well was run at 25 A for 1 hour with Tris-glycine buffer without SDS (Genessee Scientific, San Diego, CA).

To quantify ApoA-I Western blot was performed. A nitrocellulose membrane (Biorad) was first activated with 100% methanol for 5 seconds on each surface. The activated membrane was then equilibrated in the Western blot transfer buffer (20% methanol, 20% Trans-Blot transfer buffer 5x (Biorad), 60% water (v/v/v). Two transfer stacks were also equilibrated in the transfer buffer for 5 minutes until fully soaked. The Western blot protein transfer sandwich was then assembled in the order of transfer stack, membrane, poly-acrylamide gel, transfer stack from the anode to the cathode in a Trans-Blot Turbo Transfer System case (Biorad). Protein transfer was run by selecting the “mix MW” mode, which provides 1.3 A for 7 minute duration. The membrane was taken out and washed with TBST buffer (10% tris-buffer saline 10x (Biorad) , 0.1% Tween (Biorad) , 89.9% water, v/v/v) for 5 minutes each time, 3 times. The membrane was then incubated in 5% skim milk in TBST buffer for 1 hour, followed by 3 5-minute washes. Ten microliters of primary antibody solution (0.1% mouse anti-human ApoA-I antibody (Invitrogen,

Waltham, MA), 5% bovine serum albumin (Biorad), 94.9% TBST, v/w/v) was added to the membrane for primary antibody incubation at 4 °C for 24 h. After 24 h of primary antibody incubation, the membrane was washed 3 times with TBST buffer, and incubated in 10 mL secondary antibody solution (0.01% goat anti-mouse HRP-linked antibody (Invitrogen), 5% skim milk, 94.95% TBST, v/w/v) for 1 hour at room temperature. The membrane was washed 3 times with plenty of TBST for 5 minute each time, and then 6 mL of HRP substrate (50% Clarity Western Peroxide Reagent, 50% Clarity Western Luminol/Enhancer Reagent) was added on the surface of the membrane. The reaction was captured using ChemiDoc MP imaging instrument (Bio-Rad) under "Chemiluminescent" mode.

Verification of HDL Morphology and Cholesterol Efflux Capability

TEM was performed to visualize the particle morphological characteristics and size in each fraction. Carbon-coated grids (TedPella Inc., CA, USA) were glow-discharged at 30 mA for 30 seconds. Five microliters of fractions F1-F7 from the FPLC were loaded onto the carbon-coated side of the grid, allowed to sediment on the grid for 5 minutes, and blotted with filter paper to remove excess sample. The grid was then washed and stained with 5 µl 2% (v/v) uranyl acetate solution and blotted five times and left to air-dry at room temperature for 2 minutes. The dried grid was transferred onto the specimen cartridge on the specimen holder of the electron microscope (JEOL USA 1230 Transmission Electron Microscope, JEOL USA Inc., MA, USA) and inserted into the electron microscope according to the manufacturer's instructions. The sample is inserted into sthe specimen chamber of the EM after vacuum is maintained. Each specimen was first viewed using the binoculars on the electron microscope under the condition of high tension = 120 kv and Magnitude = 40 K. When a section of the specimen contained a

considerable amount of particles (≥20 particles in view), an image was taken with exposure time = 500 ms. Five images from different grid regions were taken for each specimen.

The cholesterol efflux capability of the isolated HDL was compared to that of a traditionally prepared ApoB-depleted plasma. Cholesterol efflux ability of HDL is known as the best functional assay to examine the atheroprotective capacity of HDL[18]. The experimental procedure was followed according to the protocol of a cholesterol efflux assay kit (Abcam, United Kingdom) with some modifications. Briefly, THP-1 human macrophage cells were plated into a microplate at a concentration of 10^5 cells/well. The cells were then activated using 100 µL RPMI with 10% fetal bovine serum and 40 nM (64 ng/mL) phorbol-12-myristate 13 acetate (PMA) and incubated for 24 h at 37°C and 5% CO_2 . After incubation, cells were washed with 1X PBS, and incubated with serum-free RPMI and labeling reagent (3:1) provided by the commercial kit for 4 hours. After incubation, the labeling reagent was discarded, the wells were washed with 1X PBS, and serum-free RPMI with isolated HDL at 0.1 mg/mL of total protein concentration, measured by microBCA (Thermo Science) or ApoB-depleted plasma were loaded into the designated well. The plate was then incubated for 4 h. After incubation, the supernatant portion in each well was transferred to a new plate. The remaining cells in the wells were lysed with mammalian protein extraction reagent (Thermo Scientific, USA). Fluorescence emission of both the supernatant and the cell lysis portion were measured at 515 nm after 482 nm excitation. The cholesterol efflux to the cholesterol acceptor (HDL or ApoB-depleted plasma) was calculated by dividing the supernatant fluorescence emission by the sum of the fluorescence emission of the supernatant and cell lysis fractions.

4. RESULTS

The HDL isolation method described here yields a set of highly purified HDL fractions that can either be combined to yield a single pool of total HDL or be used as distinct size-based subfractions of HDL. The total protein concentration in the 100 µL concentrated combined HDL fraction (F3-F6) was measured by microBCA protein assay to be 4.2 ± 0.1 mg/mL (Figure 2.3a). (a total of about 400 µg protein).

As shown in the SEC chromatogram (Figure 2.3b), the HDL particles eluted as a distinct double peak (F3–F6) with a smaller peak in fraction F4 and the apex of the peak in fraction F5, after LDL (fractions F1–F2) and before albumin (fraction F7).

The technical repeatability of the method was assessed by isolation of lipoproteins from a single plasma pool on 8 separate days over the course of multiple weeks (Figure 2.3c). The mean ± standard deviation peak elution volume for the LDL peak, HDL peak, and albumin peak are 8.28±0.0071, 11.7±0.027, and 13.6±0.029 mL, respectively. The % coefficient of variation of these peak elution volumes are 0.09%, 0.23%, and 0.21%, respectively, confirming a high degree of repeatability and column performance.

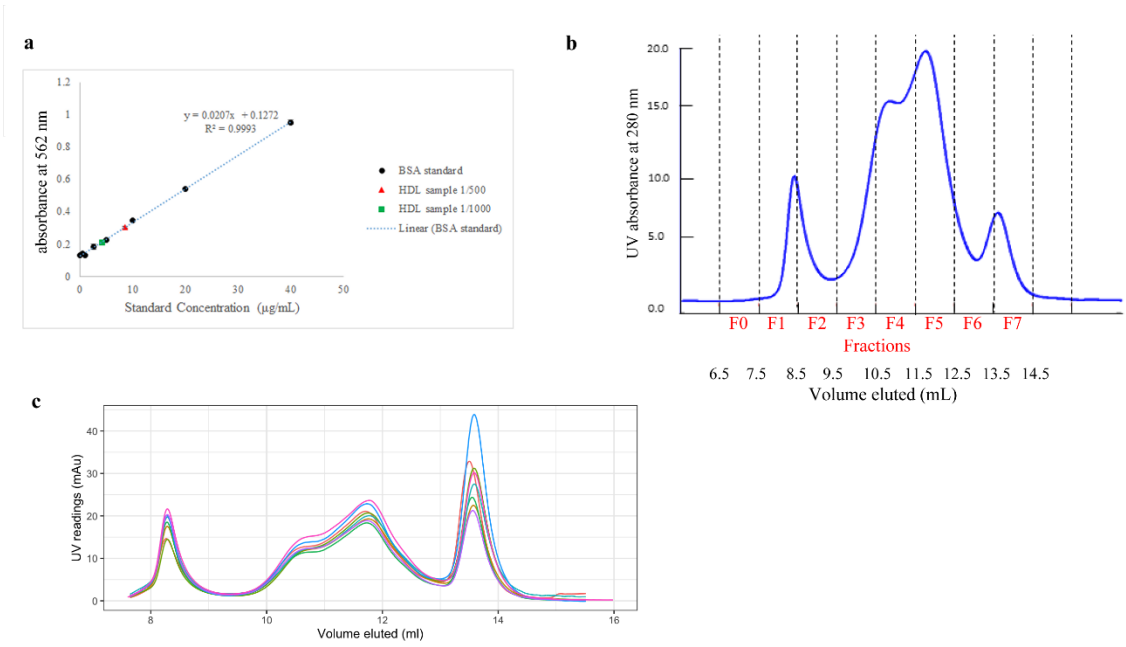

Figure 2.3. Overall HDL total protein concentration of size exclusion chromatography (SEC) fractions with SEC chromatogram. a) The total protein concentration of diluted HDL samples (500- and 1000-times) calculated from a fitted bovine serum albumin standard curve. The concentration for the 500- and 1000-times diluted HDL samples were calculated to be 8.57±0.31 µg/mL and 4.08±0.17 µg/mL, respectively. b) SEC chromatogram of pooled plasma sample following sequential flotation ultracentrifugation, with fractionation set to collect 1-mL fractions starting at 6.5 mL. Fractions F1 and 2, correspond to the low density lipoprotein (LDL) particle size range; Fractions F3-6, correspond to the high density lipoprotein (HDL) particle size range, with fraction F6 containing a portion of the albumin peak; Fraction F7 corresponds to the albumin peak. c) A chromatogram showing 8 repeated SEC on plasma aliquots from a plasma pool on several different days to demonstrate the technical reproducibility of the separation procedure. The mean ± standard deviation peak elution volume for the LDL peak, HDL peak, and albumin peak are 8.28±0.007, 11.7±0.027, and 13.6±0.029 mL, respectively. The % coefficient of variation of these are 0.09%, 0.23%, and 0.21%, respectively.

In order to assess the reproducibility of the method across individual participants who may have different lipid profiles and lipoprotein particle size distributions, plasma samples from 3 healthy individuals from the 10 subjects whose plasma samples were used to generate the plasma pool were isolated using a fractionation approach described in the methods section that was aimed at isolating the LDL, HDL, and albumin peaks at their troughs. (Figure S2.2, upper panels). SDS-PAGE was run for each fraction from each individual, and showed that the LDL fraction consistently contained ApoB, the HDL fractions consistently contained ApoA-I with no albumin, and the albumin fraction consistently contained albumin (Figure S2.2).

It is important to note that with this fractionation approach of collecting at the trough between the HDL and albumin peaks, the HDL fractions excluded albumin but there was detectable ApoA-I in the albumin fraction, indicating that some amount of the smallest HDL particles elute in the albumin peak. With this fractionation the elution from 9.78-11.52 mL and 11.52-13.26 mL was denoted as the HDL1 and HDL2 fractions, and that within 13.26-15.00 mL elution volume was labeled as the albumin fraction. In order to determine the extent of loss of HDL particles into the albumin fraction we performed a Western blot using anti-human ApoA-I antibody on the albumin fraction after denatured- and native-condition PAGE. Figure 2.4a shows that after denatured PAGE, the albumin fraction contains significant amounts of albumin and much lower amounts of ApoA-I stained by Coomassie blue. The Western blot of this gel shows a minor ApoA-I band in the albumin fraction (lane 3) compared to the ApoA-I bands in the HDL1 and HDL2 fractions (lanes 1 and 2) (Figure 2.4b). The densities of the ApoA-I bands in each lane are 41%, 54%, and 5% of the total density respectively for HDL fraction 1, HDL fraction 2, and the albumin fraction (Figure 2.4c), demonstrating that about 5% of total ApoA-I was

excluded from the HDL1 and HDL2 fractions when the fractionation cutoff was chosen at the trough between the HDL and the albumin peaks. We next determined whether the 5% of ApoA-I that was lost into the albumin fraction from the HDL fractions likely represented free ApoA-I or ApoA-I attached to HDL particles, and if the latter, whether the particles were a subset of particles that was completely different from and unrepresented by those found in the HDL fractions. Using native-condition PAGE we found a range of particles that migrated higher in the gel, consistent with larger HDL particles, as expected in the HDL1 fraction (lane 1), a range of particles that migrated lower in the gel, consistent with smaller HDL particles, as expected in the HDL2 fraction (lane 2), and a major band migrating below the smaller HDL particles in the albumin fraction (lane 3) (Figure 2.4d), corresponding to albumin. The Western blot using an ApoA-I antibody on this native gel showed very little signal for ApoA-I in the albumin fraction compared to the two HDL fractions (Figure 2.4e). The density of the ApoA-I band in the albumin fraction was 3% of the total ApoA-I signal, compared to 47% in HDL fraction 1 and 50% in HDL fraction 2 (Figure 2.4e). Moreover, the ApoA-I stained band in the albumin fraction (lane 3) overlaps with the lowest portion of the band in the HDL2 fraction (lane 2), indicating that the HDL particles present in the albumin fraction are likely to be the smallest HDL particles that are included in the range of particles found in the HDL2 fraction, rather than a separate particle type with a different gel migration pattern as determined by native PAGE. Together, these data confirm that with the isolation method described in this paper using fractionation at the trough between the HDL and albumin peaks there is minimal loss of HDL particles into the

albumin fraction, with an estimated 97% of particles being captured in the HDL fractions.

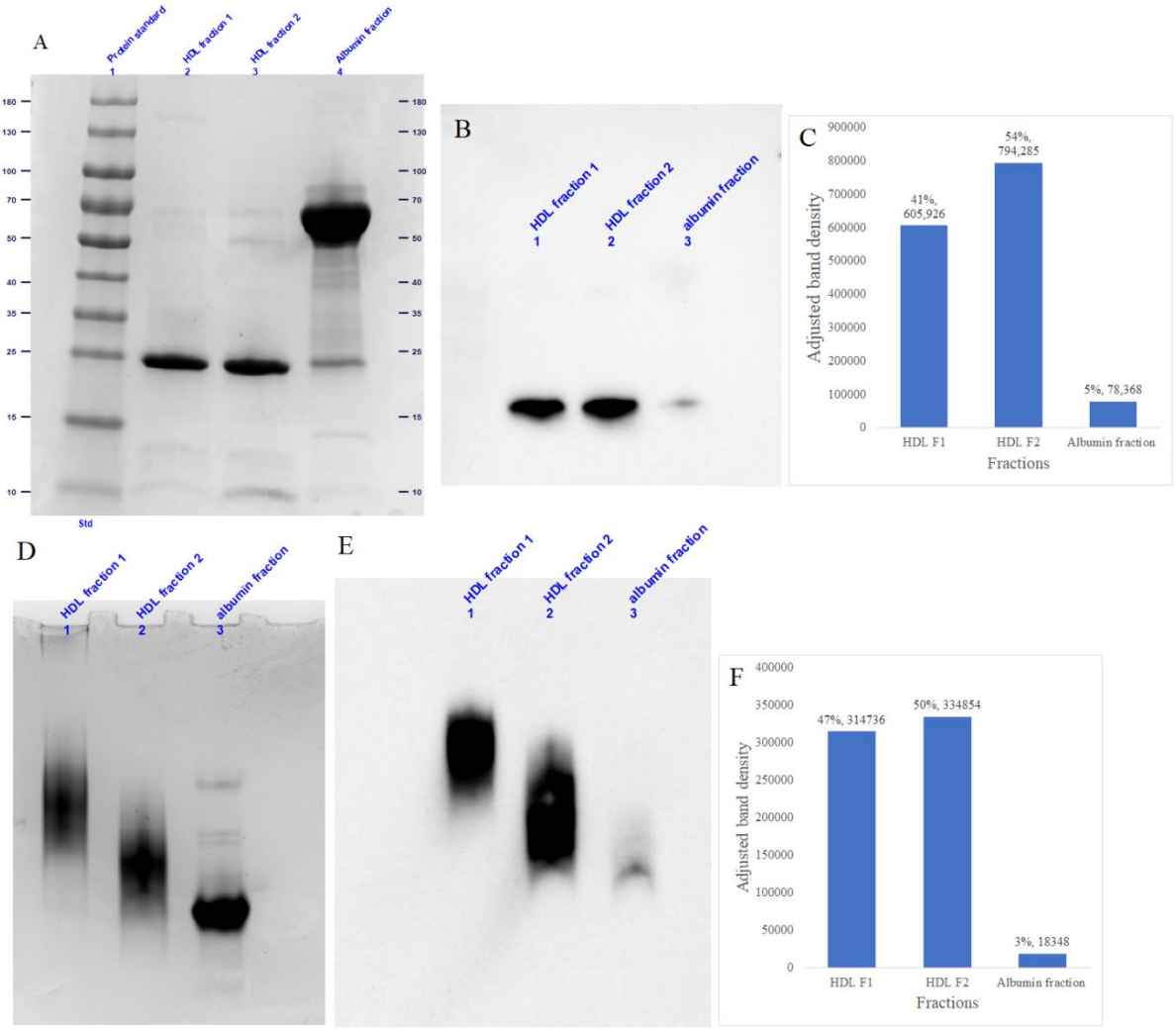

Figure 2.4. Sodium dodecyl sulfate (SDS)- and native- polyacrylamide gel electrophoresis (PAGE) and Western blot analysis on HDL fraction 1, HDL fraction 2, and albumin fraction. A) SDS-PAGE stained with coomassie blue protein stain. B) Western blot membrane showing ApoA-I proteins transferred from the gel shown in (A). C) The relative and absolute value of band density of each ApoA-I band in the Western blot shown in (B). D) Native-PAGE stained with coomassie blue protein stain. E) Western blot membrane showing ApoA-I proteins transferred from the gel shown in (D). F) The relative and absolute value of band density of each ApoA-I band in the Western blot shown in (E).

In order to obtain an unbiased assessment of all proteins present in each fraction, proteomics was performed using liquid chromatography-mass spectrometry/mass spectrometry (LC-MS/MS Orbitrap). A total of 48 proteins were detected across all eight SEC fractions (F0-F7, Supplementary Table 2.2). Figure 2.5a shows the XIC distributions of ApoA-I, ApoB, and albumin across the SEC fractions. Of the total ApoA-I detected across fractions F0-F7, most of the ApoA-I was found in fractions F3, F4, F5, and F6 respectively which corresponded to the fractions that were expected to contain the HDL particles according to the SEC chromatogram (Figure 2.3b) and according to the particle size that is expected to elute in that elution range based on the protein calibration standards (Supplementary Figure 2.1). In line with previous literature showing that ApoA-I makes up 60-70% of the total protein in HDL particles [15], ApoA-I was the most abundant protein constituent in fractions F3, F4, F5, and F6, respectively (Supplementary Table. 2.2). The majority of the protein mass in fraction F6 is albumin, indicating that this smallest fraction of HDL is the most contaminated with albumin. However, as seen in the chromatogram (Figure 2.3b), the fractionation that was carried out collecting 1mL fractions, resulted in the collection of a substantial portion of the albumin peak in fraction F6. Fraction F5 had the highest total intensity for ApoA-I and corresponded to the apex of the HDL peak on the SEC chromatogram. Both F4 and F5 had limited signal for ApoB-100 or albumin, which were several magnitudes lower than that of ApoA-I, indicating that F4 and F5 are the purest and most abundant among the 4 HDL fractions. Only a small proportion of total ApoA-I was detected in fractions F2 (LDL fraction) and F7 (albumin fraction) indicating minimal loss.

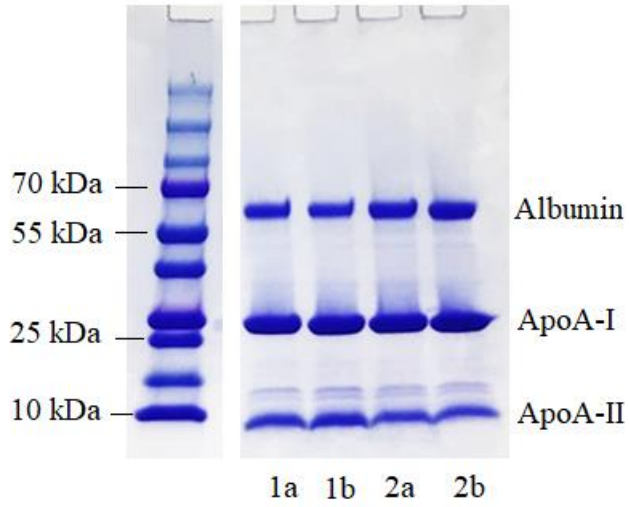

Figure S2.1: SDS-PAGE image for HDL fractions isolated by sequential floatation ultracentrifugation only. Lanes labeled 1a, 1b, 2a, and 2b were from two different subjects. The gel image shows clear bands for albumin (around 65 kDa)), ApoA-I (around 28 kDa)), and ApoA-II (around 11 kDa).

ApoB was detected primarily in SEC fractions F1 and F2, corresponding to the LDL peak. ApoB abundance diminished by two orders of magnitude relative to fractions F3-6, the major HDL-containing fractions (Figure 2.5b). Albumin was detected in SEC fractions F6, the last HDL fraction which also captured approximately half of the albumin peak, and F7 the fraction containing the albumin peak on the SEC chromatogram. Albumin is nearly undetectable in the rest of the SEC fractions (Figure 2.5c).

In order to determine the compositional heterogeneity of the four HDL fractions, we examined the content of 12 key HDL-associated proteins and their distribution across the SEC fractions, ordered according to their elution time (Figure 2.5). Clusterin (CLUS), also known as apolipoprotein J, was found to be enriched in the LDL-containing fraction F2 and the largest

HDL fraction F3, with 6 times less found in the later SEC fractions (F4-5) and no detectable levels in the smallest HDL fraction F6 or the albumin fraction F7 (Figure 2.6a). Apolipoprotein E (ApoE) was found at highest intensity in fractions F3-4, corresponding with the larger HDL particles, and also LDL fraction F2, with a much smaller intensity in the large LDL fraction F1 (Figure 2.6b). Phospholipid transfer protein (PLTP) was enriched in the large HDL fraction F3, followed by the LDL fraction F2, with 3 times less PLTP in HDL fraction F4 and no detectable levels in any of the other fractions (Figure 2.6c). Lecithin-cholesterol acyltransferase (LCAT) was found exclusively in HDL fractions F3-5, with the highest intensity found in fraction F4 (large HDL particles), half of the amount was found in fraction F3, and 7 times less found in faction F5 (Figure 2.6d). Apolipoprotein C-III (ApoC-III) has a distinct distribution pattern, with an increasing intensity of ApoC-III across the larger HDL fractions F3-5 reaching its peak in fraction F5, and 10-fold less ApoC-III in the small HDL fraction F6 and in the LDL fraction F2 (Figure 2.6e). Paraoxonase 1 (PON1) was distributed across HDL fractions F3-6 with the highest intensity found in fraction F4, and indicating that PON1 may be enriched in the larger HDL particles (Figure 2.6f). Apolipoprotein A-IV (ApoA-IV) was distributed across HDL fractions F3-5, with the highest intensity detected in fractions F3 and especially F4 corresponding to the larger HDL particles, and none found in the small HDL fraction F6 but low intensity found in the albumin fraction F7 (Figure 2.6g). ApoA-II was the second most abundant protein, and its distribution across fractions F3-6 indicates its presence across all of the sizes of HDL (Figure 2.6h). Serum amyloid A1 (SAA1) was enriched in fraction F5, corresponding to the apex of the HDL peak, with approximately 10-fold lower intensity in fraction F4, the larger HDL particles, and about 2 orders of magnitude less SAA1 in fraction F6, the smallest HDL, and no detectable levels found in the LDL or albumin fractions (Figure 2.6i). Alpha-2-HS-glycoprotein (A2HSG),

or fetuin, was found exclusively in fraction F6, corresponding to the smallest HDL, with no detectable level in any of the other fractions (Figure 2.6j). Alpha-1-antitrypsin (A1AT) was found at low intensity in HDL fractions F3-5, peaking in fraction F4, and at about 10-fold higher intensity in fractions F6, corresponding to the smallest HDL, and F7, corresponding to albumin, indicating a bimodal distribution for A1AT (Figure 2.6k). Vitamin D binding protein (VDBP) on the other hand, was enriched in the smallest HDL fraction F6 and in the albumin fraction F7, with approximately 4 times less found in fraction F5, and no detectable levels in fractions F1-4 (Figure 2.6l).

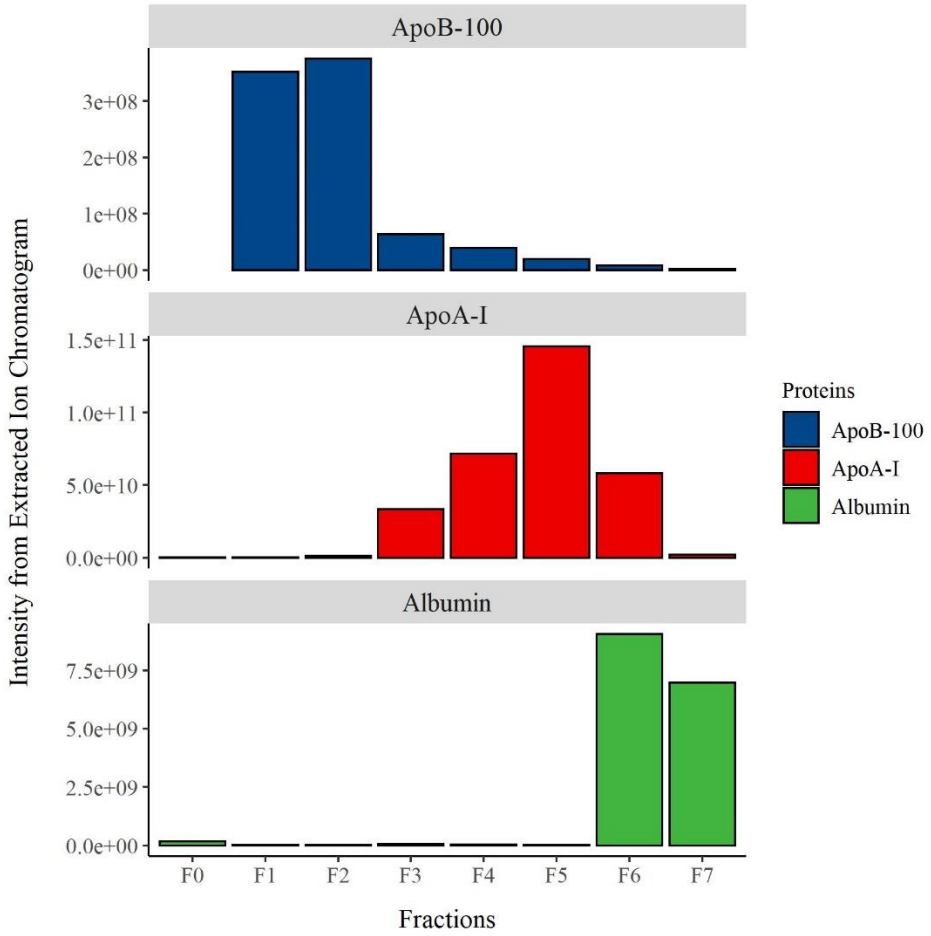

Figure 2.5. Signal intensity from liquid chromatography-mass spectrometry (LC-MS). Intensity from Extracted Ion Chromatogram (XIC) for A) Apolipoprotein B-100 (ApoB-100), B)

ApoA-I, and C) albumin in SEC fractions F0-F7 corresponding to collected low density lipoprotein (LDL), high density lipoprotein (HDL), and albumin (Alb) fractions.

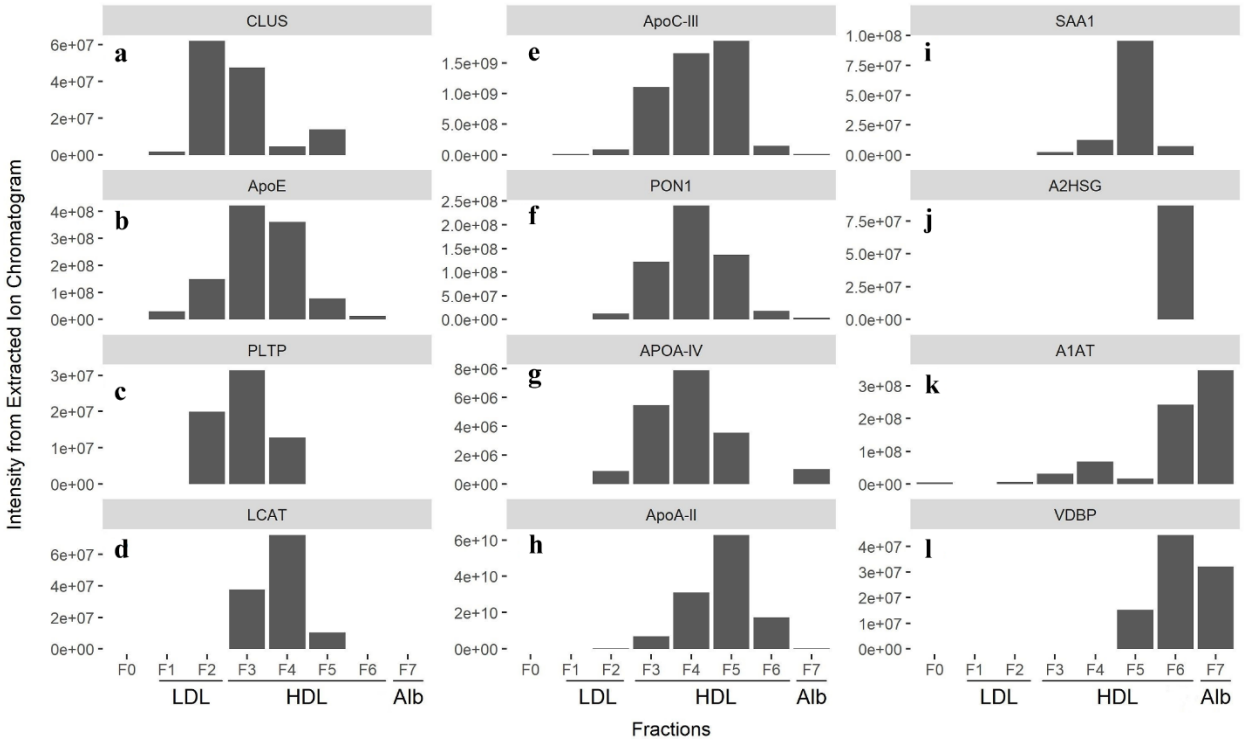

Figure 2.6. Signal intensity from Extracted Ion Chromatogram (XIC) for 12 selected HDL-associated proteins. A) clusterin (CLUS), B) apolipoprotein E (apoE), C) phospholipid transfer protein (PLTP), D) lecithin cholesterol acyl transferase (LCAT), E) apolipoprotein C-III (apoC-III), F) paraoxonase 1 (PON1), G) apolipoprotein A-IV (ApoA-IV), H) apolipoprotein A-II (ApoA-II), I) serum amyloid A1 (SAA1),J) α-2-HS-glycoprotein (A2HSG), K) α-1-antitrypsin (A1AT), and L) vitamin D binding protein (VDBP). The proteins are displayed such that those enriched in the early fractions corresponding to larger particles are shown in the left column, those distributed across all HDL fractions are shown in the middle column, and those enriched in the later fractions corresponding to smaller particles are shown in the right column. Proteomic

analysis for fractions F0–F7 was performed, with fractions F1-F2 corresponding to the low density lipoprotein (LDL) peak, F3-F6 corresponding to the high density lipoprotein (HDL) peak, and fraction F7 corresponding to the albumin (Alb) peak.

In addition to the XIC data, the full spectral count data generated from the proteomic analysis were included to provide a more comprehensive characterization of the proteins detected in each HDL fraction (Supplementary table 2.3). In addition, the spectral count data for each HDL fraction from this study were compared to a few of those reported in previously published studies (Supplementary Table 2.3). Compared to other published data, the current HDL isolation method yields higher total peptide counts for ApoA-I in all four HDL fractions (F3-6), and ApoA-II in fractions F4 and F5. ApoB total peptide counts are intermediate among the published data selected. Albumin peptide counts are significantly lower in HDL fractions F3, F4, and F5 compared to the majority of previously published data. Likewise, the peptide counts comparison table also shows a significantly lower amount of IgG found in all HDL fractions compared to previously published data.

In order to assess the effectiveness of the SEC step after UC, we carried out an additional SDS-PAGE analysis of the HDL fractions obtained after UC only (Figure S2.1). The results showed that HDL isolation by UC only without SEC yielded a fraction containing HDL, as indicated by the presence of ApoA-I and ApoA-II (Figure S2.1). However, there was significant albumin contamination, showing that albumin represented approximately 50% of the total protein content in these fractions. Published UC-only techniques typically contain albumin to ApoA-I ratios of approximately 1:3[3], whereas our method produced albumin to ApoA-I ratios of 1:50 to 1:195 in fractions F3-F5 respectively.

Some previous HDL isolation methods may disrupt the structural integrity of HDL particles, making them unsuitable for functional analyses where intact particles are needed. We investigated the morphology and size of the isolated particles in the LDL and HDL fractions using TEM. The literature-established size range for HDL was reflected in TEM imaging of the individual fractions (Figure 2.7). Fractions F1 and F2 showed particles distinctly larger than F3-F6, approximately 20-30 nm in diameter (Figure 2.7a and b), aligning with the literature consensus for LDL particle size [13,19-21]. Fractions F3-F6 (Figure 2.7c-f) had distinctly smaller particles than fractions F1 and F2, which fell within the accepted range for HDL diameter, 8-12 nm [13]. Consistent with the size-resolving nature of SEC, the particles visibly diminished in diameter from F3 to F6. Fraction F2 had a mixture of large particles over 20nm, and small particles under 20nm, indicating that some HDL-sized particles were co-eluting in the LDL fraction. Importantly, the TEM results indicate that the particles remained structurally intact after the isolation procedure, with a lack of contaminating aggregates and large particles in the HDL fractions.

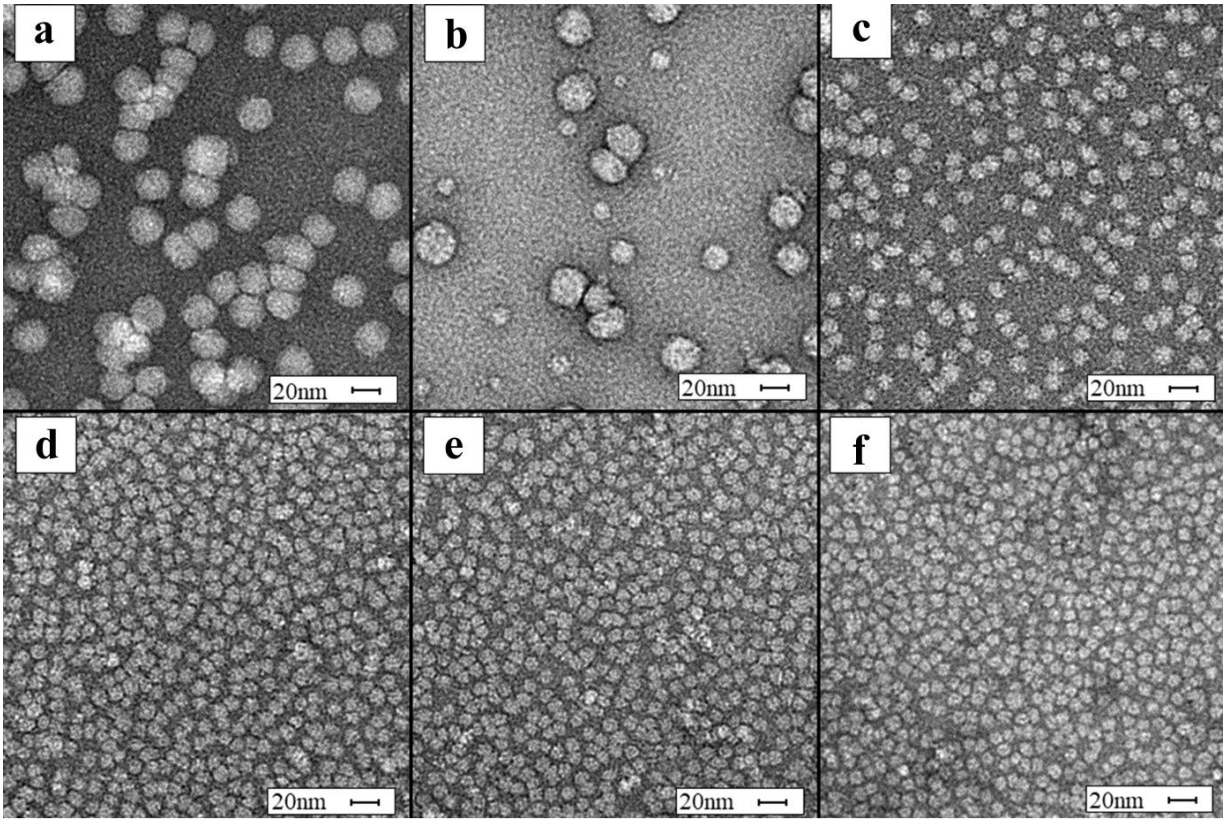

Figure 2.7. Transmission electron microscopy micrographs of size exclusion chromatography (SEC) fractions. All fractions are displayed with a size bar of 20nm. A) Fraction F1 shows particles ranging in size from 18-28nm. B) Fraction F2 shows primarily particles in the size range of 18-28nm, and some particles in the size range of 7-12nm. C) Fraction F3 shows particles in the size range of 7-18nm, D) Fraction F4 shows particles in the size range of 7-15nm, E) Fraction F5 shows particles in the size range of 7-12nm, and F) Fraction F6 shows particles in the size range of 7-10nm. Fraction F7 is not displayed because no particles were visible in this fraction.

In order to determine the suitability of the method for producing functionally intact particles the cholesterol efflux capacity of the isolated HDL particles was measured and compared to the cholesterol efflux capacity of the ApoB-depleted fraction from the same starting plasma. The cholesterol efflux capacity of the isolated HDL particles was comparable to that of

ApoB-depleted plasma at the same protein concentration level (Figure 2.8), indicating that the HDL isolated by this method are functionally intact when tested in a cellular assay.

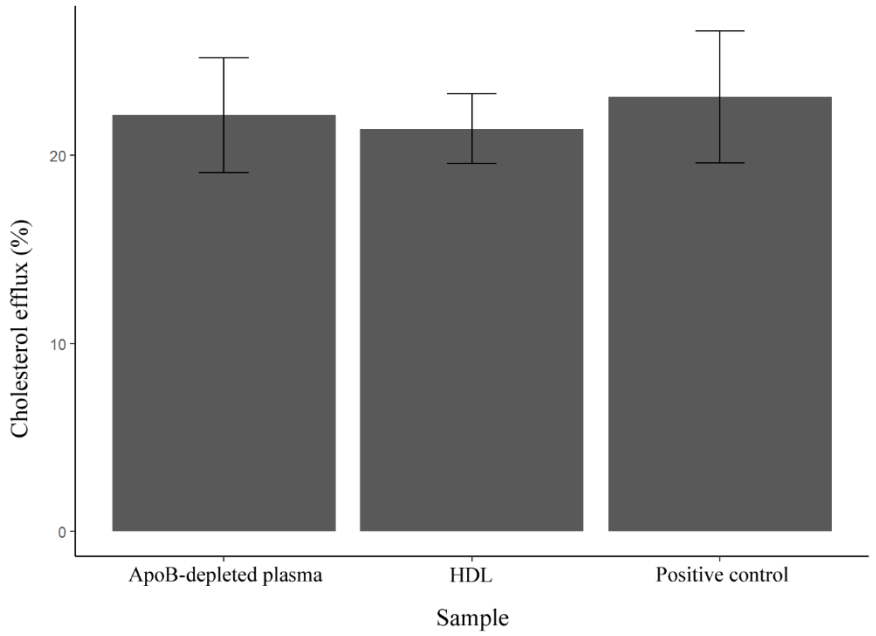

Figure 2.8. Comparison of the cholesterol efflux capacity of isolated HDL, ApoB-depleted plasma, and a positive control. HDL samples isolated by the current method has a comparable cholesterol efflux capacity (21.4±1.3 %) compared to that of ApoB-depleted plasma (22.1±2.5 %) or a positive control (23.1±2.9 %).

5. DISCUSSIONS

With this HDL isolation method we endeavored to optimize 4 critical objectives simultaneously: 1) Obtain highly purified fractions of HDL that are free of both contaminating larger particles (e.g. LDL) and contaminating plasma proteins (e.g. albumin, immunoglobulin G, other proteins); 2) obtain structurally and compositionally intact particles that are free of salts, chemicals, antibodies, lipid binding agents, and other contaminants that are artifacts of the

particle isolation process, so that they are amenable for a variety of downstream compositional and functional analyses; 3) obtain a high yield of HDL particles so that multiple compositional and/or functional analyses can be performed on the same sample and 4) achieve the first 3 objectives with a method that requires low starting plasma volume of 500 µL and that simultaneously preserves the other fractions that contain biologically significant particles. The 500 µL starting plasma volume is optimal in terms of HDL yield for the purpose of collecting a single HDL isolate that can be split into multiple aliquots for multiple compositional, structural, and functional analyses, yet is an acceptable starting volume in most situations including for studies using precious samples from biorepositories and large cohort studies. For example, depending on the plasma sample, on average 400 µg of total protein in the HDL fractions can be obtained from 500 µL plasma sample, and this will provide adequate HDL for several down-stream analyses including for example, cholesterol efflux assay (50 µg), SDS-PAGE/Western blot (10 µg), transmission/cryo-electron microscopy (1-10 µg), proteomics analysis (50 µg) and more. However, in situations where the starting plasma volume needs to be less than 500 µL, plasma can be simply diluted with d=1.006 g/mL density solution and similar separation can be achieved, albeit with reduced HDL yield.

The results demonstrate minimal contamination by albumin, other plasma proteins, or by ApoB in the HDL fractions F3-F5, with albumin elution in fraction F6 due to this fraction containing a substantial portion of the albumin peak, when using the 1-mL fractionation. However, when using the fractionation approach that collects fractions at the peak troughs, there is no detectable albumin in the HDL fractions (Figure 2.4). Failure to deplete plasma proteins, especially albumin, from HDL isolates is a pervasive problem seen in common HDL isolation methods. For example, with the ApoB depletion methods, which utilize polyethylene glycol

(PEG), dextran sulfate, or $MgCl_2$ [22], although ApoB-containing lipoproteins are effectively depleted, significant amounts of plasma proteins including albumin and immunoglobulins remain [23]. The ApoB-depletion method has the advantages of being fast, easy, and cheap to perform, and may be adequate for quantifying cholesterol and lipidomic analysis of HDL, since the contaminants may not pose significant interference on the analytical results, as the plasma proteins carry little, if any, lipids. However, proteomics analysis and biological functional analysis of HDL require HDL samples high in purity and devoid of functional plasma proteins that can potentially confound the results.

Proteomics was used as an unbiased approach to determine the presence of expected proteins, absence of contaminating proteins, and to estimate the relative abundance of proteins within each of the isolated fractions. The main proteins associated with each particle class, Apo-B for LDL, ApoA-I for HDL, and albumin were enriched in the expected fractions corresponding to the expected elution time based on the SEC protein calibration standards (Figure S2.3; Figure 2.5).

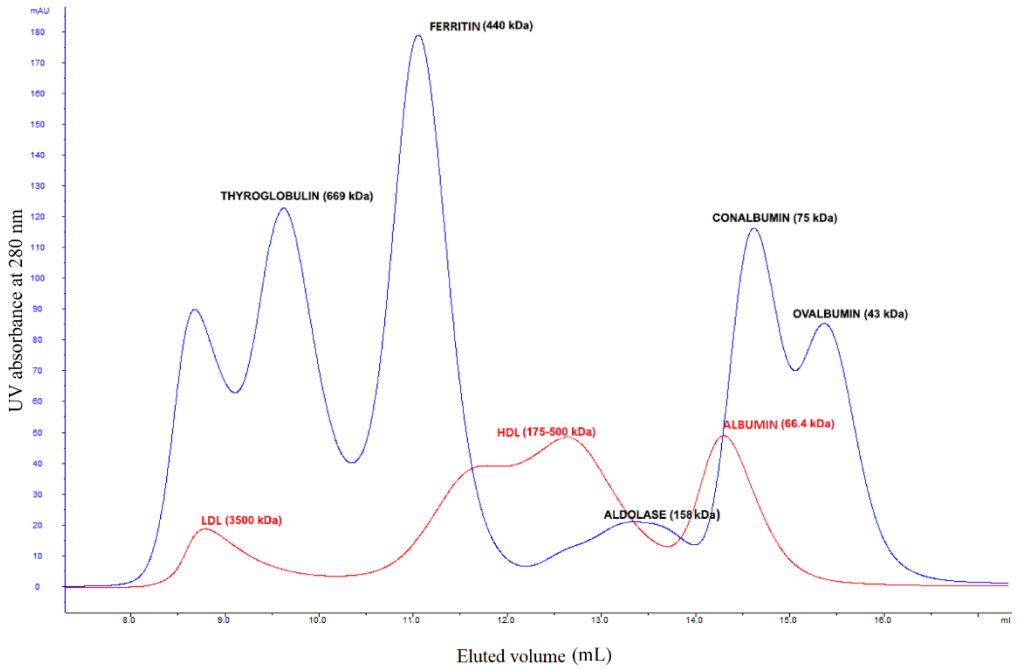

Figure S2.3. Particle size from the fractionated eluent compared with a protein molecular weight standard on a UV chromatogram (280 nm). An FPLC run using a mixture of protein molecular weight standard (thyroglobulin at 669 kDa, ferritin at 440 kDa, aldolase at 158 kDa, conalbumin at 75 kDa, and ovalbumin at 43 kDa) confirmed that the particles in the respective fractions have the correct molecular weight (LDL at 3,500 kDa, HDL at 175 – 500 kDa, and albumin at 66.4 kDa).

Some HDL-associated proteins were enriched in fractions F3-4 corresponding with the larger HDL particles (Figure 2.6 a-d), and either depleted in or completely absent from fractions F5-6, indicating that these proteins tend to associate with large HDL particles. For example, CLUS has been found to associate bimodally with large HDL and medium-to-large HDL, but not with the smallest HDL [24]. Our results also showed a bimodal distribution for CLUS (Figure 2.6a), with the most eluting in the LDL fraction F2 and the large HDL fraction F3, with an

additional though much smaller peak in the medium HDL fraction F5. HDL particles that contain CLUS have been shown to also be enriched in ApoE, ApoC-III, and PON1 [10]. We similarly found that ApoE was enriched in the larger HDL fractions. While ApoA-I is distributed in a Gaussian shape and enriched in the middle fractions, corresponding with the abundance of total HDL, ApoE is enriched in the earlier elution fractions F3-4, corresponding with the larger HDL particles (Figure b). Previous studies also showed that ApoE was associated with large HDL particles [25]. A recent study utilizing AF4 to separate 40 individual fractions in 1-2nm intervals spanning the size range of 7-30nm followed by LC-MS-based apoprotein quantification, showed that ApoE elutes across this size range, spanning HDL particles, LDL particles, as well as a distinct peak around 15nm in size (spanning the range of 13-18nm) where there are low concentrations of ApoA-I, highlighting the presence of ApoE on large HDL particles that are either depleted in or completely free of ApoA-I [13].

Along with CLUS and ApoE, PLTP was also enriched in the large HDL fraction F3 (Figure 2.6c). PLTP facilitates the transfer of phospholipids from lipid-rich lipoproteins to HDL and thereby provides material necessary to expand HDL particle size. LCAT is another enzyme that was found to be enriched in the larger HDL fractions F3 and F4 (Figure 2.6d). LCAT is involved in HDL maturation through its function of esterifying cholesterol with a fatty acid from the *sn*-2 position of a phosphatidylcholine. LCAT was absent in many proteomic analyses of HDL [25-27], which may be due to loss of LCAT using other isolation methods.

ApoC-III is the most abundant ApoC associated with lipoproteins. The main known function of ApoC-III is to inhibit the activity of lipoprotein lipase, delaying the clearance of triglyceride-rich lipoproteins (VLDL and chylomicrons) and has been associated with increased risk of hypertriglyceridemia and poor CVD outcomes [28,29]. ApoC-III-containing HDL were found

to be poorly lipidated and to be associated with smaller HDL particles with a density close to 1.21 g/ml [30]. However, a more recent report using AF4-based HDL isolation found ApoC-III to be present across the entire HDL particle size range, with the highest number of ApoC-III molecules per particle found in large HDL particles around 16nm in size [13]. Our results also indicate the presence of ApoC-III across the HDL size range (Figure 2.6e).

PON1 is an enzyme with organophosphatase, oxidase, and phospholipase-like activities that has been associated with the cardio-protective anti-oxidant function of HDL [30]. Studies have suggested that the highly hydrophobic N-terminal of PON1 anchors PON1 onto HDL [31] but that connection is weak and can be dissociated after prolonged ultracentrifugation times (as long as 48 h) [32]. PON1's presence in all of the HDL fractions F3-F6 indicates that our separation method is gentle and protective against undesirable loss of HDL-associated proteins. This advantage is important for samples that are separated for further downstream biological analysis.

ApoA-IV is an HDL-associated glycoprotein that is expressed exclusively in the small intestine in humans [33,34] in response to the ingestion of long-chain fatty acid. A recent study utilizing in situ perfusion of small intestine showed that HDL particles synthesized in the intestinal tract contain ApoA-IV, are enriched in triglyceride, and are smaller and denser than liver-derived HDL particles [35]. ApoA-IV- HDL have been found to be associated with small HDLs of size 7nm and 8.7nm [30]. In our study ApoA-IV was distributed across the HDL size range (Figure 2.6g). ApoA-II is the second most abundant apolipoprotein found associated with HDL after ApoA-I. It is also associated with the reverse cholesterol transport ability of HDL [36], however, its exact role has not been fully elucidated. Our results showed that ApoA-II was detected in similar fractions as ApoA-I (Figure 2.6h), corroborating previous observations [25,37].

Some proteins, including SAA1, A2HSG, A1AT and VDBP, were enriched in the small HDL fractions (Figure 2.6 i-l). SAA1 is an acute phase protein secreted by the liver during acute inflammatory events and during chronic inflammation in response to cytokine stimulation, and thus has been associated with HDL's role in modulating immunity [10]. During an active immune response, SAA1 concentration increases significantly and has been suggested to displace ApoA-I in HDL [38,39]. Some evidence suggests that SAA1 is associated with smaller and denser HDL (HDL-3) [38], which corresponds with our findings of SAA1 enrichment in HDL fraction F5 (Figure 2.6i). A2HSG is highly expressed in hepatocytes and is released to the plasma [40]. In our study A2HSG was found exclusively on small HDL particles in fraction F6 (Figure 2.6j), the smallest HDL coeluting with albumin. A1AT is a positive acute-phase plasma protein that is protected against oxidation through its association with HDL [6,26]. Our proteomic analysis shows that A1AT is enriched in the smallest HDL fraction F6 (Figure 2.6k).VDBP is a carrier protein for Vitamin D metabolites and has been found associated with HDL fractions in some studies [41]. Most bound vitamin D metabolites are carried by VDBP and a small fraction are carried by albumin [42]. In this study VDBP was found in the smallest HDL fractions F5-6 and in the albumin fraction F7 (Figure 2.6l). Due to differences in isolation procedures, some studies suggested that SAA1, A2ASG, and A1AT are not HDL-associated proteins, but free plasma proteins that co-isolate as contaminants with HDL [15]. However, other studies suggest otherwise, including an investigation utilizing a sequential antibody-based sandwich ELISA technique which first isolates ApoA-I-containing HDL particles followed by a second antibody-based capture of A1AT-containing HDL [10]. Using this technique, the authors showed that although most of the A1AT is indeed present as free protein in plasma, a small proportion of it does associate with a subset of HDL particles.

As shown by the differential distribution of specific proteins across the entire size range of HDL, the analysis of functions and characteristics of these different HDL subclasses may be important in gaining a better understanding of the complex biology of HDL. With the method described here, it is possible to fine-tune the size-based fractions of HDL collected. If the objective of the study is to collect the entirety of the HDL pool from a given plasma sample, it is possible to pool fractions F3-F6 corresponding to the HDL peak together. This approach maximizes total HDL amount and representativeness of the array of particles present in the plasma sample, while minimizing contamination compared to comparable methods. Alternatively, it is also possible to adjust the fractionation to collect just the middle of the HDL peak (F4 and F5), which would minimize contaminants (LDL and albumin) but would slightly reduce yield and leave out some of the heterogeneity in the HDL particles. The range of HDL fractions can be further adjusted deliberately to meet the investigators' specific needs. We showed an example of setting the fractionation cutoff at the troughs between the LDL and HDL peaks, and between the HDL and albumin peaks, and found little evidence of albumin contamination in the HDL fractions, while also minimizing loss of HDL in the albumin fraction (Figure 2.4). Whether contaminating albumin is a concern depends on the purpose of the experiment. Compositional studies, such as proteomic and glycomic analysis of HDL may not require albumin to be eliminated from the sample since albumin fragments generated from sample preparation and ionization during MS analysis can be detected and eliminated manually or by setting specific parameters in the software programs. On the other hand, for functional assays, especially if the approach is to apply a consistent dose of HDL as measured by total protein content, differential contamination levels by albumin can impact the relative proportion of HDL particles loaded per well.

Because ApoA-I was detected both by SDS-PAGE and shotgun proteomics in the albumin fraction, we set out to determine the extent of loss of HDL particles using native-condition PAGE and Western blot with anti-ApoA-I antibody. We showed that with our isolation method, using a fractionation approach where the HDL fraction is collected at the trough between the HDL and albumin peaks, there is minimal loss of HDL (estimated at 3%) into the albumin fraction (Figure 2.6).

There are some limitations and further considerations to take into account with the current method. One of the pitfalls of ultracentrifugation is the potential loss of HDL protein components, which under conditions of high salt and high g forces, may disassociate from the HDL particle [17,43]. The current method minimizes the duration of ultracentrifugation in the first step to a total of 4 hours, compared to as long as 48 hours required in other methods[5]. Although some HDL-associated protein loss may still occur, we have demonstrated that our method does not lead to the complete loss of functionally significant HDL-associated proteins, including PLTP, PON1, and LCAT. We have observed that the SEC chromatogram and isolation efficiency is affected by the lipid profile of the plasma sample. A plasma sample from an overnight fasted healthy subject is likely to produce a chromatogram similar to the pooled plasma analyzed in this study; however, a plasma sample from a hyperlipidemic or dyslipidemic subject may result in a chromatogram that is significantly different in peak shape, yield, and sometimes the ideal retention time cutoffs compared to plasma from fasted, healthy subjects. Thus, adjustment of fraction collection geared toward the sample type to be run may be necessary for sample sets including plasma samples from individuals with different types of hyperlipidemia, dyslipidemia, and/or postprandial samples. XIC data from untargeted proteomic analysis, although arguably more quantitative than spectral counts, [15] are not quantitative due to inherent differences in the

ionizatin efficiencies of different peptides, which are unrelated to their abundance. Therefore, untargeted proteomics was not used in this study to measure the absolute quantities of the 48 proteins that were detected in the fractions, but to estimate their relative abundance and relative distribution across the fractions. Finally, although our method depletes plasma proteins such as IgG from the HDL fractions comparably or more robustly compared to other published methods, there were still small amounts of IgG detectable by proteomics (Supplementary Tables 2.2 and 2.3).

6. REFERENCES

1 Rosenson, R. S. *et al.* Dysfunctional HDL and atherosclerotic cardiovascular disease. *Nat Rev Cardiol* **13**, 48-60, doi:10.1038/nrcardio.2015.124 (2016).

2 Miller, G. J. & Miller, N. E. PLASMA-HIGH-DENSITY-LIPOPROTEIN CONCENTRATION AND DEVELOPMENT OF ISCHÆMIC HEART-DISEASE. *The Lancet* **305**, 16-19, doi:10.1016/S0140-6736(75)92376-4 (1975).

3 Vaisar, T. Proteomics investigations of HDL: challenges and promise. *Curr Vasc Pharmacol* **10**, 410-421, doi:10.2174/157016112800812755 (2012).

4 Vickers, K. C., Palmisano, B. T., Shoucri, B. M., Shamburek, R. D. & Remaley, A. T. MicroRNAs are transported in plasma and delivered to recipient cells by high-density lipoproteins. *Nature cell biology* **13**, 423-433 (2011).

5 Chapman, M. J., Goldstein, S., Lagrange, D. & Laplaud, P. M. A density gradient ultracentrifugal procedure for the isolation of the major lipoprotein classes from human serum. *J Lipid Res* **22**, 339-358 (1981).

6 Gordon, S. M., Deng, J., Lu, L. J. & Davidson, W. S. Proteomic characterization of human plasma high density lipoprotein fractionated by gel filtration chromatography. *Journal of Proteome Research* **9**, 5239-5249, doi:10.1021/pr100520x (2010).

7 Collins, L. A. & Olivier, M. Quantitative comparison of lipoprotein fractions derived from human plasma and serum by liquid chromatography-tandem mass spectrometry. *Proteome Sci* **8**, 42, doi:10.1186/1477-5956-8-42 (2010).

8 Bekaert, E. D. *et al.* Isolation and partial characterization of lipoprotein A-II (LP-A-II) particles of human plasma. *Biochimica et Biophysica Acta (BBA)-Lipids and Lipid Metabolism* **1126**, 105-113 (1992).

9 Gibson, J. C. *et al.* Immunoaffinity isolation of apolipoprotein E-containing lipoproteins. *Biochimica et Biophysica Acta (BBA)-Lipids and Lipid Metabolism* **835**, 113-123 (1985).

10 Furtado Jeremy, D. *et al.* Distinct Proteomic Signatures in 16 HDL (High-Density Lipoprotein) Subspecies. *Arterioscler. Thromb. Vasc. Biol.* **38**, 2827-2842, doi:10.1161/ATVBAHA.118.311607 (2018).

11 Zschörnig, O., Machill, H., Wiegel, D., Arnhold, J. & Arnold, K. Aggregation of human plasma high density lipoproteins induced by poly (ethylene glycol). *Biomedica biochimica acta* **50**, 959-966 (1991).

12 McNamara, J. R. *et al.* Modification of the dextran-Mg2+ high-density lipoprotein cholesterol precipitation method for use with previously frozen plasma. *Clinical chemistry* **40**, 233-239 (1994).

13 Kuklenyik, Z. *et al.* Core lipid, surface lipid and apolipoprotein composition analysis of lipoprotein particles as a function of particle size in one workflow integrating asymmetric flow field-flow fractionation and liquid chromatography-tandem mass spectrometry. *PLoS One* **13**, doi:10.1371/journal.pone.0194797 (2018).

14 Michell, D. L. *et al.* Isolation of high-density lipoproteins for non-coding small RNA quantification. *JoVE (Journal of Visualized Experiments)*, e54488 (2016).

15 Holzer, M. *et al.* Refined purification strategy for reliable proteomic profiling of HDL 2/3 : Impact on proteomic complexity. *Scientific Reports* **6**, 1-10, doi:10.1038/srep38533 (2016).

16 Hafiane, A. & Genest, J. High density lipoproteins: Measurement techniques and potential biomarkers of cardiovascular risk. *BBA Clin* **3**, 175-188, doi:10.1016/j.bbacli.2015.01.005 (2015).

17 Kunitake, S. T. & Kane, J. P. Factors affecting the integrity of high density lipoproteins in the ultracentrifuge. *J Lipid Res* **23**, 936-940 (1982).

18 Khera, A. V. *et al.* Cholesterol efflux capacity, high-density lipoprotein function, and atherosclerosis. *NEW ENGL.J.MED.* **364**, 127-135 (2011).

19 Krauss, R. M. & Burke, D. J. Identification of multiple subclasses of plasma low density lipoproteins in normal humans. *J Lipid Res* **23**, 97-104 (1982).

20 Shen, M. M., Krauss, R. M., Lindgren, F. T. & Forte, T. M. Heterogeneity of serum low density lipoproteins in normal human subjects. *J Lipid Res* **22**, 236-244 (1981).

21 Berneis, K. K. & Krauss, R. M. Metabolic origins and clinical significance of LDL heterogeneity. *J Lipid Res* **43**, 1363-1379, doi:10.1194/jlr.R200004-JLR200 (2002).

22 Büyüktiryaki, S., Uzun, L., Denizli, A., Say, R. & Ersöz, A. Simultaneous depletion of albumin and immunoglobulin G by using twin affinity magnetic nanotraps. *Separation Science and Technology* **51**, 2080-2089, doi:10.1080/01496395.2016.1200086 (2016).

23 Davidson, W. S. *et al.* The effects of apolipoprotein B depletion on HDL subspecies composition and function. *J Lipid Res* **57**, 674-686, doi:10.1194/jlr.M066613 (2016).

24 Silva, H. V. d. *et al.* A 70-kDa apolipoprotein designated ApoJ is a marker for subclasses of human plasma high density lipoproteins. *Journal of Biological Chemistry* **265**, 13240-13247 (1990).

25 Davidson, W. S. *et al.* Proteomic Analysis of Defined HDL Subpopulations Reveals Particle-Specific Protein Clusters. *Arterioscler. Thromb. Vasc. Biol.* **29**, 870-876, doi:10.1161/ATVBAHA.109.186031 (2009).

26 Karlsson, H., Leanderson, P., Tagesson, C. & Lindahl, M. Lipoproteomics II: Mapping of proteins in high-density lipoprotein using two-dimensional gel electrophoresis and mass spectrometry. *PROTEOMICS* **5**, 1431-1445, doi:10.1002/pmic.200401010 (2005).

27 Heller, M. *et al.* Mass spectrometry-based analytical tools for the molecular protein characterization of human plasma lipoproteins. *PROTEOMICS* **5**, 2619-2630, doi:10.1002/pmic.200401233 (2005).

28 Yao, Z. & Wang, Y. Apolipoprotein C-III and hepatic triglyceride-rich lipoprotein production. *Current Opinion in Lipidology* **23**, 206-212, doi:10.1097/MOL.0b013e328352dc70 (2012).

29 Kohan, A. B. ApoC-III: a potent modulator of hypertriglyceridemia and cardiovascular disease. *Curr Opin Endocrinol Diabetes Obes* **22**, 119-125, doi:10.1097/MED.0000000000000136 (2015).

30 Asztalos, B. F., Tani, M. & Schaefer, E. J. Metabolic and functional relevance of HDL subspecies. *Current Opinion in Lipidology* **22**, 176-185, doi:10.1097/MOL.0b013e3283468061 (2011).

31 Mackness, B., Mackness, M. I., Arrol, S., Turkie, W. & Durrington, P. N. Effect of the molecular polymorphisms of human paraoxonase (PON1) on the rate of hydrolysis of paraoxon. *British Journal of Pharmacology* **122**, 265-268, doi:10.1038/sj.bjp.0701390 (1997).

32 Don, M. M., Masters, C. J. & Winzor, D. J. Further evidence for the concept of bovine plasma arylesterase as a lipoprotein. *Biochem J* **151**, 625-630, doi:10.1042/bj1510625 (1975).

33 Wang, F. *et al.* Apolipoprotein A-IV: a protein intimately involved in metabolism. *J Lipid Res*, jlr.R052753, doi:10.1194/jlr.R052753 (2015).

34 Peng, J. & Li, X.-p. Apolipoprotein A-IV: A potential therapeutic target for atherosclerosis. *Prostaglandins & Other Lipid Mediators* **139**, 87-92, doi:10.1016/j.prostaglandins.2018.10.004 (2018).

35 Yamaguchi, S. *et al.* Selective evaluation of high density lipoprotein from mouse small intestine by an in situ perfusion technique. *J Lipid Res* **55**, 905-918, doi:10.1194/jlr.M047761 (2014).

36 Gao, X., Yuan, S., Jayaraman, S. & Gursky, O. Role of Apolipoprotein A-II in the Structure and Remodeling of Human High-Density Lipoprotein (HDL): Protein Conformational Ensemble on HDL. *Biochemistry* **51**, 4633-4641, doi:10.1021/bi300555d (2012).

37 Gauthamadasa, K. *et al.* Speciated Human High-Density Lipoprotein Protein Proximity Profiles. *Biochemistry* **49**, 10656-10665, doi:10.1021/bi1015452 (2010).

38 Jayaraman, S., Haupt, C. & Gursky, O. Thermal transitions in serum amyloid A in solution and on the lipid: implications for structure and stability of acute-phase HDL. *J Lipid Res* **56**, 1531-1542, doi:10.1194/jlr.M059162 (2015).

39 Sato, M. *et al.* Effects of serum amyloid A on the structure and antioxidant ability of high-density lipoprotein. *Biosci Rep* **36**, doi:10.1042/BSR20160075 (2016).

40 Nawaz, S. S., Joy, S. S., Al Farsi, Y., George, T. P. & Siddiqui, K. Potential role of serum fetuin-A in relation with pro-inflammatory, chemokine and adhesion molecules in diabetic kidney disease: a case–control study. *Mol Biol Rep* **46**, 1239-1246, doi:10.1007/s11033-019-04592-2 (2019).

41 Kheniser, K. G. *et al.* Temporal Dynamics of High-Density Lipoprotein Proteome in Diet-Controlled Subjects with Type 2 Diabetes. *Biomolecules* **10**, doi:10.3390/biom10040520 (2020).

42 Altinova, A. E. *et al.* Vitamin D-binding protein and free vitamin D concentrations in acromegaly. *Endocrine* **52**, 374-379, doi:10.1007/s12020-015-0789-1 (2016).

43 Ståhlman, M. *et al.* Proteomics and lipids of lipoproteins isolated at low salt concentrations in D2O/sucrose or in KBr. *J Lipid Res* **49**, 481-490 (2008).

Chapter 3: Lutein and zeaxanthin enhance whereas oxidation, fructosylation, and low pH damage high-density lipoprotein biological functionality

Jingyuan Zheng[1], Brian V. Hong[1], Joanne K. Agus[1], Xinyu Tang[1], Nola R. Klebaner[1], Siyu Chen[2], Fei Guo[3], Danielle J. Harvey[4], Carlito B. Lebrilla[2] and Angela M. Zivkovic[1]

[1] Department of Nutrition, University of California, Davis. Davis, CA. 95616. U.S.A.

[2] Department of Chemistry, University of California, Davis. Davis, CA. 95616. U.S.A.

[3] Department of Molecular and Cellular Biology, University of California, Davis. Davis, CA. 95616. U.S.A.

[4] Department of Public Health Sciences, University of California, Davis, Davis, CA. 95616. U.S.A.

1. ABSRACT

High density lipoproteins (HDLs) are key regulators of cellular cholesterol homeostasis but are functionally altered in many chronic diseases. The factors that cause HDL functional loss in chronic disease are not fully understood. It is also unknown what roles antioxidant carotenoids play in protecting HDL against functional loss. The aim of this study was to measure how various disease-associated chemical factors including exposure to 1) Cu2+ ions, 2) HOCl, 3) H2O2, 4) sialidase, 5) glycosidase, 6) high glucose, 7) high fructose, and 8) acidic pH, and the carotenoid antioxidants 9) lutein and 10) zeaxanthin affect HDL functionality. We hypothesized that some of the modifications would have stronger impacts on HDL particle structure and function than others, and that lutein and zeaxanthin would improve HDL function. HDL samples were isolated from generally healthy human plasma and incubated with the corresponding treatments listed above. Cholesterol efflux capacity (CEC), lecithin-cholesterol acyl transferase (LCAT) activity, and paraoxonase-1 (PON1) activity were measured in order to determine changes in HDL functionality. Median HDL particle diameter was increased by acidic pH treatment, and reduced by HOCl, high glucose, high fructose, N-glycosidase, and lutein treatments. Acidic pH, oxidation, and fructosylation all reduced HDL CEC, whereas lutein, zeaxanthin, and sialidase treatment improved HDL CEC. LCAT activity was reduced by acidic pH, oxidation, high fructose treatments, and lutein. PON1 activity was reduced by sialidase, glycosidase, H2O2, and fructose, and improved by zeaxanthin and lutein treatment. These results show that exposure to oxidizing agents, high fructose, and low pH directly impairs HDL functionality related to cholesterol efflux and particle maturation, whereas deglycosylation impairs HDL antioxidant capacity. On the other hand, the antioxidants lutein and zeaxanthin

improve or preserve both HDL cholesterol efflux and antioxidant activity but have no effect on particle maturation.

2. INTRODUCTION

Although high-density lipoprotein (HDL) cholesterol (HDL-C) concentration has been found to be associated with protection from several chronic diseases such as cardiovascular disease (CVD) [1–4] and Alzheimer's disease (AD) [5,6], HDL-C itself may not be the correct target for improving risk. Some genetic variations that lead to low circulating HDL-C are not associated with higher CVD risk [7,8], and on the other hand, pharmaceutical interventions that raise HDL-C failed to prevent CVD progression [9]. Thus, the focus has turned to understanding and measuring other aspects of HDL, in particular HDL particle size distribution and functionality.

The beneficial properties of HDL particles, including cholesterol efflux capacity (CEC) [10,11], anti-inflammatory [12] and antioxidant functions [12,13], participate in several important biological processes that have been linked with disease development. However, HDL particles can be damaged and modified over time as they circulate before being cleared, especially in pathological states with high levels of oxidative stress, changes in pH, high glucose or fructose concentrations, and other chemical and enzymatic processes observed to occur in chronic disease states.

Oxidation has been found to diminish the antioxidant capacity and CEC of HDL particles, and these dysfunctional, oxidized HDL accumulate in human atheromatous plaque [14–16]. Hypochlorous acid released by myeloperoxidase in activated macrophages and the accumulation of metal ions such as Cu^{2+} can oxidize several components in HDL [17]. Glycation of apolipoprotein A-I (apoA-I), the major structural and functional apolipoprotein in HDL, with ribose or glucose resulted in the formation of advanced glycation end products (AGE) and reduction in CEC [18], though this result was not confirmed in another study [19]. HDL particles that

are both glycated and oxidized inhibit platelet aggregation and have altered lipid profiles [20]. Alterations in protein glycosylation may also be involved in loss of function of HDL particles, as demonstrated, for example, by differences in the HDL glycome of patients with vs. without coronary artery disease (CAD) [21], and differences in the immunomodulatory capacity of HDL particles with differential glycoproteomic profiles [22]. Under acidic pH, HDL particles have been found to undergo substantial structural remodeling and functional alterations [23].

Antioxidant molecules such as vitamin E are thought to protect HDL from oxidation. However, vitamin E (α- and γ-tocopherol) was found to actually promote HDL oxidation [24]. Lutein and zeaxanthin are two other antioxidant molecules that are primarily transported by HDL [25,26]. They are the predominant carotenoids of the macular pigment, which protect the retina from light-induced damage and age-related macular degeneration [27]. Several studies showed that lutein/zeaxanthin intake increased HDL-C concentrations in humans and animals [28–30]. Yet their antioxidant impact on HDL functions have not been fully resolved.

A comprehensive, head-to-head comparison of the impact of these different modifications on HDL particle structure and function has not yet been performed. In this study, we used a single pooled HDL sample to directly compare the effects of different chemical modifications on HDL structure and function. We hypothesized that some of the modifications would have stronger impacts on HDL particle structure and function than others, and that lutein and zeaxanthin would improve HDL function.

3. METERIALS AND METHODS

Sample collection and HDL isolation

Human fasting plasma was derived from blood samples from twenty men and women aged 18–45 years old at Ragle Human Nutrition Center, University of California, Davis between April 2019 and December 2019. Donors were generally healthy, did not take any medication or have any comorbidities that would affect HDL functions. The study was approved by the Institutional Review Board of UC Davis. Detailed participant description, exclusion criteria, and study design were described in a previous report [1]. A single plasma pool of 500uL from each of the 20 participants was generated and then HDL was isolated using a previously published method [2]. Briefly, 0.5 mL plasma was underlaid beneath 4.2 mL of 1.006 g/mL potassium bromide (KBr) solution (1.095% KBr w/w in deionized water) in a 4.7 mL OptiSeal Polypropylene Tube. The layered mixture was submitted to ultracentrifugation at 110,000 rpm (657,272×g) using a fixed-angle rotor (TLA-110, Beckmann-Coulter, IN, USA) in a Beckman Optima MAX-TL Ultracentrifuge for 90 minutes. The top 4.0 mL solution was removed, and the bottom 0.7 mL solution was mixed with 1.1 mL 1.340 g/mL KBr solution (59.11% KBr w/w in deionized water) to reach an adjusted density of 1.210 g/mL. The mixture was then carefully underlaid beneath 2.9 mL of 1.210 g/mL KBr solution (9.439% KBr w/w in deionized water) in a new OptiSeal Polypropylene Tube and submitted to ultracentrifugation at 110,000 rpm (657,272×g) using the same rotor and centrifuge for 30 minutes. Centrifuged solution was retrieved and the top 2 mL layer containing HDL was obtained, diluted with 2 mL 0.01M phosphate buffer saline (1XPBS, Thermo Fisher, MA, USA, Cat. No. 10010023), and filtered through a filtering unit (Amicon Ultra-4 50kDa, MilliporeSigma, MA, USA, Cat. No. UFC805024) to remove remaining KBr ions. The filtered solution was resuspended to 0.25 mL and was further separated by particle size using a Superdex 200 Increase 10/300 GL agarose-crosslinked column (GE Healthcare, USA) mounted on an HPLC system (1260 Infinity II LC

System) with a flowrate of 0.4 mL/min. HDL Fractions were collected at elution volume between 10 mL and 13.6 mL (Agilent 1260 FC-AS). The HDL isolates were pooled together to generate one consistent HDL sample from the plasma pool. Cryoprotectant (2% sucrose) was added into the collected HDL fraction, and samples were stored at -80 °C before use. Isolated HDL samples were quantified for total protein concentration using a commercially available microBCA protein assay kit (Thermo Scientific, MA, USA. Cat. No. 23235), following all manufacturer's instructions.

HDL treatments

A single pooled sample of isolated HDL was divided into 64 aliquots and treated with various reagents to simulate processes observed in chronic disease. HDL aliquots were first diluted into 0.5 mg/mL protein concentration with 1XPBS (Thermo Fisher, MA, USA, Cat. No. 10010023). Detailed treatment reagent and conditions are reported in Supplemental Table S3.1. Briefly, to simulate the effects of oxidative stress, HDL were incubated with copper (II) sulfate ($CuSO_4$, 10 μM, 18 h), hydrogen peroxide (H_2O_2, 160 μM, 2 h) or hypochlorous acid (HOCl, 160 μM, 2 h); to simulate an acidic pH environment, HDL were incubated in pH 5.5 ammonium acetate buffer (20 mM, 18 h); to induce glycation and fructosylation, processes which occur in conditions of hyperglycemia and/or high fructose intake, HDL were incubated in 50 mM glucose for 120 h, or in 100 mM fructose solution for 192 h; to simulate alterations in glycosylation, HDL were incubated with the N-glycan removal enzyme peptide:N-glycosidase F (PNGase F, 25,000 U/mL, 4 h), or the sialic acid removal enzyme α2-3, 6, 8, 9 neuraminidase A (sialidase, 2,000 U/mL, 2 h). To explore the effects of antioxidant carotenoid molecules on HDL particle structure and function, HDL samples were incubated with lutein (1 mM, 18 h) or zeaxanthin (1 mM, 18 h). All treatments were incubated at 37 °C in a water bath. Because different treatments had different

incubation time requirements, time-based control samples were generated for each incubation time (2, 4, 18, 120, or 192 hours) without any treatment. An additional HDL aliquot that received 0 hour of any treatment (i.e. frozen right after isolation) served as a master control. Each set of treatments and controls was performed in 4 replicates. In total, 64 samples were generated (10 treatment groups, 5 time-control groups, and 1 master control group, with 4 replicates for each group). The excessive reagent was removed by 5 repeats of filtration through a 50 kDa filter (Amicon Ultra-4 50kDa, MilliporeSigma, MA, USA, Cat. No. UFC805024) followed by dilution with 1XPBS (Thermo Fisher, MA, USA, Cat. No. 10010023).

To investigate the preventative potential of lutein/zeaxanthin on induced oxidation of HDL, 30μM lutein or zeaxanthin was first incubated with HDL at 4 °C for 2 h. The excessive reagent was then removed from the treated HDL solution as described above, follow by treatment with 160 μM H_2O_2 at 37 °C for 2 h to introduce oxidation. After oxidation treatment, excessive reagent was removed as described above. Control samples with HDL only, with HDL + H_2O_2, and with lutein or zeaxanthin only were prepared for background adjustments. All samples were prepared in triplicate.

Table 3.1. Detailed characteristics of experimental treatment groups. All treatments were performed at 37°C with pH 7.4 phosphate buffer saline (except for the acidic pH treatment).

Treatment name/purpose	Treatment reagent (vendor)	Concentration	Treatment time (h)	Reference
$CuSO_4$/oxidation	copper (II) sulfate ($CuSO_4$) (Cat. #: C988L31, Neta Scientific, NJ, USA)	10 μM	18	[14]
H_2O_2/oxidation	hydrogen peroxide (H_2O_2) (Cat. #: H1065, Spectrum Chemical, CA, USA)	160 μM	2	[17]
HOCl/oxidation	hypochlorous acid (HOCl)	160 μM	2	[17]

	(Cat. # S1316, Spectrum Chemical, CA, USA)			
Acidic pH/acidification	ammonium acetate buffer, pH 5.5 (Cat. #: 40100184-1, Spectrum Chemical, CA, USA)	20 mM	18	[23]
Glucose/glycation	Glucose (Cat. #: 40700008-1, Spectrum Chemical, CA, USA)	50 mM	120	[20]
Fructose/fructosylation	Fructose (Cat. #: 40600008-1, Spectrum Chemical, CA, USA)	100 mM	192	[32]
PNGase F/de-glycosylation	PNGase F (Cat. #: P0705S, New England Biolabs, MA, USA)	25,000 U/mL	4	[21]
Sialidase/de-sialylation	α2-3, 6, 8, 9 neuraminidase A (Cat. #: P722S, New England Biolabs, MA, USA)	2,000 U/mL	2	[21]
Lutein/antioxidation	Lutein (Cat. #: PHR1699, Sigma, MO, USA).	1 mM	18	[24]
Zeaxanthin/antioxidation	Zeaxanthin (Cat. #: 1733119, Sigma, MO, USA)	1 mM	18	[24]

Glycosylation modification efficacy determinations

The glycosylation modification of HDL samples was confirmed by analyzing the glycan composition from treated vs. control HDL (Supplemental Figure S3.1 and S3.2) using methods described previously [3]. Briefly, the HDL were resuspended in 100 µL of 5 mM dithiothreitol in 100 mM ammonium bicarbonate solution and denatured in a boiling water bath for 2 minutes. After the samples were cooled to room temperature, 2 µL of PNGase F was added. The samples were heated to 37°C using a microwave (CEM Corporation) at 20 watts for 10 minutes to release the glycans and incubated in a 37°C water bath overnight to hydrolyze the primary amines of the released glycans to hydroxyl groups. After the incubation, 350 µL of nanopure water was added. The samples were ultracentrifuged at 200,000 ×*g* for 45 min at 4°C and the supernatant containing the N-glycans were desalted using a porous graphitic carbon (PGC) solid phase extraction plate. The plate was conditioned using 80% (v/v) acetonitrile in water with 0.1% (v/v) trifluoroacetic acid and equilibrated using nanopure water. The samples were loaded and washed

using nanopure water before eluted using 40% (v/v) acetonitrile in water with 0.05% (v/v) trifluoroacetic acid. The eluates were vacuum-dried prior to mass spectrometry analysis.

The samples were reconstituted in nanopure water and analyzed using an Agilent 6520 Accurate-Mass Q-TOF LC/MS equipped with a PGC microfluidic chip (Agilent Technologies). The glycans were separated with a binary LC gradient using solvents (A) 3% (v/v) acetonitrile in water with 0.1% (v/v) formic acid, and (B) 90% (v/v) acetonitrile in water with 1% (v/v) formic acid at a flow rate of 300 nL/min: 0-2 min, 0-0% B; 2-20 min, 0-16% B; 20-40 min, 16%-72% B; 40-42 min, 72-100% B; 42-52 min, 100-100% B; 52-54 min, 100-0% B; 54-65 min, 0-0% B. MS spectra were scanned from m/z 600 to 2000 in positive ionization mode. The most abundant precursor ions in each MS1 spectrum were selected for fragmentation through collision-induced dissociation (CID) based on the equation $V_{collision} = 1.8 \times (m/z) \div (100\ V - 2.4\ V)$. Glycans were extracted by searching the data against an in-house human N-glycan database using the Agilent Mass Hunter Qualitative Analysis software (B.08.00) with a mass tolerance of 20 ppm. The relative abundances of glycans were compared using their chromatographic peak areas.

Lutein/zeaxanthin incorporation confirmation

The confirmation of lutein/zeaxanthin incorporation into HDL particles was conducted using methods described previously [4,5] with modifications. Lutein or zeaxanthin was incubated with 0, 50, or 500 (for lutein only) μg/mL HDL at 37 °C for 2 h and excessive lutein/zeaxanthin in the solution was removed as described in section *2.2.* The absorption of samples at 445 nm was measured on a Synergy H1 plate reader (BioTek, Winooski, VT, USA). All samples were prepared in triplicate. Lutein/zeaxanthin incorporation was confirmed (Supplemental Figure S3).

Negative-stain transmission electron microscopy and image analysis

Particle size average and distribution were assessed using negative-stain transmission electron microscopy (NS-TEM, Talos L120C, FEI, Thermo Fisher, MA, USA) and the image analysis software ImageJ [6], as described previously [2]. Briefly, 5 µL of HDL sample at 50 µg/mL protein concentration in 1XPBS was loaded on a glow-discharged carbon-coated grid (TedPella Inc., CA, USA, Cat. No. 01840-F). The sample was let sit on the grid for 1 minute for sample binding, and then removed using filter paper. Five µL of 2% uranyl formate stain was then loaded on the grid, and quickly removed using filter paper. The staining steps were repeated 4 more times. After the last stain was removed, the grid was allowed to air-dry in a dark environment before it was stored until imaging. During sample imaging, samples were viewed using a Talos L120C electron microscope at 80 kV HT and 36,000x magnification. Sample images were captured with a defocus of 1.5 – 2.0 nm and an exposure time of 300 ms with a 4096*4096 resolution. At least 10 images were captured for each sample. Particle size of samples was analyzed using the image analysis tool ImageJ with a customized IJM script. Briefly, images were adjusted for threshold using the "Default" mode. Particles with area less than 19.625 nm2 (diameter less than 5 nm) were selected using the "Particle Analysis" function and removed. Particles between 38.465 nm^2 – 706.5 nm^2 (diameter between 7 nm – 30 nm) were selected. These selected particles were then filtered with geometric parameters, excluding particles that had a circularity < 0.5, roundness < 0.5, and aspect ratio > 1.5. Particles that were not excluded were used for particle size data analysis. Median particle diameter was calculated for each experiment replicate. Particle diameter distribution was described as the percentage of particles at each 1-nm size group between 7 nm - 15 nm diameter divided by total particle number within the 7 nm – 15 nm diameter range.

CEC assay

The CEC of control and treatment samples were measured in mouse macrophages J774A.1 (ATCC, Manassas, VA, USA, Cat. No. TIB-67) using a commercially available CEC assay kit (Abcam, Cambridge, UK. Cat. No. ab19685), following manufacturer's instructions with minor adjustment as described previously [7]. Briefly, about 50,000 J774 macrophages were loaded onto each well in a 96-well microplate (Sigma, MO, USA. Cat. No. CLS3603) and incubated at 37°C, 5% CO2, 90% relative humidity for 18 hours in RPMI 1640 medium (Thermo Fisher, MA, USA. Cat. No. 11875093) with 1% penicillin/streptomycin (Thermo Fisher, MA, USA. Cat. No. 15140122), and 10% fetal bovine serum (Thermo Fisher, MA, USA. Cat. No. A3160502). After incubation, the medium was discarded and cells washed with serum-free RPMI 1640 medium for 3 times. Cells were then incubated with BODIPY-labeled cholesterol, acyl-coenzyme A: cholesterol acyltransferase inhibitor, and cyclic adenosine monophosphate provided by the assay kit at 37°C, 5% CO2, 90% relative humidity for 4 hours for cholesterol loading. After cholesterol loading, the remaining medium was removed and cells were washed with serum-free RPMI 1640 medium for 3 time, followed by the addition of 10 μg (total protein) cholesterol acceptors (HDL samples or plasma as the quality control), and positive control and negative control provided by the assay kit. The cells were then incubated at 37°C, 5% CO2, 90% relative humidity for 4 hours for cholesterol efflux. After cholesterol efflux incubation, the supernatant portion was collected and transferred to a new microplate. The remaining cell pellet was lysed with M-PER cell lysis buffer (Thermo Fisher Scientific, Waltham, MA, USA, Cat. No. 78505) for 30 minutes. The fluorescence of the supernatant and the lysed fraction were measured at 482/515 nm (excitation/emission) on a Synergy H1 plate reader (BioTek, Winooski, VT, USA). The CEC was calculated by the fluorescence value of the supernatant fraction divided by the sum of fluorescence value of the supernatant and the lysed fractions. To account for the inter-

plate variability, CEC values were normalized to the value of the plasma sample control on each plate to adjust for inter-plate variability, as previously described, resulting in a CEC index [8].

LCAT activity assay

A commercially available kit (Roar Biomedical, USA, Cat. No. mak107) was used to measure the LCAT activity of 5 µg HDL (total protein) following the manufacturer's instructions, using a Synergy H1 plate reader at excitation = 340 nm, and at emission at 390 nm or 470 nm. The ratio between fluorescence emission at 390 nm to 470 nm was calculated as a measurement of LCAT activity. The higher the ratio the higher the LCAT activity. LCAT activity values were normalized to the value of a plasma sample control on each plate to adjust for inter-plate variability, as previously described, resulting in a LCAT activity index [8].

PON1 activity assay

The Ca^{2+}-dependent PON1 activity of HDL was determined by monitoring the conversion of paraoxon to 4-nitrophenol over time at 405 nm [9,10]. HDL samples (10 µg, total protein) were placed into 96-well plate and mixed thoroughly with 200 µL buffer at pH 8 containing Tris (100mM) (Sigma, MO, USA, Cat. No. T1503), CaCl2 (2mM) (Sigma, MO, USA. Cat. No. C4901), and paraoxon (1mM) (Sigma, MO, USA. Cat. No. 36186). The absorbance of light at 405 nm wavelength was measured every 5 minutes on a plate reader. Kinetic plots were made for each group by plotting absorbance at 405 nm against measurement timepoints. The linear regions of the kinetic plots were determined and the difference between the beginning and the end absorbance value within the linear regions were found. The difference was then divided by time span between when the two absorbance points were measured and further divided by the molar extinction coefficient of the product 4-nitrophenol (17,100 $L \bullet mol^{-}$

^{1}•cm^{-1}). PON1 activity of samples was expressed as nM 4-nitrophenol/minute. PON1 activity values were normalized to the value of a plasma sample control on each plate to adjust for inter-plate variability, as previously described, resulting in a PON1 activity index [8].

Statistical analysis

Mean particle diameter, percentage of particle number at each 1-nm size group, CEC index, LCAT 390/470 ratio, and PON1 activity for each replicate were tested for outliers using the Grubb's Test for Outliers with a $\alpha = 0.05$. Mean particle diameter, percentage of particle number at each size group, CEC index, LCAT 390/470 ratio, and PON1 activity for each treatment were compared to the control group that corresponded to their treatment times using two-sample t-test with significance value reported as $p < 0.05$, assuming equal variance. For multi-group comparisons, differences between groups were tested with one-way ANOVA, and pair-wise comparisons were conducted using *post hoc* Tukey's HSD. Statistically significant findings are indicated as * $p < 0.05$, ** $p < 0.01$, *** $p < 0.001$, and **** $p < 0.0001$. The normality of the outcome variables was inspected using the Shapiro–Wilks test. The equal variance between groups was examined using Levene's test.

4. RESULTS

HDL particle size and distribution

Median HDL particle size and particle size distribution were assessed to determine structural changes in response to the treatments. The HDL diameter results in the time controls were generally similar (Figure 3.1A), except for C18h (10.7 nm ± 0.0818 nm), which was significantly smaller than that of C4h (11.4 nm ± 0.0483 nm), C120h (11.4 nm ± 0.101 nm), and C192h (11.5 nm ± 0.124 nm). Figure 1B shows that HDL samples that were incubated with

HOCl (9.12 nm ± 0.11 nm vs. 11.39 nm ± 0.28 nm, -19.93 %, $p < 0.005$), glucose (10.02 nm ± 0.35 nm vs. 11.41nm ± 0.10 nm, -12.13 %, $p < 0.005$), fructose (10.07 nm ± 0.35 nm vs. 10.73 nm ± 0.08 nm, -12.01 %, $p < 0.05$), PNGase F (10.44 nm ± 0.06 nm vs. 11.37 nm ± 0.05 nm, -8.13 %, $p < 0.001$), and lutein (10.03 nm ± 0.17 nm vs. 10.73 nm ± 0.08 nm, -6.48 %, $p < 0.01$) had significantly smaller median particle diameter than their respective control groups. HDL treated with acidic pH of 5.5 was the only treatment group that had a significantly larger (12.46 nm ± 0.55 nm vs. 10.73 ± 0.08 nm, +16.23 %, $p < 0.01$) median diameter than control. HDL treated with H_2O_2, zeaxanthin, $CuSO_4$, and sialidase did not have significantly different particle size from their control groups (Figure 3.1B).

Because HDL particles are structurally heterogeneous and have a continuous size range, the size distribution of HDL in different treatment groups were further characterized and compared to their control groups (Figure 3.1C). The population of particles within the diameter range of 7 nm – 15 nm were divided by 1-nm increment into 8 subclasses (7 nm – 8 nm, 8 nm – 9 nm, etc.). For each treatment group, the abundance of particles within each subclass was compared to the same subclass in the corresponding control group. Fructose, glucose, H2O2, HOCl, lutein, PNGase F, and zeaxanthin treatment resulted in a significant increase in small particles compared to their corresponding control groups (Figure 3.1C). For the glucose and PNGase F groups particularly, a shift in particle size distribution from larger to smaller particles was observed. In contrast, $CuSO_4$, acidic pH, and sialidase shifted particle size distribution from smaller to larger particles (Figure 3.1C).

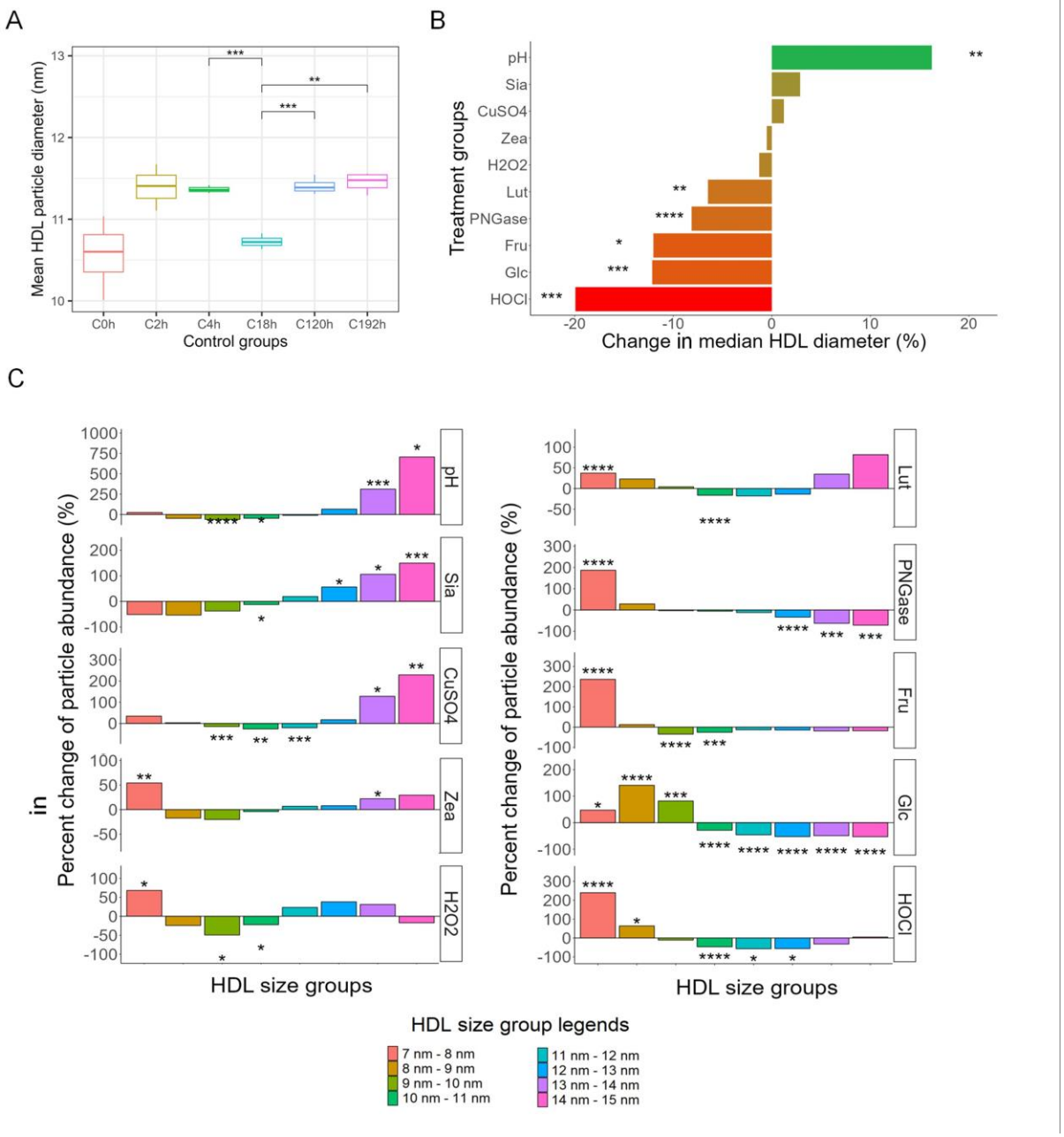

Figure 3.1. Diameter changes of HDL in different treatment groups compared to corresponding time-controls. (A) Comparisons of HDL diameter in different time control groups. (B) Change in median HDL particle diameter measured on transmission electron microscope images of HDL samples. (C) Analysis of HDL 1-nm size group abundance change in response to treatments. Subfraction abundance was calculated as 100% × (abundance of HDL

subfraction in the treatment group) ÷ (abundance of HDL subfraction in the corresponding time-control group). Statistical significance is shown as *($p<0.05$), **($p<0.01$), ***($p<0.005$), ****($p<0.001$). Treatments legend: **HOCl** = hypochlorous acid; **Glc** = glucose; **Fru** = fructose; **PNGase** = PNGase F; **Lut** = lutein; **H2O2** = hydrogen peroxide; **Zea** = zeaxanthin; **CuSO4** = copper (II) sulfate; **Sia** = α-2, 3, 6, 8-neuraminidase; **pH** = pH 5.5.

HDL CEC, LCAT activity and PON1 activity

The control-normalized mean HDL CEC index among treatment groups was significantly different (ANOVA $p<0.001$) after correction to their corresponding time controls. Pairwise comparison showed that the pH treatment group had the lowest HDL CEC value (0.193 ± 0.163, significantly lower than Glc, Lut, PNGase, Sia, and Zea groups), followed by the HOCl group (0.217 ± 0.0115, significantly lower than CuSO4, Fru, Lut, Sia,and Zea groups), the CuSO4 group (0.443 ± 0.0115, significantly lower than Fru, Lut, Sia, and Zea groups), the H2O2 group (0.750 ± 0.0700, significantly lower than Lut, Sia, and Zea groups), and the Fru group (0.797 ± 0.0114, significantly lower than Glc and Sia groups). The Glc group (0.953 ± 0.0981) was significantly higher than the pH group. The PNGase (1.25 ± 0.232), Zea (1.29 ± 0.0586), Sia (1.34± 0.0537), and Lut (1.35 ± 0.135) groups had the highest HDL CEC values (Supplemental Table S3.1). We further compared the percentage of change in CEC in the treatment groups compared to their time-controls (Figure 3.2A). Low pH (0.11 ± 0.095 vs. 0.58 ± 0.04, -81 %, $p < 0.001$), HOCl (0.13 ± 0.01 vs. 0.61 ± 0.04, -78%, $p < 0.001$), $CuSO_4$ (0.26 ± 0.01 vs. 0.58 ± 0.04, -56%, $p < 0.001$), H_2O_2 (0.46 ± 0.044 vs. 0.61 ± 0.043, -25%, $p < 0.01$), and fructose (0.44 ± 0.0058 vs. 0.58 ± 0.041, -21%, $p < 0.01$) treatment resulted in significantly lower CEC (Figure 3.2A). In contrast, zeaxanthin (0.75 ± 0.032 vs. 0.58 ± 0.043, +29%, $p < 0.005$), sialidase (0.82 ±

0.03 vs. 0.61 ± 0.04, +34%, $p < 0.001$), and lutein (0.79 ± 0.078 vs. 0.58 ± 0.043, +35%, $p < 0.01$) treatment resulted in significantly higher CEC than their control groups (Figure 3.2A).

Control- normalized LCAT activity was not significantly different among treatment groups (ANOVA $p = 0.08$), and none of the treatment groups was significantly different from one another after adjustment for multiple pairwise comparisons (Supplemental Table S3.1). Nevertheless, several treatments significantly changed HDL LCAT activity compared to their time-controls: low pH (0.88 ± 0.070 vs. 1.0 ± 0.023, -12%, $p < 0.05$), H_2O_2 (0.91 ± 0.024 vs. 1.0 ± 0.024, -11%, $p < 0.005$), HOCl (0.93 ± 0.016 vs. 1.0 ± 0.024, -8.8%, $p < 0.001$), fructose (0.93 ± 0.0056 vs. 0.97 ± 0.015, -4.3%, $p < 0.05$), and lutein treatment (0.96 ± 0.0035 vs. 1.0 ± 0.023, -4.2%, $p < 0.05$) reduced LCAT activity compared to their controls, whereas none of the other treatments altered LCAT activity (Figure 3.2B).

Control-adjusted PON1 activity was significantly different among treatment groups (ANOVA < 0.001). The Fru group had the lowest normalized PON1 activity value (0.060 ± 0.14) and was significantly lower than the Lut and Zea groups, followed by the Sia group (0.31 ± 0.072, significantly lower than the CuSO4, Lut, and Zea groups), the H2O2 group (0.46 ± 0.12, significantly lower than Lut and Zea groups), the PNGase group (0.58 ± 0.038, significantly lower than Lut and Zea groups), the Glc group (0.61 ± 0.071, significantly lower than Lut and Zea groups), the pH group (0.65 ± 0.12, significantly lower than Lut and Zea groups), the CuSO4 group (0.76 ± 0.082, significantly lower than Sia, Lut and Zea groups), and the HOCl group (0.88 ± 0.33, significantly lower than Lut and Zea groups). The Zea (3.1 ± 0.40) and Lut (4.1 ± 0.31) groups had the highest normalized PON1 activity values among the treatment groups (Supplemental Table S3.1). Paraoxon hydrolysis activity (i.e. PON1 activity) of HDL treated with fructose (1.2 nM/minute vs. 1.9 nM/minute, -94%, $p < 0.005$), sialidase (1.6 nM/minute vs.

5.1 nM/minute, -69%, $p < 0.001$), H_2O_2 (2.4 nM/minute vs. 5.1 nM/minute, -54%, $p < 0.005$), and PNGase F (3.0 nM/minute vs. 5.3 nM/minute, -42%, $p < 0.001$) was significantly reduced compared to the corresponding time-control groups (Figure 3.2C). Samples treated with zeaxanthin (9.9 nM/minute vs. 3.5 nM/minute, +182%, $p < 0.001$) and lutein (13 nM/minute vs. 3.5 nM/minute, +279%, $p < 0.001$), on the other hand, showed a significant and substantial increase in PON1 activity (Figure 3.2C). Variation in functional assay measurements of the control groups is shown in Supplemental Figure S3.4.

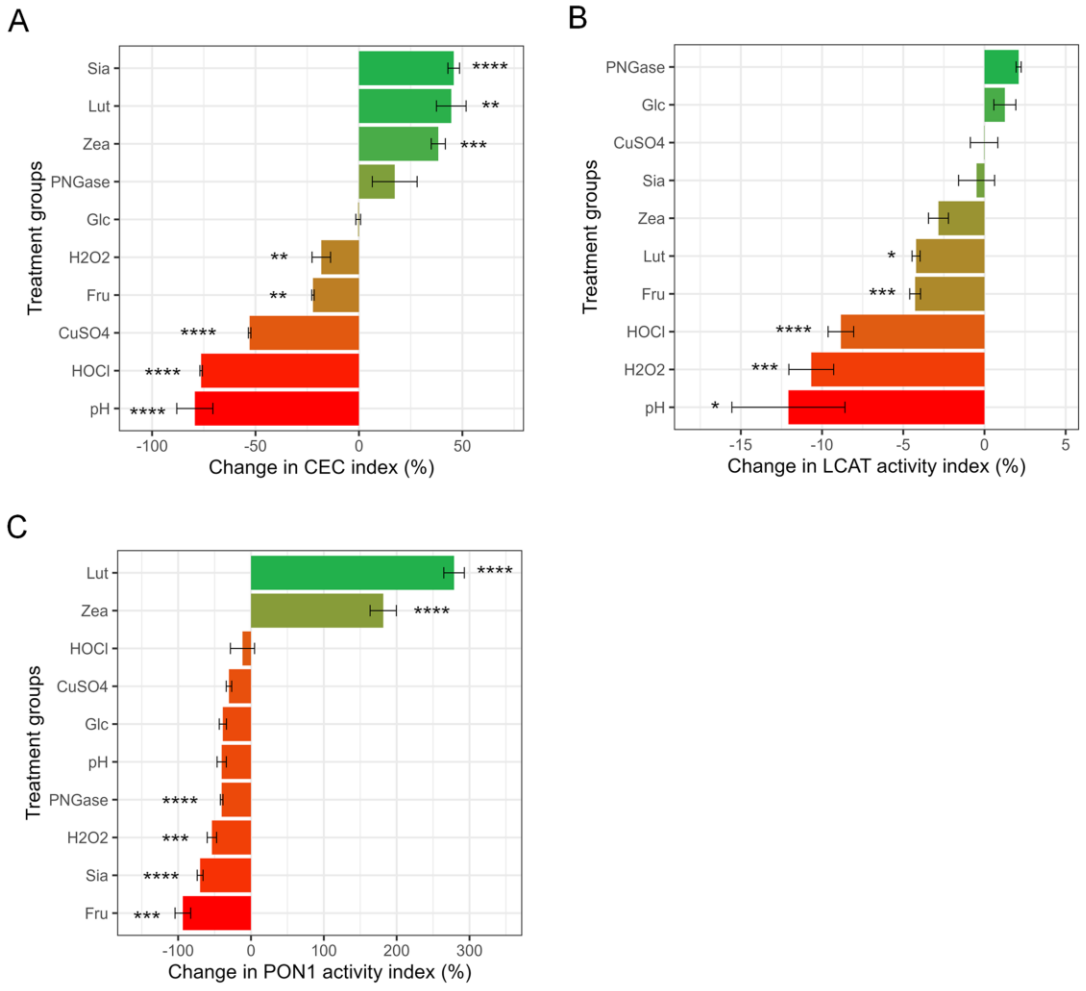

Figure 3.2. Percentage change in HDL functional measurements. (A) Change in CEC. CEC was measured using a commercially available kit in J774A.1 mouse macrophage cells. Change in

CEC was calculated as 100% × (CEC of treatment groups - CEC of corresponding time-control group)) ÷ (CEC of corresponding time-control group). (B) Percent LCAT activity change. LCAT activity was measured as the sample fluorescent emission ratio at λ = 390 nm over λ = 470 nm using commercially available kit at excitation λ = 340 nm. Change in LCAT activity was calculated as 100% × (LCAT activity of treatment groups - LCAT activity of corresponding time-control group) ÷ (LCAT activity of corresponding time-control group). (C) Percent PON1 activity change. PON1 enzyme activity was reported as the nM of paraoxon converted to 4-nitrophenol per minute. Change in PON1 activity was calculated as 100% × (PON1 activity of treatment groups - PON1 activity of corresponding time-control group)) ÷ (PON1 activity of corresponding time-control group). Statistical significance is shown as *($p<0.05$), **($p<0.01$), ***($p<0.005$), ****($p<0.001$). Treatments legend: **HOCl** = hypochlorous acid; **Glc** = glucose; **Fru** = fructose; **PNGase** = PNGase F; **Lut** = lutein; **H2O2** = hydrogen peroxide; **Zea** = zeaxanthin; **CuSO4** = copper (II) sulfate; **Sia** = α-2, 3, 6, 8-neuraminidase; **pH** = pH 5.5.

HDL CEC, LCAT activity and PON1 activity after lutein/zeaxanthin pre-incubation followed by oxidation treatment

To further explore whether lutein and zeaxanthin can prevent HDL from oxidation, we performed additional experiments to oxidize HDL samples after lutein/zeaxanthin pre-incubation. Figure 3.3 shows the CEC, LCAT activity, and PON1 activity of HDL samples after H_2O_2-induced oxidation with or without lutein/zeaxanthin pre-incubation. H_2O_2 treatment reduced CEC, LCAT, and PON1 activity of HDL (Figure 3.3A, B, C). Pre-incubating HDL with 30 μM lutein for 2 h (0.81 ± 0.026, Figure 3A, yellow bar) attenuated the effect of H_2O_2 (0.67 ± 0.034, Figure 3A, gray bar) on CEC reduction, but the attenuation of PON1 activity loss did not reach statistical

significance (Figure 3.3C). Neither lutein nor zeaxanthin pre-incubation had an effect on LCAT activity loss (Figure 3.3B). Pre-incubating HDL with 30 μM zeaxanthin for 2 h did not have a significant preventative effect on HDL CEC or PON1 activity loss (Figure 3.3A, C red vs. dark gray column).

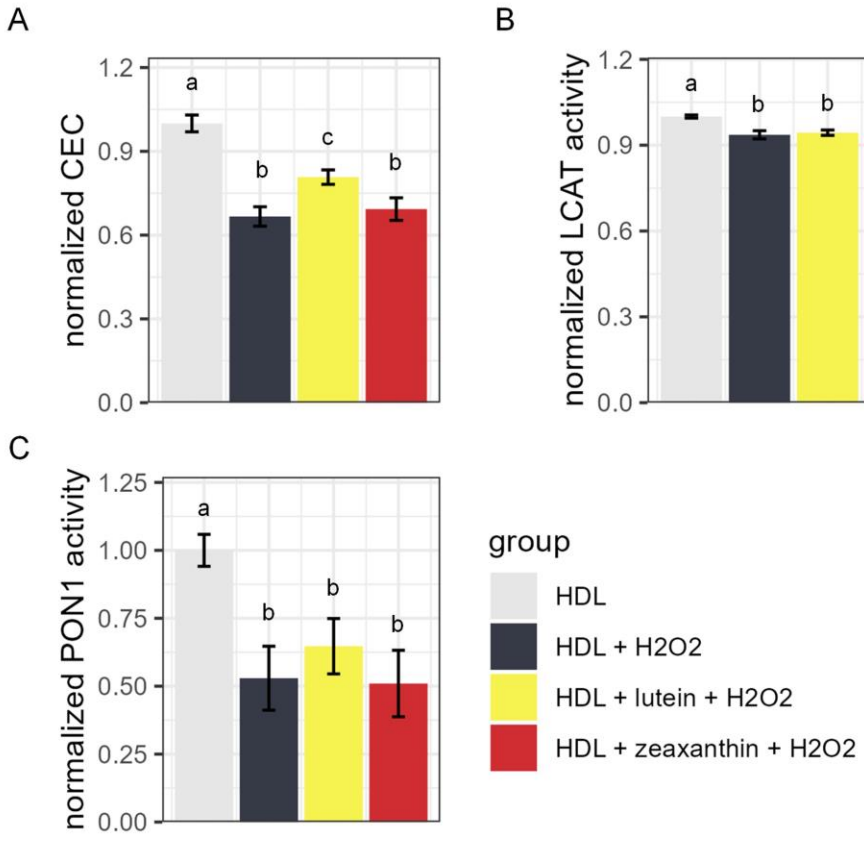

Figure 3.3. Functional measurement of HDL with and without carotenoid pre-treatment. A) Normalized cholesterol efflux capacity (CEC), B) normalized lecithin-cholesterol acyltransferase (LCAT) activity, and C) normalized paraoxonase-1 (PON1) activity of HDL particles without H2O2 oxidant treatment (light grey), with H2O2 treatment but without carotenoid pre-incubation (dark grey), with lutein pre-treatment followed by H2O2 treatment (yellow), and with zeaxanthin

pre-treatment followed by H2O2 treatment (red). For all groups with the same letter above the bars, the difference between the means was not statistically significant.

5. DISCUSSIONS

The aim of this study was to determine the effects of multiple chemical modifications often observed in pathological processes on HDL particle size distribution and functional properties, and to determine the effects of the carotenoids lutein and zeaxanthin on the same parameters. The antioxidant carotenoids lutein and zeaxanthin consistently improved HDL CEC and PON1 activity, and lutein treatment slightly reduced LCAT activity. Lutein and zeaxanthin are transported primarily by HDL in the body [26] and exert well-characterized functions in the eye [38]. High lutein supplementation in animals has been found to reduce oxidized low-density lipoprotein (LDL) [39]. Moderate lutein supplementation in the form of egg yolk or milk in human trials has been shown to increase plasma lutein level without increasing HDL-C or LDL-cholesterol [40]. On the other hand, oxidants, including HOCl, H_2O_2, and $CuSO_4$ reduced HDL function. The CEC results are in agreement with previous findings, where oxidizing agents were shown to impair ATP-binding cassette transporter A1-mediated cholesterol transport [17] as well as other CEC-related components [41]. Treating human subjects with γ-radiolysis water containing hydroxyl radical and peroxide anions significantly reduced PON1 activity and the sulfhydryl groups on PON1 [42]. Besides lutein, LCAT activity was reduced by low pH, H_2O_2, HOCl, and high-concentration fructose incubation. The mechanism of such reductions is not clear. One possibility could be removal of LCAT from its complex with HDL through these treatments. These results suggest that the CEC, LCAT, and PON1 activity of HDL are sensitive to oxidative stress.

The most surprising result was that high glucose was the only treatment that did not affect any of the HDL functions; whereas high fructose treatment consistently reduced all three functional assays of HDL. It is possible that functional differences could be observed with longer incubation times [43]. However, longer incubation times introduce HDL degradation, which may confound the effects of glycation. High blood glucose and fructose levels are commonly found in patients with T2DM or in people who habitually consume sugary food or beverages [44,45]. Most of the previous studies on the adverse effects of high fructose diet revolve around its interaction with body cells and the lipogenic effect of fructose [46,47]. These results indicate that high fructose may be more destructive to HDL function than a high glucose environment.

Low pH treatment also had a strong negative effect on HDL function, especially CEC and LCAT activity. Previous studies with similar experimental design found that low pH increased the CEC of HDL [23]. However, instead of neutralizing pH by adding base, we filtered out the low pH solution using a filtering unit with 50 kDa pore size and reconstituted HDL with PBS. This procedure can remove free apoA-I, a 28 kDa protein that contributes significantly to CEC, from the sample. This may be what caused the differences between our results and previous findings. The LCAT and PON1 activity of low pH-treated HDL were also reduced compared to their respective control, though the difference in PON1 activity did not quite reach statistical significance ($p = 0.07$). A simple explanation may be that at low pH the proteins unfolded and some of the free apoA-I, LCAT, and PON1 from the HDL detached from the particle [23]. Both LCAT (~47 kDa) and PON1 (~43 kDa) are smaller than the pore size of our filtering unit and thus likely did not remain in the HDL sample as free proteins.

The effects of glycosylation modification, sialidase and PNGase F treatments, on HDL functions were more unpredictable. While sialidase treatment increased CEC, it reduced PON1

activity. PNGase F treatment also decreased PON1 activity, but it appeared to increase CEC. Terminal sialic acid residues have an array of important roles including modification of the microenvironment, masking of the underlying glycans, and facilitating specific recognition and interactions, for example via lectin receptors [48]. It is currently unknown what aspects of HDL-associated sialylation could have led to the observed increase in CEC. On the other hand, both sialidase and PNGase F treatment reduced HDL PON1 activity. PON1 is a glycoprotein [49] so it is possible that glycosylation removal reduced its activity. Another possibility is that sialic acids themselves may be naturally modified into uncharged lactones between the C-1 carboxyl group and hydroxyl groups from adjacent sugars [48], which then may be an additional substrate for PON1, and thus the control group would contain more sialic acid lactone than the sialic acid-free sialidase treatment group, resulting in lower apparent PON1 activity in the sialidase-treated group. Interestingly, although LCAT is also a glycosylated protein [50], LCAT activity was not significantly affected by either sialidase or PNGase F treatment.

The structural changes of HDL after each treatment were characterized by their change in particle diameter and subclass abundance. HOCl treatment resulted in smaller median HDL particle diameter in this study. Several key structural components of HDL, including apoA-I [51], apoA-II [51] and apoE [52] undergo structural changes after oxidation. It is less clear why H_2O_2 treatments, also a potent oxidizing agent, did not result in reduced median HDL particle diameter. One possible explanation is that HOCl is a more powerful oxidant than H_2O_2 [17]. In this study since the amount of HOCl and H_2O_2 were in equal molar ratio, the oxidizing power of H_2O_2 may not be strong enough to induce a significant change in median HDL size that is comparable to the effects of HOCl. In fact, the changes in HDL subgroups in the H_2O_2 treated samples were partially comparable to that of the HOCl groups – both treatments increased the

abundance of the smallest 7 nm - 8 nm particles, and reduced the 10 nm – 11 nm medium-size HDL particles, though both magnitude and statistical significance were lower for the H_2O_2 treatment group. Low pH substantially increased median HDL particle size, with the largest HDL (13 nm – 15 nm) specifically being increased in abundance compared to the control (Figure 3.1). On the other hand, Cu^{2+} treatment changed HDL subfraction distribution the same way as low pH, but the overall median HDL size was not different compared to the control group. Such differences were expected. Cu^{2+}-treated HDL has been shown to be slightly larger by HPLC analysis, but not obvious enough to be seen under TEM [53], and also had reduced CEC [14,53] which agrees with our observations. For acidic pH environment, previous studies with a similar design have shown that compared to the elution profile of non-treated HDL3 particles, which eluted as one peak, HDL incubated at pH 5.5 buffer showed two separate peaks, one larger and the other smaller. The smaller peak was identified as free apoA-I protein [23].

We also observed that the majority of treatments that reduced LCAT activity (lutein, high fructose, HOCl, H_2O_2, and acidic pH) also reduce the median HDL particle diameter. This is in agreement with historical reports that LCAT is enriched in large HDL in proteomic studies [32]. This observation suggests that either there is a structural preference of the LCAT protein for large HDL particles, or that removing LCAT from HDL through external factors results in reduced HDL maturation.

Lutein incubation reduced median HDL diameter, and more specifically increased the abundance of the smallest HDL subfraction while reducing the medium-size HDL subfraction. Zeaxanthin treatment achieved similar subfraction changes, but the overall median HDL diameter was unchanged. The incorporation of lipophilic molecules may disturb the structure of HDL and potentially introduce cleavage of a large HDL into more than one HDL particles or

fragments [54]. We further showed that pre-incubating HDL with 30 μM lutein (physiological level) attenuated the negative effects of H_2O_2-induced oxidation on CEC by 21% (Figure 3.3A). On the other hand, zeaxanthin pre-incubation did not protect HDL particle function from H_2O_2-induced oxidation. It is important to note that lutein and zeaxanthin, among other carotenoids, are extensively modified, undergoing isomerization and other modifications during the process of digestion and absorption, and also have multiple interactions with gut microbes [55], which could all have important implications for the effects of these molecules in vivo.

Glucose and fructose treatments both reduced median HDL diameter. There is limited information on HDL particle size after glucose or fructose treatments. Patients with type 2 diabetes have been shown to have decreased average HDL diameter, specifically, a shift from medium and large HDL particles to small HDL particles [56–58]. However, this shift in HDL particle size distribution in type 2 diabetes may be related to metabolic effects associated with the well-known mechanism of cholesterol ester transfer protein (CETP)-mediated HDL metabolism by hepatic lipase [59].

PNGase F and sialidase treatments modify the glycan structure of HDL-associated proteins. PNGase F treatment reduced median HDL diameter. N-glycans alter the conformational preferences of proteins to a higher probability of more compact and stable conformations [60,61]. However, the impacts of glycosylation on protein conformation and association with HDL particles, and the downstream effects on HDL particle structure have not been characterized. It is possible that the lipid-protein complex was loosened in response to N-glycan removal, and a larger HDL may thus disintegrate into more than one smaller HDLs. Our results support this hypothesis since the largest HDLs (12 nm – 15 nm) were significantly decreased while the smallest HDLs (7 nm – 8 nm) were significantly increased in abundance (Figure 3.2) after

PNGase F treatment. In contrast, sialidase treatment did not significantly alter median HDL size. However, sialidase treatment significantly increased the abundance of the largest HDL subfractions (12 nm – 15 nm) while the smaller subfractions were slightly but not significantly reduced. Sialidase specifically removes terminal sialic acid residues from glycan chains. Without sialic acids, proteins of HDL particles that are known to be sialylated (e.g. apoA-II, apoCs, apoD, apoE, apoJ, and apoM) [62] may adopt different conformations, affecting the structure and function of HDL particles.

6. SUPPLEMENTAL INFORMATION

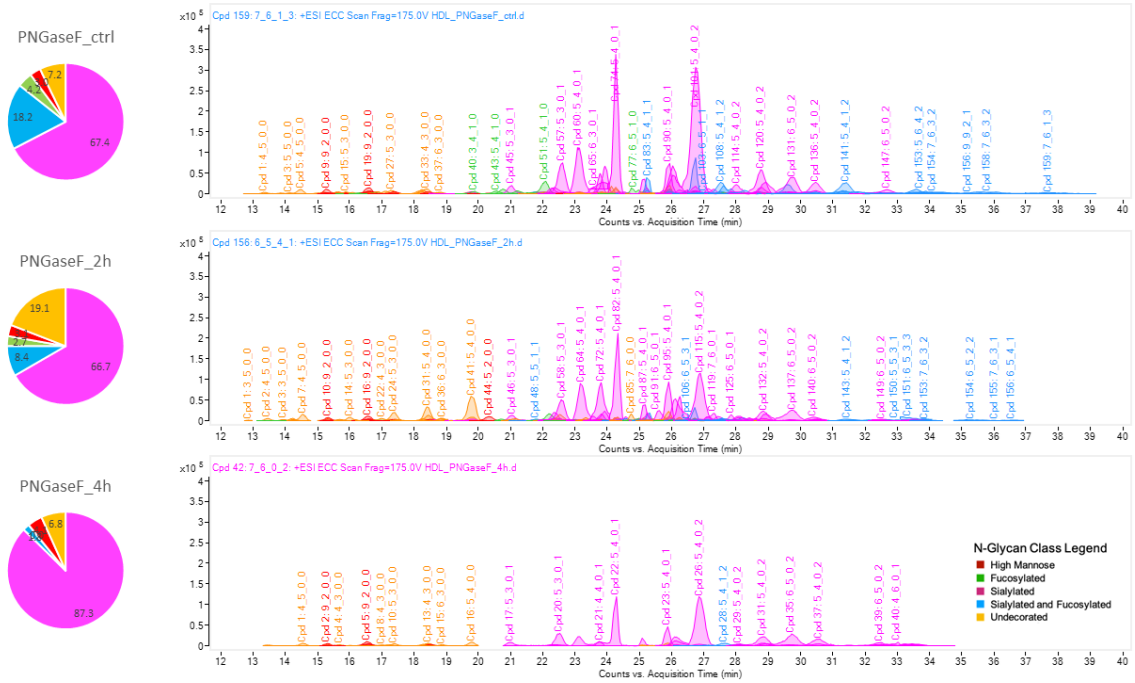

Figure S3.1. Glycoprofile of HDL samples incubated with PNGase F for different amounts of time. HDL isolates were treated with PNGase F (25,000 U/mL) for 0, 2, or 4 hours. The extracted compound chromatograms show the released N-glycans annotated with glycan compositions (extracted compound number followed by the numbers of hexose_N-acetylhexosamine_fucose_sialic acid). The peaks are color coded to show N-glycan subtypes according to the legend: red, high mannose; green, fucosylated; pink, sialylated; blue, fucosylated and sialylated; orange, undecorated. The pie charts represent the relative abundances of each N-glycan subtype. The chromatograms show a depletion of all types of glycans after PNGase F treatment for 2h and especially 4h.

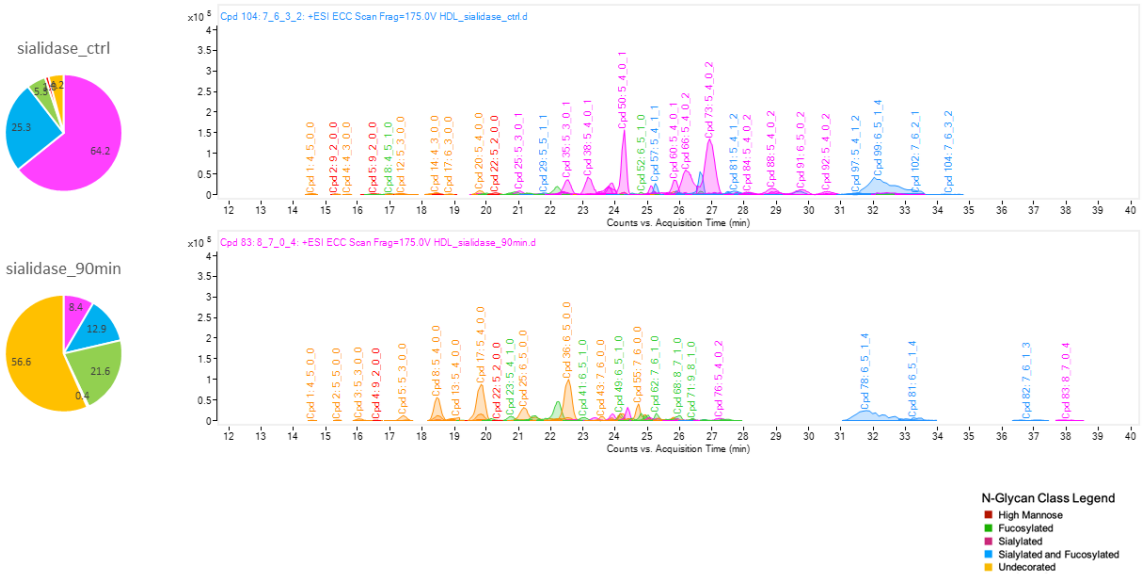

Figure S3.2. Glycoprofile of HDL samples incubated with sialidase (α2-3, 6, 8, 9 neuraminidase A) for different amounts of time. HDL isolates were treated with sialidase (2,000 U/mL) for 0 or 90 minutes. The extracted compound chromatograms show the released N-glycans annotated with glycan compositions (extracted compound number followed by the numbers of hexose_N-acetylhexosamine_fucose_sialic acid). The peaks are color coded to show N-glycan subtypes according to the legend: red, high mannose; green, fucosylated; pink, sialylated; blue, fucosylated and sialylated; orange, undecorated. The pie charts represent the relative abundances of each N-glycan subtype. The chromatograms show a depletion of sialylated (pink) as well as sialylated and focyslated (blue) glycans after neuraminidase treatment for 90 min.

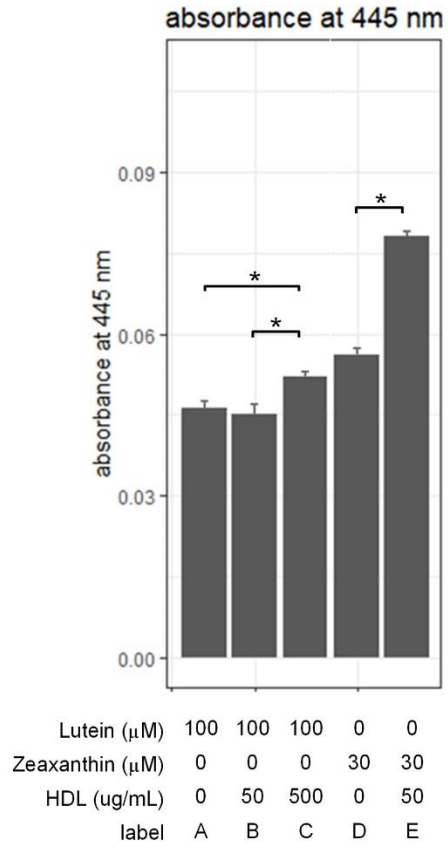

Figure S3. Comparisons of solution absorbance at 445 nm. Solution with 100 μM lutein (A, B, C) incubated with 0 (A), 50 (B), and 500 (C) μg/mL HDL and solution with 30 μM zeaxanthin (D, E) incubated with 0 (D) or 50 (E) μg/mL HDL were measured for absorbance at 445 nm wavelength after solvent replacement to evaluate retainment of carotenoid molecules as a reflection of carotenoid incorporation in HDLs.

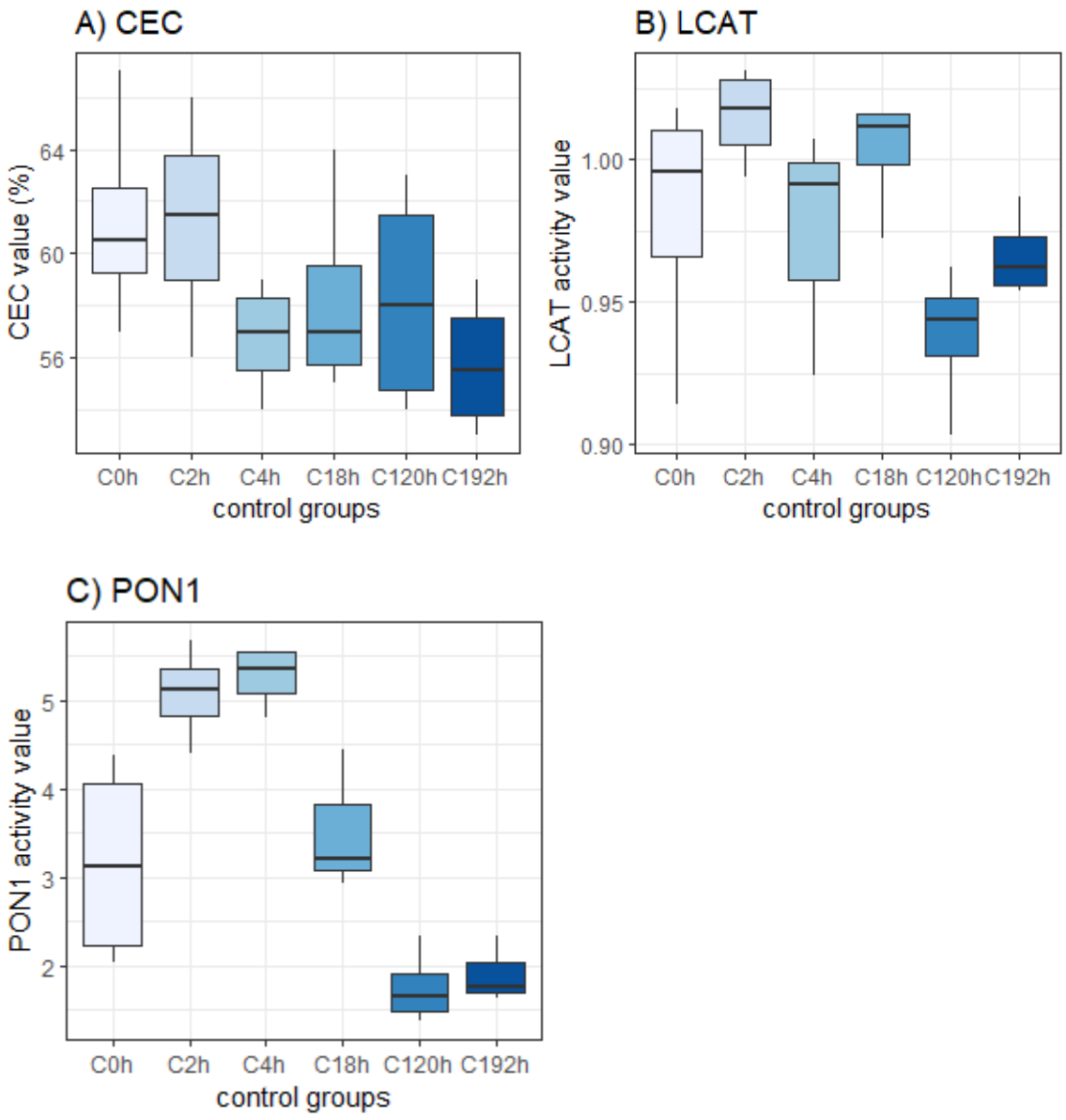

Figure S3.4. Comparisons of HDL functional assay values of Control groups. The A) cholesterol efflux capacity (CEC), B) lecithin-cholesterol acyltransferase (LCAT) activity, and C) paraoxonase-1 (PON1) activity of the control group (C0h) and various time-control groups (C2h, C4h, C18h, C120h, and C192h).

Table S3.1. Differences in time control-normalized CEC, LCAT, and PON1 activity among treatment groups. Shown are the means and standard deviations (SD) for cholesterol efflux capacity (CEC), lecithin cholesterol acyltransferase (LCAT) activity, and paraoxonase 1 (PON1) activity for each treatment group normalized to corresponding time-control. ANOVA analysis was performed to determine whether there were statistically significant differences among the

treatment groups. The p-values for the ANOVA analyses were: $p < 0.001$ for CEC, $p = 0.002$ for LCAT, and $p < 0.001$ for PON1. Pairwise comparisons between treatment groups were performed using a t-test with the Benjamini–Hochberg adjustment for CEC, LCAT, and PON1. Treatment groups that were not statistically significantly different were labeled with the same letter in the comparisons column of each biological assay. Treatments legends: **CuSO4** = copper (II) sulfate; **Fru** = fructose; **Glc** = glucose; **H2O2** = hydrogen peroxide; **HOCl** = hypochlorous acid; **Lut** = lutein; **pH** = pH 5.5; **PNGase** = PNGase F; **Sia** = α-2, 3, 6, 8-neuraminidase; **Zea** = zeaxanthin.

Variables	**CEC**			**LCAT**			**PON1**		
	mean	**s.d.**	**comparisons**	**mean**	**s.d.**	**comparisons**	**mean**	**s.d.**	**comparisons**
CuSO4	0.443	0.012	a	0.985	0.0071	ns	0.758	0.0818	a
Fru	0.797	0.012	b	0.943	0.0289	ns	0.0600	0.141	ab
Glc	0.953	0.098	abc	1.02	0.0115	ns	0.610	0.0707	abc
H2O2	0.750	0.0700	abcd	0.923	0.0551	ns	0.463	0.115	abcd
HOCl	0.217	0.0115	cde	0.910	0.0200	ns	0.883	0.328	abce
Lut	1.35	0.135	bcf	0.973	0.0231	ns	4.14	0.309	f
pH	0.193	0.163	abde	0.880	0.0698	ns	0.650	0.121	abcdeg
PNGase	1.25	0.232	abcdefg	0.997	0.0231	ns	0.575	0.0379	abcdefgh
Sia	1.34	0.0537	cfgh	0.993	0.0153	ns	0.313	0.0723	bcdefgh
Zea	1.29	0.0585	bcfgh	0.987	0.0306	ns	3.08	0.395	f

7. REFERENCES

1. Gofman, J. W., Young, W. & Tandy, R. Ischemic heart disease, atherosclerosis, and longevity. *Circulation* **34**, 679–697 (1966).

2. Gordon, T., Castelli, W. P., Hjortland, M. C., Kannel, W. B. & Dawber, T. R. High density lipoprotein as a protective factor against coronary heart disease: the Framingham Study. *The American journal of medicine* **62**, 707–714 (1977).

3. Miller, N. E., Thelle, D., Førde, O. & Mjøs, O. THE TROMSØHEART-STUDY: HIGH-DENSITY LIPOPROTEIN AND CORONARY HEART-DISEASE: A PROSPECTIVE CASE-CONTROL STUDY. *The Lancet* **309**, 965–968 (1977).

4. Voight, B. F. *et al.* Plasma HDL cholesterol and risk of myocardial infarction: a mendelian randomisation study. *The Lancet* **380**, 572–580 (2012).

5. Pedrini, S., Chatterjee, P., Hone, E. & Martins, R. N. High-density lipoprotein-related cholesterol metabolism in Alzheimer's disease. *Journal of Neurochemistry* (2020).

6. Reitz, C. *et al.* Association of higher levels of high-density lipoprotein cholesterol in elderly individuals and lower risk of late-onset Alzheimer disease. *Archives of neurology* **67**, 1491–1497 (2010).

7. Sirtori, C. R. *et al.* Cardiovascular status of carriers of the apolipoprotein A-IMilano mutant: the Limone sul Garda study. *Circulation* **103**, 1949–1954 (2001).

8. van Capelleveen, J. C., Bochem, A. E., Motazacker, M. M., Hovingh, G. K. & Kastelein, J. J. Genetics of HDL-C: a causal link to atherosclerosis? *Current atherosclerosis reports* **15**, 1–10 (2013).

9. Tall, A. R. HDL in Morbidity and Mortality: A 40+ Year Perspective. *Clinical Chemistry* **67**, 19–23 (2021).

10. Khera, A. V. *et al.* Cholesterol efflux capacity, high-density lipoprotein function, and atherosclerosis. *New England Journal of Medicine* **364**, 127–135 (2011).

11. Lee, C. D., Tse, W., Smith, J. D. & Landreth, G. E. Apolipoprotein E promotes β-amyloid trafficking and degradation by modulating microglial cholesterol levels. *Journal of Biological Chemistry* **287**, 2032–2044 (2012).

12. Marsche, G., Stadler, J. T., Kargl, J. & Holzer, M. Understanding myeloperoxidase-induced damage to HDL structure and function in the vessel wall: implications for HDL-based therapies. *Antioxidants* **11**, 556 (2022).

13. Holzer, M. *et al.* Myeloperoxidase-derived chlorinating species induce protein carbamylation through decomposition of thiocyanate and urea: novel pathways generating dysfunctional high-density lipoprotein. *Antioxidants & redox signaling* **17**, 1043–1052 (2012).

14. Nakajima, T. *et al.* Localization of oxidized HDL in atheromatous plaques and oxidized HDL binding sites on human aortic endothelial cells. *Annals of clinical biochemistry* **37**, 179–186 (2000).

15. Pennathur, S. *et al.* Human atherosclerotic intima and blood of patients with established coronary artery disease contain high density lipoprotein damaged by reactive nitrogen species. *Journal of Biological Chemistry* **279**, 42977–42983 (2004).

16. Van Lenten, B. J. & Roheim, P. S. Changes in the concentrations and distributions of apolipoproteins of the aging rat. *Journal of Lipid Research* **23**, 1187–1195 (1982).

17. Bergt, C. *et al.* The myeloperoxidase product hypochlorous acid oxidizes HDL in the human artery wall and impairs ABCA1-dependent cholesterol transport. *Proceedings of the National Academy of Sciences* **101**, 13032–13037 (2004).

18. Hoang, A. *et al.* Advanced glycation of apolipoprotein AI impairs its anti-atherogenic properties. *Diabetologia* **50**, 1770–1779 (2007).

19. Low, H. *et al.* Advanced glycation end-products (AGEs) and functionality of reverse cholesterol transport in patients with type 2 diabetes and in mouse models. *Diabetologia* **55**, 2513–2521 (2012).

20. Lê, Q. H. *et al.* Glycoxidized HDL, HDL enriched with oxidized phospholipids and HDL from diabetic patients inhibit platelet function. *The Journal of Clinical Endocrinology & Metabolism* **100**, 2006–2014 (2015).

21. Krishnan, S. *et al.* Combined high-density lipoprotein proteomic and glycomic profiles in patients at risk for coronary artery disease. *Journal of proteome research* **14**, 5109–5118 (2015).

22. Krishnan, S. *et al.* HDL Glycoprotein Composition and Site-Specific Glycosylation Differentiates Between Clinical Groups and Affects IL-6 Secretion in Lipopolysaccharide - Stimulated Monocytes. *Scientific Reports* **7**, 1–15 (2017).

23. Nguyen, S. D. *et al.* Spontaneous remodeling of HDL particles at acidic pH enhances their capacity to induce cholesterol efflux from human macrophage foam cells. *Journal of lipid research* **53**, 2115–2125 (2012).

24. Nadeem, N. *et al.* The two faces of α-and γ-tocopherols: an in vitro and ex vivo investigation into VLDL, LDL and HDL oxidation. *The Journal of nutritional biochemistry* **23**, 845–851 (2012).

25. Clevidence, B. A. & Bieri, J. G. [4] Association of carotenoids with human plasma lipoproteins. in *Methods in enzymology* vol. 214 33–46 (Elsevier, 1993).

26. Connor, W. E., Duell, P. B., Kean, R. & Wang, Y. The prime role of HDL to transport lutein into the retina: evidence from HDL-deficient WHAM chicks having a mutant ABCA1 transporter. *Investigative ophthalmology & visual science* **48**, 4226–4231 (2007).

27. Landrum, J. T. & Bone, R. A. Lutein, zeaxanthin, and the macular pigment. *Archives of biochemistry and biophysics* **385**, 28–40 (2001).

28. Ata, S. *et al.* Consumption of either one egg or lutein-enriched egg per day increases HDL cholesterol, reduces apolipoprotein B while increasing plasma carotenoids and macular pigment density in adult subjects. *The FASEB Journal* **24**, 92–4 (2010).

29. Blesso, C. N., Andersen, C. J., Bolling, B. W. & Fernandez, M. L. Egg intake improves carotenoid status by increasing plasma HDL cholesterol in adults with metabolic syndrome. *Food & function* **4**, 213–221 (2013).

30. Murillo, A. G. *et al.* Compared with powdered lutein, a lutein nanoemulsion increases plasma and liver lutein, protects against hepatic steatosis, and affects lipoprotein metabolism in guinea pigs. *The Journal of nutrition* **146**, 1961–1969 (2016).

31. Kang, J. W. *et al.* Multi-omic Analyses Reveal Bifidogenic Effect and Metabolomic Shifts in Healthy Human Cohort Supplemented with a Prebiotic Dietary Fiber Blend. *Frontiers in Nutrition* 1242.

32. Zheng, J. J. *et al.* Isolation of HDL by sequential flotation ultracentrifugation followed by size exclusion chromatography reveals size-based enrichment of HDL-associated proteins. *Scientific reports* **11**, 1–15 (2021).

33. Goulinet, S. & Chapman, M. J. Plasma LDL and HDL subspecies are heterogenous in particle content of tocopherols and oxygenated and hydrocarbon carotenoids: relevance to oxidative resistance and atherogenesis. *Arteriosclerosis, thrombosis, and vascular biology* **17**, 786–796 (1997).

34. Schindelin, J. *et al.* Fiji: an open-source platform for biological-image analysis. *Nature methods* **9**, 676–682 (2012).

35. Hong, B. V. *et al.* High-Density Lipoprotein Changes in Alzheimer's Disease Are APOE Genotype-Specific. *Biomedicines* **10**, 1495 (2022).

36. Minami-Takano, A. *et al.* The association between impairment of HDL cholesterol efflux capacity and atrial remodeling in atrial fibrillation. *Scientific Reports* **11**, 1–10 (2021).

37. Gan, K. N., Smolen, A., Eckerson, H. W. & La Du, B. N. Purification of human serum paraoxonase/arylesterase. Evidence for one esterase catalyzing both activities. *Drug Metabolism and Disposition* **19**, 100–106 (1991).

38. Kishimoto, Y. *et al.* Additional consumption of one egg per day increases serum lutein plus zeaxanthin concentration and lowers oxidized low-density lipoprotein in moderately hypercholesterolemic males. *Food Research International* **99**, 944–949 (2017).

39. Dwyer, J. H. *et al.* Oxygenated carotenoid lutein and progression of early atherosclerosis: the Los Angeles atherosclerosis study. *Circulation* **103**, 2922–2927 (2001).

40. Severins, N., Mensink, R. & Plat, J. Effects of lutein-enriched egg yolk in buttermilk or skimmed milk on serum lipids & lipoproteins of mildly hypercholesterolemic subjects. *Nutrition, Metabolism and Cardiovascular Diseases* **25**, 210–217 (2015).

41. Tall, A. R. & Yvan-Charvet, L. Cholesterol, inflammation and innate immunity. *Nature Reviews Immunology* **15**, 104–116 (2015).

42. Jaouad, L. *et al.* Age-related decrease in high-density lipoproteins antioxidant activity is due to an alteration in the PON1's free sulfhydyl groups. *Atherosclerosis* **185**, 191–200 (2006).

43. Parodi, A. J. Protein glucosylation and its role in protein folding. *Annual review of biochemistry* **69**, 69–93 (2000).

44. Stanhope, K. L. *et al.* Consuming fructose-sweetened, not glucose-sweetened, beverages increases visceral adiposity and lipids and decreases insulin sensitivity in overweight/obese humans. *The Journal of clinical investigation* **119**, 1322–1334 (2009).

45. Malik, V. S. *et al.* Long-term consumption of sugar-sweetened and artificially sweetened beverages and risk of mortality in US adults. *Circulation* **139**, 2113–2125 (2019).

46. Lê, K.-A. & Tappy, L. Metabolic effects of fructose. *Current Opinion in Clinical Nutrition & Metabolic Care* **9**, 469–475 (2006).

47. Feinman, R. D. & Fine, E. J. Fructose in perspective. *Nutrition & metabolism* **10**, 1–12 (2013).

48. Lewis, A. L., Chen, X., Schnaar, R. L. & Varki, A. Sialic acids and other nonulosonic acids. *Essentials of Glycobiology [Internet]. 4th edition* (2022).

49. Draganov, D. I. *et al.* Human paraoxonases (PON1, PON2, and PON3) are lactonases with overlapping and distinct substrate specificities. *Journal of lipid research* **46**, 1239–1247 (2005).

50. Schindler, P. A., Settineri, C. A., Collet, X., Fielding, C. J. & Burlingame, A. L. Site-specific detection and structural characterization of the glycosylation of human plasma proteins

lecithin: cholesterol acyltransferase and apolipoprotein D using HPLC/electrospray mass spectrometry and sequential glycosidase digestion. *Protein Science* **4**, 791–803 (1995).

51. Anantharamaiah, G. *et al.* Effect of oxidation on the properties of apolipoproteins AI and A-II. *Journal of lipid research* **29**, 309–318 (1988).

52. Strittmatter, W. J. *et al.* Binding of human apolipoprotein E to synthetic amyloid beta peptide: isoform-specific effects and implications for late-onset Alzheimer disease. *Proceedings of the National Academy of Sciences* **90**, 8098–8102 (1993).

53. Nagano, Y., Arai, H. & Kita, T. High density lipoprotein loses its effect to stimulate efflux of cholesterol from foam cells after oxidative modification. *Proceedings of the National Academy of Sciences* **88**, 6457–6461 (1991).

54. Ito, F. & Ito, T. High-density lipoprotein (HDL) triglyceride and oxidized HDL: new lipid biomarkers of lipoprotein-related atherosclerotic cardiovascular disease. *Antioxidants* **9**, 362 (2020).

55. Rocha, H. R., Coelho, M. C., Gomes, A. M. & Pintado, M. E. Carotenoids diet: Digestion, gut microbiota modulation, and inflammatory diseases. *Nutrients* **15**, 2265 (2023).

56. Garvey, W. T. *et al.* Effects of insulin resistance and type 2 diabetes on lipoprotein subclass particle size and concentration determined by nuclear magnetic resonance. *Diabetes* **52**, 453–462 (2003).

57. Mora, S. *et al.* Lipoprotein particle size and concentration by nuclear magnetic resonance and incident type 2 diabetes in women. *Diabetes* **59**, 1153–1160 (2010).

58. Dullaart, R. P., Otvos, J. D. & James, R. W. Serum paraoxonase-1 activity is more closely related to HDL particle concentration and large HDL particles than to HDL cholesterol in Type 2 diabetic and non-diabetic subjects. *Clinical biochemistry* **47**, 1022–1027 (2014).

59. Sokooti, S. *et al.* HDL particle subspecies and their association with incident type 2 diabetes: the PREVEND study. *The Journal of Clinical Endocrinology & Metabolism* **106**, 1761–1772 (2021).

60. Wormald, M. R. & Dwek, R. A. Glycoproteins: glycan presentation and protein-fold stability. *Structure* **7**, R155–R160 (1999).

61. Solá, R. J. & Griebenow, K. Effects of glycosylation on the stability of protein pharmaceuticals. *Journal of pharmaceutical sciences* **98**, 1223–1245 (2009).

62. Tang, X. *et al.* Quantitative glycoproteomics of high-density lipoproteins. *RSC advances* **12**, 18450–18456 (2022).

Chapter 4: TEM and convolutional neural network analysis reveals *APOE* genotype-specific correlations between HDL particle size and dementia in patients with Alzheimer's disease

Jack Jingyuan Zheng[1], Brian Vannak Hong[1], Joanne K. Agus[1], Xinyu Tang[1], Fei Guo[2], Carlito B. Lebrilla[3], Izumi Maezawa[4], Lee-Way Jin[4], Wyatt N. Vreeland[5], Dean C. Ripple[5], Angela M. Zivkovic[1]

[1] Department of Nutrition, University of California, Davis, USA

[2] Department of Molecular and Cell Biology, University of California, Davis, USA

[3] Department of Chemistry, University of California, Davis, USA

[4] Department of Pathology and Laboratory Medicine, School of Medicine, University of California, Davis, USA

[5] National Institute of Standards and Technology, Gaithersburg, MD, USA.

1. ABSTRACTS

High density lipoprotein (HDL) cholesterol concentrations are closely related to health and associated with the risk of several chronic conditions, including Alzheimer's disease (AD). However, the relationships between HDL particle size and cognitive impairment are not clear. Negative-stain transmission electron microscopy (NS-TEM) allows direct visualization and size quantification of individual particles. Yet NS-TEM has not been widely used to explore the connections between HDL particle size and disease prediction, mostly due to the difficulty of determining the size of large quantities of particles from TEM images efficiently and accurately. In this study, we report a method for measuring the diameter of over 1,800,000 HDL particles from TEM micrographs of 183 study participants with AD, mild cognitive impairment (MCI), or without dementia (Control) using the deep learning-based object detector You Only Look Once (YOLOv7). The model was trained with 14,990 HDL particles from different randomly selected micrograph fractions. The precision and recall of the model was characterized with 1641 HDL particles from 20 randomly selected micrograph fractions. The accuracy of HDL diameter measurement was compared to the area reported ImageJ image-processing software. The different-day coefficient of variance of the size-standard diameter in TEM micrographs was 0.85%. The model's precision and recall was 89.0% ± 5.08% and 78.0% ± 15.2%, respectively. The average area measurement difference compared to ImageJ manual selection was 2.9% and not significantly different. Particle sample size simulation showed that at least 2,500 particles should be included in order to estimate the mean HDL diameter from a study participant accurately. HDL particle diameters from micrographs of 183 clinical samples (> 10,000 particles/sample) were measured by the model. HDL particles from participants with AD and MCI showed more small HDL subclasses compared to Controls, and were further modified by

the participants' *APOE* genotype. In participants with the *APOE* ε3ε3 genotype, abundance of HDL with diameter ≤ 9.5 nm negatively associated with HDL functions, but had mixed correlations with cognitive measurements; in participants with the *APOE* ε3ε4 genotype, abundance of HDL with diameter ≤ 9.5 nm negatively associated with cognitive measurements, but positively associated with HDL functions. Our results show that accurate individual HDL particle diameter measurement from TEM micrographs for clinical samples is possible using the YOLOv7-assissted method, and can be expanded to characterize the relationship between HDL diameter and other diseases.

2. INTRODUCTION

High density lipoprotein (HDL) is central to cholesterol transport and metabolism of the human body [1]. HDL cholesterol concentration and HDL functions have been found to be associated with cardiovascular disease, obesity, type II diabetes, neurodegenerative disease, and metabolic chronic diseases [2–4]. The HDL population consists of heterogeneous particles that can be categorized by fine diameter ranges [5,6], and there is growing evidence on the associations between the abundance of specific HDL subclasses and disease risk. For example, an increase in HDL2b, which are very large HDL, has been associated with a reduced risk of coronary heart disease (CHD) [7]. The role of small HDLs in chronic disease is less well understood: the concentration of the small HDL3b subfraction was associated with an atherogenic lipoprotein profile [8]; in contrast other studies show small HDLs are more anti-inflammatory and anti-oxidative because more paraoxonase-1, an arylesterase involved in neutralizing pro-oxidative molecules like lipid peroxides, was found to be associated with the small HDL subfraction [9]. Additionally, recent studies suggest that the size of HDL-like particles in the cerebrospinal fluid is correlated with the risk of AD development [10,11].

Several techniques can measure the size of HDL particles or isolate HDL particles by their size. These include analytical ultracentrifugation [12], size-exclusion chromatography (SEC) with tandem protein concentration detection [13], nondenaturing gradient gel electrophoresis (NDGGE) [14], 2-dimensional gel electrophoresis (2DGE) [15], electron microscopy [16], nuclear magnetic resonance spectroscopy (NMR) [17], ion mobility (IM) [18], and batch dynamic light scattering (batch-DLS) [19]. However, each of these techniques has limitations, especially for measuring heterogeneously sized particles like lipoproteins. For example, batch-DLS only measures a weighted-average particle size value that is strongly influenced by the presence of

large particles (including larger lipoprotein particles and extracellular vesicles) [20]. NDGGE characterizes the size distribution of lipoprotein particles into subfraction HDL3 (3a, 3b, 3c) and HDL2 (2a, 2b) based on the electrophoretic mobility of particles compared to globular protein standards with defined molecular weight [6]. However, the band-broadening effect during particle migration through a gel often hinders accurate characterization of HDL particle subclasses. Further, the globular protein mix molecular standard used in NDGGE does not accurately characterize the size of protein-lipid complex nanoparticles such as HDLs.

Negative-stain transmission electron microscopy (NS-TEM) has been used to measure the size of individual HDL particles [16,21]. NS-TEM is the most rigorous technique for accurate HDL particle sizing. Instead of relying on conversion from molecular weight of globular proteins to nanometer units, the diameter of HDL particles from NS-TEM micrographs is calculated based on image analysis of the micrograph, which is calibrated carefully with size standards with known nanometer values[22]. But its poor economy of scale limits its application in clinical diagnostic labs. In practice NS-TEM is most often used to explore HDL interaction with other molecules and cells [23,24] or to substantiate the validity of other sizing methods [25]. Another challenge is the availability of a large dataset from NS-TEM micrographs for size analysis, which usually requires either manual particle picking on an enlarged micrograph [26] or customarily coded script to work with specific image analysis software, such as ImageJ [27], Image Pro Plus [28] or IMAQ Vision software [29]. The same image processing parameters that work for one micrograph often fail to work optimally on another with different background intensity, defocus, sample preparation, signal-to-noise ratio, or the combination of these. Even in the limited studies that utilized NS-TEM micrographs for HDL size measurement, the number of particles included for data analysis varied between different studies, ranging from $40 < n_{\text{particle}} <$

500 [26–28,30] with no consensus on the appropriate particle sample size to estimate the true mean particle diameter of the entire HDL population from a clinical sample accurately. The utility of NS-TEM to evaluate the diameter and abundance of particle subfractions in biological samples, and any extra information high-resolution NS-TEM data may garner, has not been thoroughly evaluated.

In the present study, we utilized the publicly available deep learning object detector You Only Look Once (YOLOv7) [37]to select HDL particles from NS-TEM micrographs. The precision and recall of particle selection by the YOLOv7 model was compared to manual selection. The diameter of HDL particles measured by YOLOv7 was compared to that measured by ImageJ. We further conducted a particle sample size simulation to explore the appropriate number of particles for accurate estimation of population mean HDL diameter for valid comparisons between different individuals. With this method we characterized the HDL diameter distribution of each individual from 183 study participants with Alzheimer's disease (AD, $n = 67$), mild cognitive impairment (MCI, $n = 37$), and without dementia (Control, $n = 79$), and conducted analyses on the associations between the abundance of specific HDL size-based subclasses with participant biometrics and clinical characteristics.

3. METERIALS AND METHODS

Biological samples

The biological samples used for this particle analysis study were obtained from the University of California, Davis, Alzheimer's Disease Research Center (ADRC) Biorepository, a nationally recognized biorepository for recruiting an ethnically diverse elderly cohort [31], which

was described in detail previously [32]. A total of 194 plasma samples were collected, including individuals from the following groups: *n* = 37 AD, *n* = 22 MCI and *n* = 44 Control with *APOE* ε3ε3 genotype, and *n* = 34 AD, *n* = 18 MCI, and *n* = 39 Control with *APOE* ε3ε4 genotype. Out of 194 samples, 183 were included in this analysis. Eleven samples were not included due to poor sample quality for particle size analysis (*n* = 4 for Control, *n* = 3 for MCI, *n* = 4 for AD). The participants were selected to have approximately equal numbers of males and females and equivalent average age within each diagnosis × genotype group. Participants meeting the criteria of having a BMI of no more than 40 kg/m^2, and an available plasma sample volume of 500 µL were included, provided they had been diagnosed with ADRC criteria within one year of their blood draw. Samples were collected between 2002 to 2018 (average storage time = 5638 days), and stored at -80 °C until analysis. The study was approved by the Institutional Review Board of the University of California, Davis.

The participants' neuropsychological function was assessed using the Spanish English Neuropsychological Assessment Scales (SENAS), an established and validated evaluation [33,34]. The SENAS cognitive domains including verbal memory score (VMS), executive function score (EFS), spatial score, and semantic memory score were used for data analysis in this study. A global measure of independent function, including six cognitive domains in memory, orientation, judgement and problem-solving, community affairs, home and hobbies, and personal care was assessed using the Clinical Dementia Rating Scale Sum of Boxes (CDRSOB) [32]. Total white matter hyperintensity volume (WMHV) was measured using magnetic resonance imaging (MRI) with a procedure previously described [35].

HDL and size-standard sample preparation

HDL were isolated from human plasma as described previously [27]. Briefly, HDL fractions were collected from a two-step sequential flotation density ultracentrifugation at 110,000 RPM (657,272×*g*, TLA-110 Fixed-Angle Rotor, k factor = 13, Beckman-Coulter, CA, USA) followed by size-exclusion chromatography (Superdex 200 Increase 10/300 GL agarose-crosslinked column, GE Healthcare, USA), between the elution volume of 9.78 mL and 13.26 mL at a flowrate of 0.5 mL/min in phosphate buffer saline (Sigma-Aldrich, MO, USA, Cat. No.: D8537-1L). Samples were cleaned and concentrated using Amicon Ultra-4 50 kDa centrifugal filters (MilliporeSigma, MA, USA) at 4500 RPM (1100×*g*) for 8 min using a Sorvall Legend XF centrifuge (Thermo Fischer Scientific, MA, USA). Isolated HDL samples were stored at -80 °C with 2% sucrose as cryoprotectant before use.

The Poly(styrene) latex (PSL) size standard beads (nominal diameter 22 nm ± 2 nm, approximate concentration: 1% solids, Thermo Fisher, USA, Cat. No.:3020A) were homogenized by gentle inversion several times and sonicated for 10 seconds according to the manufacturer's recommendation, and diluted 1:24 (v:v) with deionized water to produce a concentration suitable for NS-TEM visualization.

Negative-stain electron microscopy

The isolated HDL samples from study participants were thawed on ice and diluted with deionized water to achieve 50 µg/mL total protein concentration. PSL size standard was diluted from stock with deionized water at the ratio of 1:24 (v:v) for each sample imaging session to account for possible daily variations in TEM magnification. For sample loading, 4 µL PSL size standard or human HDL isolate were loaded on glow-discharged carbon-coated TEM grids

(TedPella Inc., CA, USA). After 1 minute of sample binding, excessive sample solution was removed by blotting with filter paper. The grid was then stained with 4 μL of 2% (w/v) uranyl formate (pH 4.6), and quickly blotted with a filter paper to remove excess stain in a dark environment. The staining process was repeated 4 more times. After the last stain solution was removed, the grid was left to air dry in the dark at room temperature according to published optimized protocols [27,36]. When ready, the grids were examined with a Talos L120C electron microscope (Thermo Fisher, MA, USA) at 80 kV HT and 36,000x magnification. Micrographs were captured with a defocus between 1.5 nm and 2.0 nm and an exposure time of 300 ms with a 4096 px × 4096 px (2.4 pixels = 1 nm) resolution. Micrographs that were clearly of poor quality or void of samples were discarded. Five micrographs were taken for the PSL size standard, and more than 20 micrographs were taken for each study participant's HDL sample.

HDL particle selection and sizing with Roboflow and YOLOv7 model training

HDL particles used for the training and testing set were manually selected on the Roboflow (https://roboflow.com/) using the Instance Segmentation mode.

YOLOv7 Instance Segmentation (YOLOv7-seg) is the image segmentation module of YOLOv7 [37]. This module is implemented based on YOLOv5, with the algorithm interlinked with the YOLOv7 object detection weights. The comprehensive architecture of YOLOv7 instance segmentation is depicted in Supplemental Figure S4.1. It includes the backbone network to extract features from the input image, followed by a neck based on the Path Aggregation Network (PANet), and the head network to generate classes, objectness scores, bounding boxes, and segmentation masks for object instances in the input image.

Backbone: Images sized 512 x 512 x 3 were provided to the YOLOv7-seg backbone. The backbone of YOLOv7-seg was built using convolution blocks and Efficient Layer Aggregation Network (ELAN) blocks to extract image features across the entire image [38]. Its architecture comprises five stage layers that extract features from low to high levels. The first stage layer includes three convolution blocks. The second stage contains a convolution block and ELAN block. The third to the fifth stage layers consist of a max-pooling and stride convolution block and an ELAN block. The outputs from the ELAN blocks in the third, fourth, and fifth stage layers extract essential features from an image, further processed via the PANet to obtain feature pyramids.

Neck: PANet serves as the neck in the YOLOv7-seg architecture. The feature maps generated from the backbone are fed into the PANet to combine and mix features, creating a feature pyramid that is then passed to the head for prediction. In the PANet, a top-down path extracts and combines semantically rich features with precise localization information, followed by a bottom-up augmentation path creating shortcuts between the lower layers and the topmost features [39].

Head: The features extracted from the neck undergo a convolution layer for object detection and particle segmentation. At each-sized feature map, the convolution layer is fed to a detection head. The head applies anchor boxes on feature maps and renders classes, objectness scores, and bounding boxes. With the largest feature map, the features are used to generate particle segmentation predictions.

Model Training: The final loss is the sum of the bounding box regression, classification, objectness, and mask regression losses, multiplied by the batch size: $L = (L_{box} + L_{cls} + L_{obj} + L_{seg}) \times bs$, where L_{box} is the box regression loss, L_{cls} is the classification loss, L_{obj} is the objectness

loss, L_{seg} is the mask regression loss, and *bs* is the batch size. The YOLOv7 segmentation model was pretrained on the Microsoft Common Objects in Context (MS COCO) dataset, a widely used dataset for computer vision [40]. We used the weights obtained from the pretrained model for transfer learning. A total of 299 TEM images, sized 512×512, were used for training, along with 20 images for validation. The training images were augmented with flip, rotation, brightness, exposure, blur, noise, mosaic, and other augmentation methods. Ultimately, 897 images (14990 particles) were used to train the model, with a batch size of 16, an epoch of 20, learning rate of 0.01, momentum of 0.937, weight decay of 0.0005 (Figure 4.1). Python version was 3.10.12, torch version was 2.1.0.

The trained model was deployed to predict HDL particles in micrographs on a remote computing resource service. The processing time for each 512×512 micrograph was ~30 ms. Data output from model prediction contains the following information on each selected particle: particle label, index, normalized particle's center of mass x-position on the micrograph, normalized particle's center of mass y-position on the micrograph, normalized particle width, normalized particle height, and pixels of particle's area. The diameters of particles were converted and calculated from pixel to nanometer using the resolution of the TEM micrograph (2.4 px/nm). The selected particles were classified as intersecting the edges if their normalized center-of-mass x or y coordination were less than 0 or greater than 1 after deducing or adding, respectively, half of their normalized width (for x-coordinate) or height (for y-coordinate).

The model output for the 20-micrograph validation dataset was used to establish the precision and recall of the model. Precision was defined as true positive/(true positive + false positive) and recall was defined as true positive/(true positive + false negative). True positive, false positive and false negative were determined manually as follow:

- True positive: particles that were selected by YOLOv7 that are manually agreed to be classified as a particle.
- False positive: particles that were selected by YOLOv7 that are not manually agreed to be classified as a particle.

False negative: particles that were not selected by YOLOv7 that are manually agreed to be classified as a particle.

Particle sample size simulation

To measure how the sample size of particles ($n_{(particles)}$) affects the accuracy of estimating the true mean (μ) of HDL population within a study participant's sample, we ran a computer simulation with different sample sizes from $n_{(particles)}$ = 1 to $n_{(particles)}$ = 5000 (i.e. $n_{(particles)} = 1, 2, 3, \dots, 5000$). Particles were randomly selected from a population of 10,304 particles from one study participant's HDL micrographs. At each $n_{(particles)}$, random sampling was repeated 100 times with replacement.

The means of 100 random sampling iterations were constructed into a vector ($\bar{Y}$):

$$\bar{\mathrm{Y}}^{n_{(particles)}} = [\bar{\mathrm{y}}_1^{n_{(particles)}}, \bar{\mathrm{y}}_2^{n_{(particles)}}, \bar{\mathrm{y}}_3^{n_{(particles)}}, \dots, \bar{\mathrm{y}}_{100}^{n_{(particles)}}]$$

The probability of sampling distributions of $\bar{\mathrm{Y}}^{n_{(particles)}}$ to fall within either 1%, 5%, or 10% of the μ was calculated and reported as the "closeness to population mean" within 1%, 5%, or 10% error. Procedures are shown in Supplemental Figure S4.2.

ImageJ particle analysis

Particle diameter was measured using an open-source image analysis software ImageJ [41] with a customized script as a template to evaluate the diameter predicted by the YOLOv7 model (Figure 4.1). Twenty selected micrographs were used for direct ImageJ measurement as described previously [27]. The following steps were performed: raw image was adjusted for threshold using the "Default" mode; measurement scale was set at 2.4 pixel/nm; particle analysis was performed using Size = 38.47 – 176.62 nm^2, Circularity = 0.10 – 1.00. Particles that were detected and selected by ImageJ were manually validated by ensuring the selections were appropriately marking the particle of interest. Particle diameter was reported as an equivalent circular diameter, obtained by converting the area of selected particles into diameter with the equation $diameter = 2 \times \sqrt{area/\pi}$.

Particles selected by ImageJ were used to validate the diameter of particles reported by YOLOv7 from the same micrograph. Particles that appeared on both ImageJ and YOLOv7 selections were manually selected. The mean diameter of particles in the ImageJ selection was considered the "ground truth" and compared to the mean diameter of particle in the YOLOv7 selection.

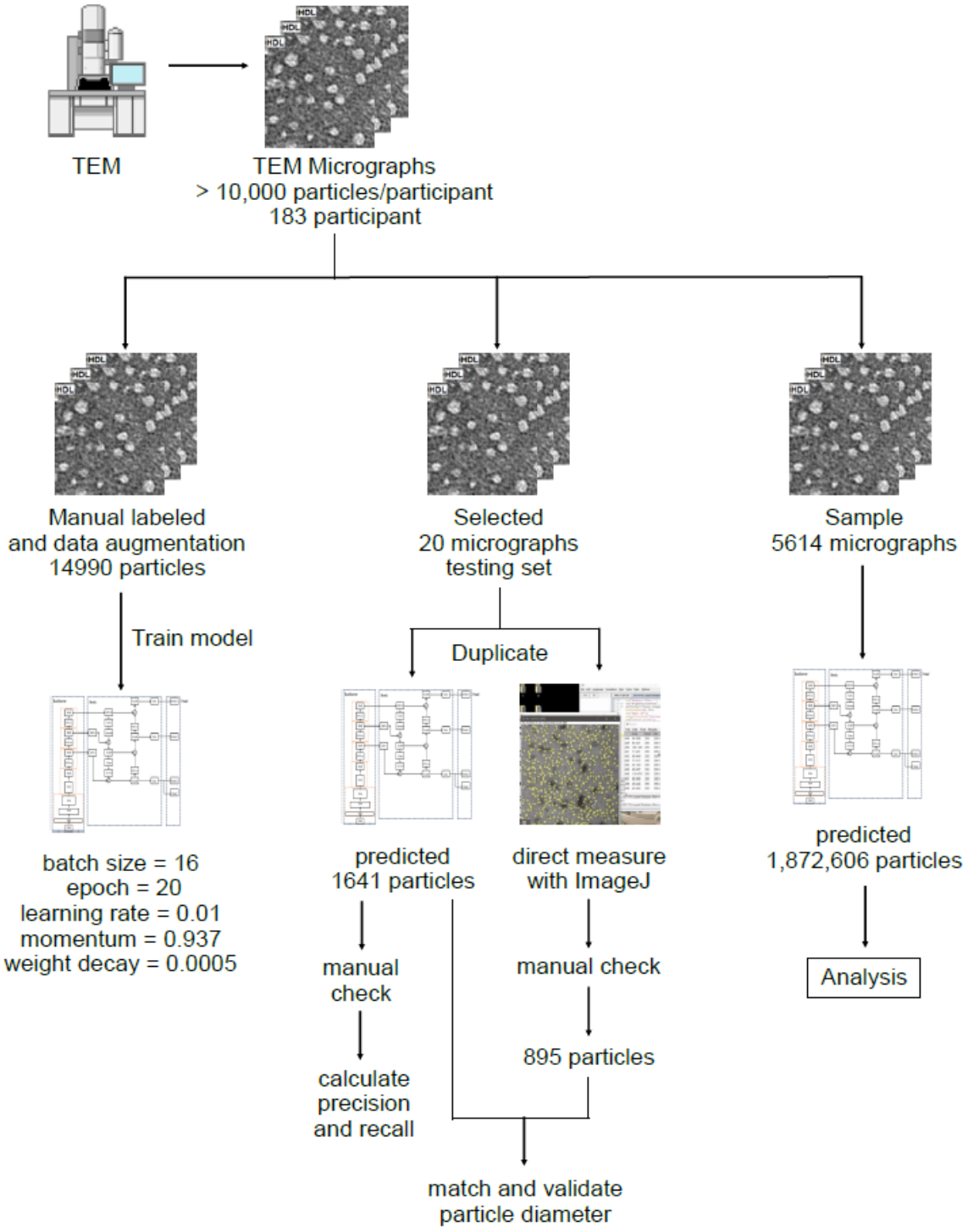

Figure 4.1. Overview of HDL particle diameter measurement from TEM micrographs using a YOLOv7 CNN model.

HDL Functional Activity Assays

The antioxidant activity of HDL samples was assessed by following a published PON1 activity assay method [42]. Briefly, 10 μg HDL sample was mixed with 2 mmol/L paraoxon (Sigma, MO, USA.) in a 100 mmol/L Tris buffer (Sigma, MO, USA) with 2 mmol/L $CaCl_2$ (Sigma, MO, USA). The production of 4-nitrophenol was monitored at 37 °C every 5 minutes by optical absorption at 405 nm and calculated using Beer's Law with the extinction coefficient of 4-nitrophenol equal to 17,100 L/mol. PON1 activity of the sample was reported as nM 4-nitrophenol/minute. CEC, and LCAT activity data were obtained from a study published previously [32]. Briefly, in the CEC assays, J774A.1 cells (ATCC, Manassas, VA, USA, catalog TIB-67) were seeded at 100,000 cells per well for 4 hours in medium containing 10% fetal bovine serum and 100 μg/mL penicillin and streptomycin. Cells were then incubated with labeled fluorescent cholesterol (Abcam, Cambridge, UK) for 4 hours, followed by incubation with 10 μg of HDL protein for another 4 hours. The fluorescent emission at 515 nm was measured for the cell media and the cell lysate at an excitation wavelength of 482 nm. In the LCAT activity assays, the reaction mixture was prepared from a commercially available kit (Roar Biomedical, Millipore Sigma, Burlington, MA, USA) and 5 μg HDL following the manufacturer's instruction. The fluorescence of the reaction product was measured at excitation = 340 nm and emission = 390 nm and 470 nm. LCAT activity was calculated as the ratio between fluorescence intensities at 390 nm and 470 nm.

Particle analysis on HDL samples from human with AD, MCI, and without cognitive decline

HDL particles from human sample micrographs were predicted with the trained YOLOv7 model (Figure 4.1). A total of 5614 micrographs were obtained from 183 study participants. The diameter of each predicted particle was reported as the equivalent circular diameter. Particles were grouped into the following diameter range subclasses: H1P: 7.4 nm ≤ diameter ≤ 7.8 nm; H2P: 7.8 nm ≤ diameter ≤ 8.7 nm; H3P: 8.7 nm ≤ diameter ≤ 9.5 nm; H4P: 9.5 nm ≤ diameter ≤ 10.3 nm; H5P: 10.5 nm ≤ diameter ≤ 10.8 nm; H6P: 10.8 nm ≤ diameter ≤ 12.0 nm; H7P: 12.0 nm ≤ diameter ≤ 13.0 nm. Abundance of each subclass was calculated by:

$$abundance\ (\%) = 100\% \times \frac{particles\ in\ the\ selected\ subclass}{total\ particles\ in\ all\ subclasses}$$

The similarity index of particle diameter distribution profile was calculated by:

$$Similarity\ index = 1 - RMSD$$

where RMSD is the root-mean-square deviation (RMSD) between the two diameter distribution curves in each comparing pair. RMSD is an estimator for structural similarity [43]. The RMSD value between two distribution curves was calculated as:

$$RMSD = \sqrt{\frac{1}{N}\sum_{i=1}^{N}\delta_i^2}$$

where δ_i is the difference of bin abundance of the i^{th} bin between the two comparing particle populations, and N is the total number of bins. In this report, we used a bin size of 0.1 nm for RMSD calculations. Thus, N = (20 nm – 7 nm) ÷ 0.1 nm = 140 bins. The similarity index was calculated for every pair of study participants combination.

Statistical analysis

All statistical analyses were done using statistical software R version 4.1.1[44] and Microsoft Excel (Microsoft, WA, USA). For method characterization, mean diameter of particles measured using YOLOv7 and ImageJ was tested with Student's t-test. The null hypothesis of no difference between different sizing methods was rejected if $p < 0.05$. Differences in HDL subclass abundance and HDL diameter profile similarity between AD, MCI, and Control groups were tested with one-way ANOVA. The null hypothesis of no difference between groups was rejected if $p < 0.05$. A post-hoc pair-wise comparison with Benjamin-Hochberg [45] adjustment was conducted when a significant difference was observed. Correlation analysis between particle subclass abundance and the cognitive, functional, MRI assessments, or key participant baseline measurements were conducted using Spearman's correlation. The correlation between variables is reported as Spearman's correlation, rho (ρ), and the significant values of correlations were adjusted using the Benjamini-Hochberg procedure[45]. Statistically significant findings are indicated as shown: * $p < 0.05$, ** $p < 0.01$, *** $p < 0.001$, and **** $p < 0.0001$.

4. RESULTS

HDL particle diameter measurement on NS-TEM micrographs with YOLOv7 model

The different-day mean diameter of PSL size standards was 17.4 nm ± 0.43 nm (CV = 2.5%, Figure 4.2A). The precision and recall of the YOLOv7 model on a test set image (n_{image} = 20) was 89.0% ± 5.08% (Figure 4.2B) and 78.0% ± 15.2% (Figure 4.2C). From 1641 particles predicted by YOLOv7, 895 particles overlapped with particles selected by ImageJ. Of the 895 particles measured by both methods, there was no significant difference in particle diameter measured by the two sizing methods (Figure 4.2D).

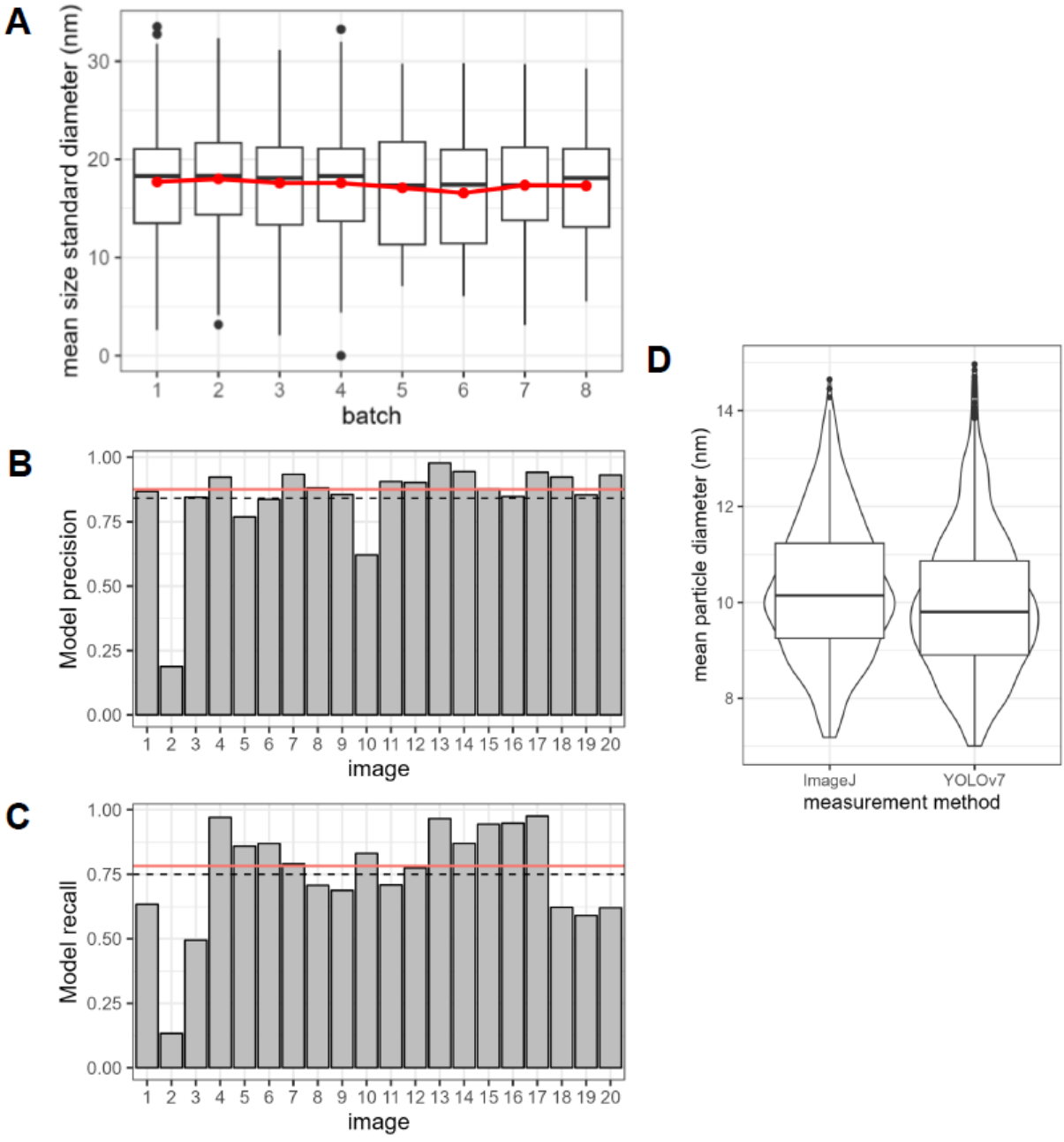

Figure 4.2. Characteristics of YOLOv7-assisted particle diameter measurement using TEM.(A) Mean particle diameter between days of measurements. Red dots show the mean particle diameter of each day's measurements, linked by a red line. (B) precision and (C) recall of the model on predicting HDL particles. Dashed lines represent the overall average value; red solid line

represents the average value after removing the outlier data of image 2. (D) comparison of particle diameter measured by ImageJ and YOLOv7.

HDL sample size simulation

There is no consensus in the sample size of HDL that needs to be analyzed for an accurate estimate of the population mean. Therefore, we performed an HDL particle sample size simulation. The mean diameter of all 10,304 particles in a study participant's micrographs was 9.69 nm ± 1.57 nm and was taken to be an accurate estimate of the true mean and true standard deviation. Sample sizes from $n_{(particle)} = 1$ to $n_{(particle)} = 5000$ were randomly selected from the population, and the random selection of each $n_{particle}$ was repeated 100 times to obtain a set of sample means ($\bar{Y}$). The probability of the sample means to fall within 1%, 5%, or 10% deviation from 9.69 nm are summarized in Supplemental Figure S4.4. The sample size to achieve a sample mean with decent probability to estimate μ at 1% error required $n_{particles} \geq 2{,}500$ particles (Supplemental Figure S4.4A); the sample size of that to estimate μ at 5% error required $n_{particles} \geq 120$ particles (Supplemental Figure S4.4B); the sample size of that to estimate μ at 10% error required $n_{particles} \geq 20$ particles (Supplemental Figure S4.4C).

HDL diameter profile and subclass comparisons between the AD, MCI, and Control group

We first determined the overall particle diameter distribution by plotting the abundance of particles across a continuous range from 7 nm to 13 nm. Figure 4.3A shows the continuous HDL particle diameter distribution of the Control (pink), MCI (green), and AD (blue) groups. There is a clearly visible increased abundance in particles within the 7 nm – 9 nm diameter range and

reduced abundance in particles within the 9 nm – 13 nm diameter range in the MCI and AD groups compared to the Control group (Figure 4.3A).

We next grouped the continuous particle diameter data into diameter-based subclasses using legacy size range cutoffs commonly used for describing HDL subclasses [17] (Figure 4.3). Among samples from all study participants (i.e. when including both *APOE* genotypes), the Control group had a lower percentage abundance of small HDL subclasses: H1P (7.4 nm – 7.8 nm) and H2P (7.8 nm – 8.7 nm) compared to both the MCI and AD groups (Figure 4.3B). There was no difference in the relative amount of H3P particles (8.7 nm – 9.5 nm). In contrast, the Control group had more medium-to-large HDL subclasses: H4P (9.5 nm – 10.3 nm), H5P (10.3 nm – 10.8 nm), and H6P (10.8 nm – 12.0 nm) compared to both the MCI and AD groups (Figure 4.3B).

Previously, our group found that the average HDL particle diameter was different between the Control, MCI, and AD groups only in participants with the *APOE* ε3ε4 genotype but not in those with the *APOE* ε3ε3 genotype [32]. In this study we further explored the changes in the abundances of specific HDL subclasses among the diagnosis groups of these two *APOE* genotypes.

In participants with the *APOE* ε3ε3 genotype, the Control group had higher variability in the abundances of several of the HDL subclasses, including H2P, H3P and H6P particles, with as low as 5% to as high as 35% of HDL being in the H2P size range, for example (Figure 4.3C). In the participants with the *APOE* ε3ε3 genotype there was also discordance between the MCI and AD groups compared to Controls, where for most of the HDL subclasses there was only a difference between the Control and MCI patients but not between the Control and AD patients.

For example, particles in the H5P size range (10.3 nm – 10.8 nm) were lower in the MCI patients but not the AD patients compared to Controls (Figure 4.3C).

On the other hand, in participants with the *APOE* ε3ε4 genotype, there was generally a progressively higher difference between the Controls and AD patients, with MCI patients intermediate between the two (Figure 4.3C, D). For example, in participants with the *APOE* ε3ε4 genotype the Control group had lower H1P and H2P abundance (Figure 4.3D) but higher H4P and H5P abundance than both the MCI and AD patients (Figure 4.3D), with MCI patients intermediate between the Controls and AD patients. Interestingly, there was a directionally different relationship between the H3P particle subclass and clinical diagnosis. Whereas Controls with the *APOE* ε3ε3 genotype had lower relative abundances of H3P particles compared to cognitively impaired patients (Figure 4.3C), Controls with the *APOE* ε3ε4 genotype had higher relative abundances of these particles compared to cognitively impaired patients. Detailed HDL subgroup abundance information is described in Supplemental Table S4.1.

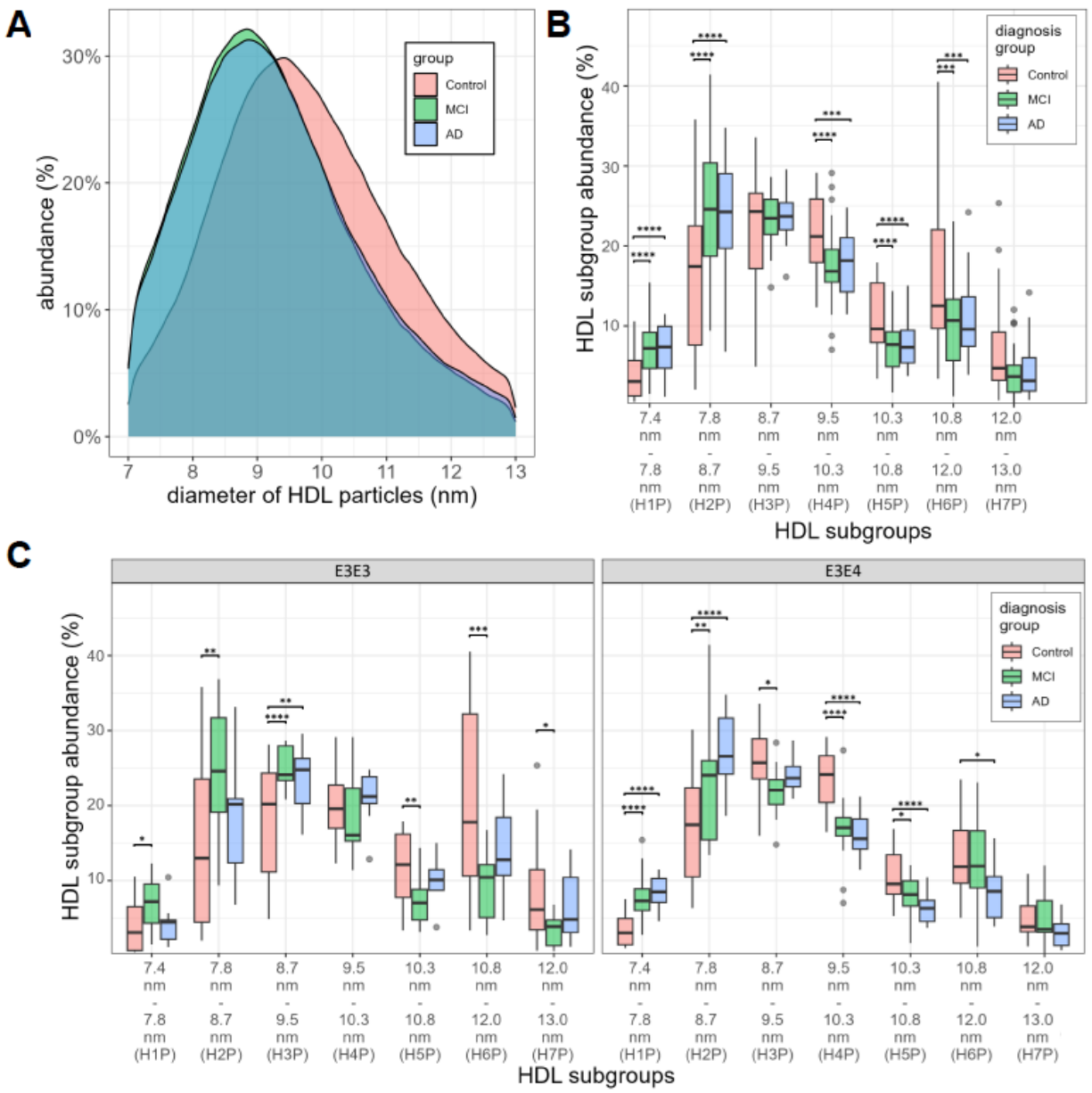

Figure 4.3. High density lipoprotein (HDL) particle diameter distribution of individuals with normal cog-nition (NC), mild cognitive impairment (MCI), and Alzheimer's disease (AD).(A) Continuous population density curves of HDL particle diameter distribution for each study group. (B) Comparisons of HDL subclass abundance across all subclasses defined by NMR Lipo-profile size cutoffs. (C) Comparisons HDL subclasses in samples from participants with *APOE*ε3ε3 genotype and participants with *APOE*ε3ε4 genotype.

Correlations between HDL subclass abundance, HDL functions and participant cognitive measurements

The relationships between HDL diameter-based subclass abundance and participant characteristics were also *APOE* genotype-specific. Notably, in participants with the *APOE* ε3ε3 genotype HDL subclass abundance was not significantly correlated with BMI (Figure 4.4A). Also of note, the abundance of particles in the H3P size range (8.7 nm – 9.5 nm) showed negative correlations with multiple clinical cognitive measures including verbal memory, executive function, and spatial function, as well as positive correlations with both the clinical dementia rating (a measure of the degree of dementia) and with white matter hyperintensity volume (an MRI readout of the extent of chronic cerebrovascular damage) (Figure 4.4A, Table S4.2). White matter hyperintensity volume was also positively correlated with the abundance of the smallest H1P and H2P particles, and negatively correlated with the larger H4P, H5P, H6P, and H7P particles (Figure 4.4A, Table S4.2). In participants with the *APOE* ε3ε3 genotype generally the abundance of the smaller HDL particles (H1P, H2P, H3P) was negatively correlated with the functionality of HDL particles whereas the abundance of the larger HDL particles (H4P, H5P, H6P, and H7P) was positively correlated with the functionality of HDL particles, including cholesterol efflux capacity, LCAT activity, and antioxidant capacity (Figure 4.4A, Table S4.2).

On the other hand, in participants with the *APOE* ε3ε4 genotype, BMI was strongly correlated with HDL subclass abundance (Figure 4.4B, Supplemental Table S4.2), with the abundances of the smaller H1P and H2P particles positively associated with BMI whereas the abundances of the larger H4P, H5P, H6P, and H7P particles negatively associated with BMI. In general there were less and weaker correlations between HDL subclasses and HDL functions in

the *APOE* ε3ε4 participants, with several being in the opposite direction from those in the *APOE* ε3ε3 participants (Figure 4.4B, Table S4.2). For example, cholesterol efflux capacity was positively correlated with the abundance of the smaller HDL particles (H1P, H2P) in *APOE* ε3ε4 participants, whereas the opposite was the case in the *APOE* ε3ε3 participants. In the *APOE* ε3ε4 participants there were more and much stronger correlations between HDL particle subclasses and multiple measures of cognitive function in all but the H3P subclass. The abundance of smaller particles (H1P, H2P) was negatively correlated with all measures of cognitive function (verbal memory, executive function, semantic and spatial cognition), and positively correlated with the degree of dementia, measured by the clinical dementia rating score. The opposite was the case with the abundance of the larger HDL particles (H4P-H7P), which were positively correlated with cognitive function and negatively correlated with clinical dementia rating (Figure 4.4B, Table S4.2).

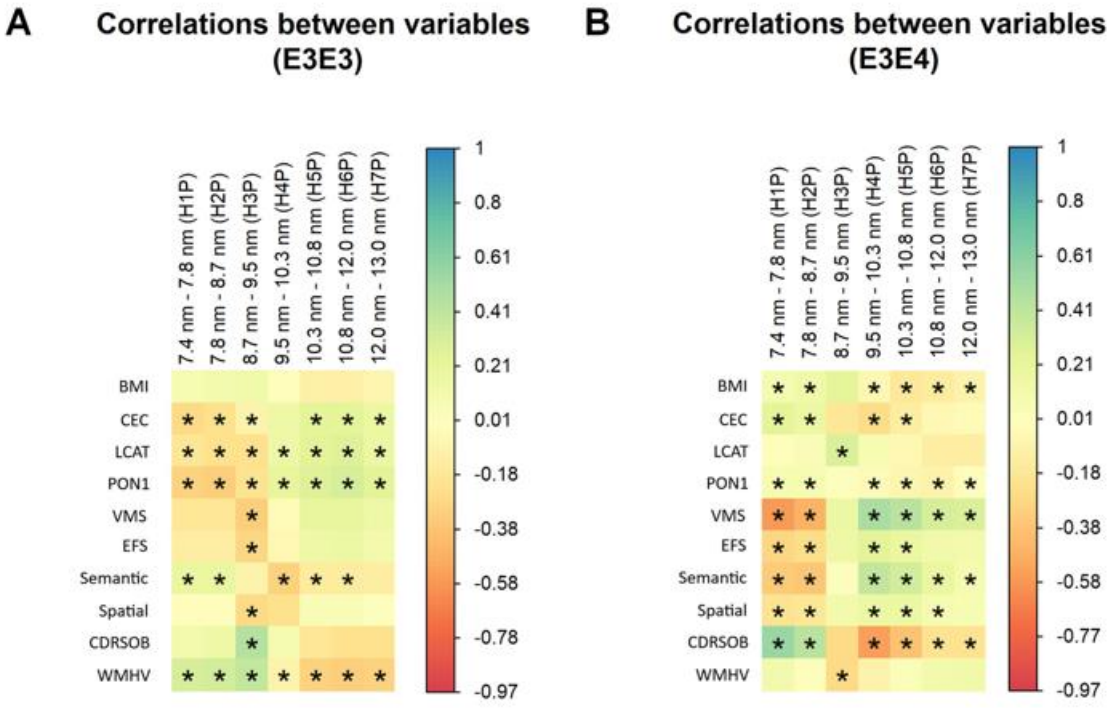

Figure 4.4. Correlations between HDL subclass abundance and participant characteristics. (A): participants with *APOE* ε3ε3 genotype. (B): participants with *APOE* ε3ε4 genotype. Correlations between two variables are described in their intersecting squares. Positive correlations are represented with green color. Negative correlations are represented with orange color. Statistically significant (p-value < 0.05) correlations are notified by an asterisk (*) in the square. H1P = abundance of particles between 7.4 nm – 7.8 nm; H2P = abundance of particles between 7.8 nm – 8.7 nm; H3P = abundance of particles between 8.7 nm – 9.5 nm; H4P = abundance of particles between 9.5 nm – 10.3 nm; H5P = abundance of particles between 10.3 nm – 10.8 nm; H6P = abundance of particles between 10.8 nm – 12.0 nm; H7P = abundance of particles between 12.0 nm – 13.0 nm; BMI =body mass index (kg/m2) of the individuals at blood collection; CEC = cholesterol efflux capacity index of HDL; LCAT = lecithin-cholesterol acyltransferase activity; PON1 = paraoxonase-1 activity; VMS = verbal memory score; EFS = executive function score; Semantic = semantic memory score; Spatial = spatial score; CDRSOB = clinical dementia rating sum of boxes score; WMHV = white matter hyperintensity volume.

Participants with dementia diagnosis or APOE ε3ε4 genotype have more similar HDL distribution patterns than other groups

The metabolism and remodeling of HDL particles can be altered by certain metabolic conditions, and therefore a more similar HDL size distribution pattern among participants may be indicative of a commonly shared underlying metabolic trait. We explored whether the size distribution pattern of HDL from the study participants was associated with diagnosis group or *APOE* genotype by comparing their similarity indices. We first calculated the similarity between diameter distribution curves in 5 images of the same PSL size standard beads as 99.1% ± 0.691%

(CV = 0.697%), and the similarity between 5 images of the same participant sample as 97.0% ± 0.614 (CV = 0.633%). Among the Control, MCI, and AD diagnosis groups, the Control group (98.5% ± 0.864%), had a lower similarity index compared to the MCI (99.0% ± 0.590%, $p < 0.001$) and the AD (99.0% ± 0.619%, $p < 0.001$) groups (Figure 4.5A). Genotype-wise, participants with the *APOE* ε3ε3 genotype (98.6% ± 0.900%) had a lower similarity index than those with the *APOE* ε3ε4 genotype (98.9% ± 0.638%, $p < 0.001$) (Figure 4.5B).

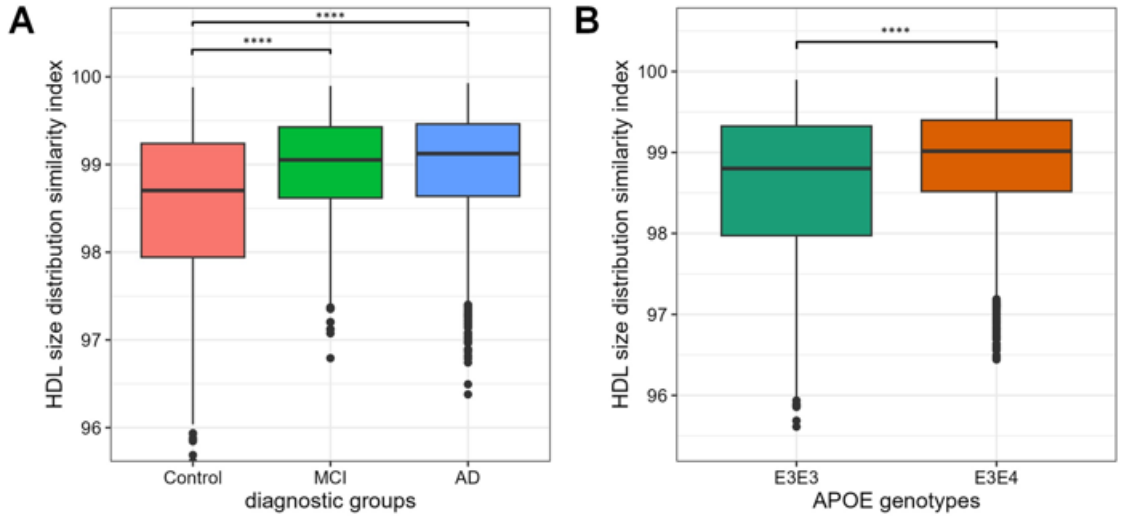

Figure 4.5. HDL size distribution similarity index comparison between participants. (A): comparisons of similarity index between different dementia diagnosis, and (B): the comparison of similarity index between different *APOE* genotypes. $^{****}p < 0.001$.

5. DISCUSSIONS

In this study we combined the use of a standardized approach for imaging isolated HDL particles from large numbers of clinical samples with NS-TEM, with the YOLOv7 CNN model and a bespoke script to automate HDL particle size measurement in the obtained NS-TEM

micrographs. The model was trained using 14990 particles and achieved average model precision of 89.0% ± 5.08% and average model recall of 78.0% ± 15.2% compared to manual selection. The precision and recall of the model were slightly affected by extremely poor image quality (Supplemental Figure S4.3B). The average particle diameter calculated using data predicted by the YOLOv7 CNN model showed similar average particle diameter that was measured using ImageJ, a common image analysis software. However, ImageJ occasionally select marginally aggregated particles, which would be removed during manual examination, leading to lower apparent particle selection or yield from micrographs (Supplemental Figure S4.3C and D). A large amount of studies that characterize HDL particle diameter or size from micrographs reported different levels of manual selection and user-specific procedures in the process [26,29]. The YOLOv7 model trained in this study can greatly reduce the tedious process. The improvement in particle sizing efficiency is critical if analysis of a large number of samples is needed.

Previous studies analyzed between 100 and a few hundred particles [21,46] when attempting to characterize the mean particle diameter from NS-TEM micrographs of HDL samples. HDL populations from clinical samples do not have a Gaussian distribution in diameter, and thus the sample size of particles to estimate population mean is likely larger than what has been analyzed previously. We showed in our sample size simulation experiment (Supplemental Figure 4.4) that at least 2,500 particles need to be selected and accurately measured from NS-TEM micrographs to obtain sample means that fall within 1% error of the population mean. Manual selection of more than 2,500 particles from each sample would take a considerable amount of time, whereas it is essentially instantaneous with the YOLOv7 model prediction.

To demonstrate the utility and applicability of the method, the method was applied to a large clinical sample set from age-matched individuals diagnosed with AD and MCI compared

with Control participants with *APOE* ε3ε3 or *APOE* ε3ε4 genotype. HDL particle size as a clinical indicator for AD risk prediction has been a topic of interest for many years, but while some studies show an increased concentration of small HDL in *APOE* ε4 allele carriers being protective against AD [10], other studies show increased small HDL particle concentrations are positively correlated with CVD, a common comorbidity of AD [47]. In the current analysis we found an increase in the smallest HDL particles and concomitant decrease in medium- and large-HDL particles in the AD and MCI groups compared to Controls, which resembles the particle size distribution pattern often observed in patients with metabolic syndrome [48 49] and coronary heart disease (CHD) [50].

We previously reported that both HDL CEC and LCAT activity in individuals with AD compared to Control were decreased in those with the *APOE* ε3ε3 genotype whereas CEC was paradoxically increased in AD patients with the *APOE* ε3ε4 genotype, possibly due to the fact that these *APOE* ε3ε4 AD patients had more small HDL particles, which would have meant a higher dose of total particles in the CEC assay [32]. The results of this study corroborate this observation. Small particles (diameter ≤ 9.5) were negatively associated with HDL functions in individuals in the *APOE* ε3ε3 group, while most of the particles in that range were positively associated with HDL functions in the *APOE* ε3ε4 group. The H3P particle size subclass is the most abundant, representing between 20% - 30% of total HDL particles analyzed. This subclass has been reported to be enriched in ApoJ, ApoL-1, ApoF, PON 1/3, phospholipid transfer protein, and platelet-activating factor acetyl hydrolase, and has been found to be protective against low-density lipoprotein oxidation [6,51]. Studies have reported a negative association between the amount of medium HDL particles (8.2 nm – 8.8 nm) and risk of coronary heart disease [50]. However, these normally protective H3P particles were increased in *APOE* ε3ε3 individuals with

AD/MCI compared with Control. One possibility is that *APOE* ε3ε3 AD/MCI patients have more of these usually protective H3P HDL, but they are dysfunctional. This possibility is supported by our previous finding that among individuals with AD/MCI, both CEC and LCAT activity were decreased specifically in *APOE* ε3ε3 but not *APOE* ε3ε4 compared to Control [32].

The abundance of HDL subclasses was also associated with cognitive measures. The abundance of the most abundant HDL particle size group, H3P, in the *APOE* ε3ε3 individuals showed the highest negative correlations with cognitive health. On the other hand, the abundance of the smallest two HDL subclasses, H1P and H2P, showed negative correlations with cognitive performance in the *APOE* ε3ε4 group. It was previously published that the abundance of "small HDL" was positively associated with cognitive function [10,52], an observation that at first glance contradicts our findings. However, the "small HDL" subclass as measured by ion mobility encompasses particles 7.0 nm – 10.5 nm in diameter, which represent as many as 75-80% of total HDL, and includes H1P, H2P, H3P and H4P particles in our analysis. While the smallest H1P and H2P particles were increased in those with AD, the medium size H3P (in *APOE* ε3ε3 only) and H4P (in *APOE* ε3ε4 only) particles were decreased in dementia patients compared to the Control group. Since the H3P and H4P particles together represent more than 40% of total HDL particles, whereas H1P and H2P particles represent about 20% to 30% of total HDL particles, our findings do not contradict the previous findings, but instead find variation within the finer size range that was not observed previously, a feature that is enabled by the granulated data provided by particle selection from NS-TEM micrographs.

We calculated the HDL particle diameter distribution similarity index to better understand whether dementia diagnosis and/or *APOE* genotype were important factors in HDL particle size distribution. A more consistent HDL particle diameter profile among a group of individuals

would be expected if there was a common underlying HDL size-modifying metabolic driver. Patients with AD/MCI had more similar HDL size distribution patterns than the Control group, and participants with *APOE* ε3ε4 genotype had more similar HDL size distribution patterns than those with *APOE* ε3ε3 genotype (Figure 4.5).

Together these data suggest that there are fundamental differences in both the HDL particle size distribution and how the HDL particles of different sizes are linked with cognitive outcomes among individuals with different *APOE* genotypes.

In summary, we utilized the YOLOv7 CNN model to select HDL particles from NS-TEM micrographs as a novel way to characterize HDL particle diameter. We demonstrated the utility of this method by examining the diameter data of more than 1.8 million individual HDL particles from 183 clinical samples obtained from study participants with normal cognition, MCI, or AD. The current results highlight the utility of the approach using NS-TEM coupled with a machine learning based image analysis model to discover HDL particle size distribution patterns and changes that are differentially correlated with multiple measures of cognitive function in a large clinical cohort of age-matched individuals. These results highlight the utility of the method described here for the discovery of biomarkers and disease mechanisms.

6. SUPPLEMENTAL INFORMATION

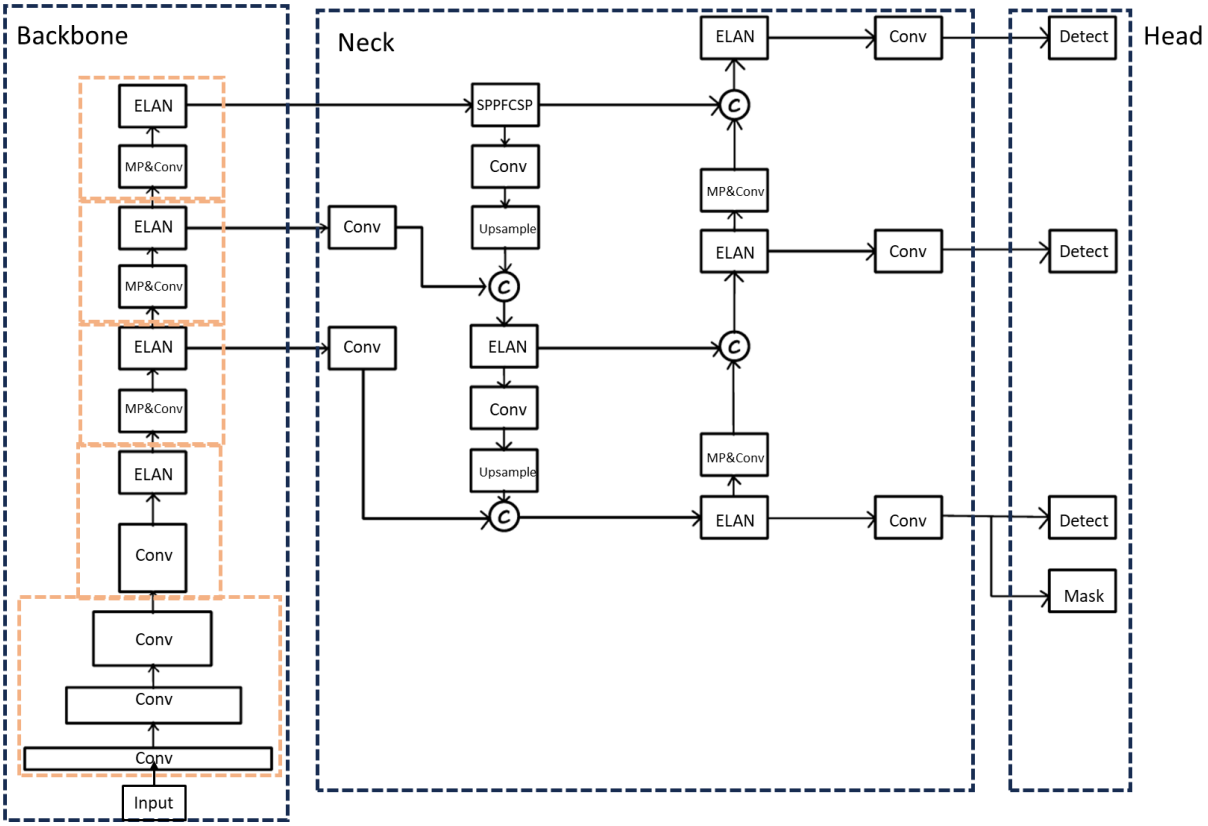

Figure S4.1. YOLOv7 CNN architecture used in the current study. Conv: a convolutional block comprising a convolution layer, a batch normalization layer, and an activation layer. ELAN: Efficient Layer Aggregation Network block, which integrates VoVNet with CSPNet. The feature maps generated from the ELAN blocks within the backbone architecture were transmitted to the Neck architecture for further processing. PANet: Path Aggregation Network. SPPFCSP: the spatial pyramid pooling fast cross stage partial network, a combination of spatial pyramid pooling fast (SPPF) and cross stage partial network (CSPNet). MP&Conv: a downsampling block consisting of a max pooling layer and convolution blocks. The features extracted from the Neck architecture were forwarded to the Head architecture for the prediction of object confidence, object classification, bounding box estimation, and segmentation.

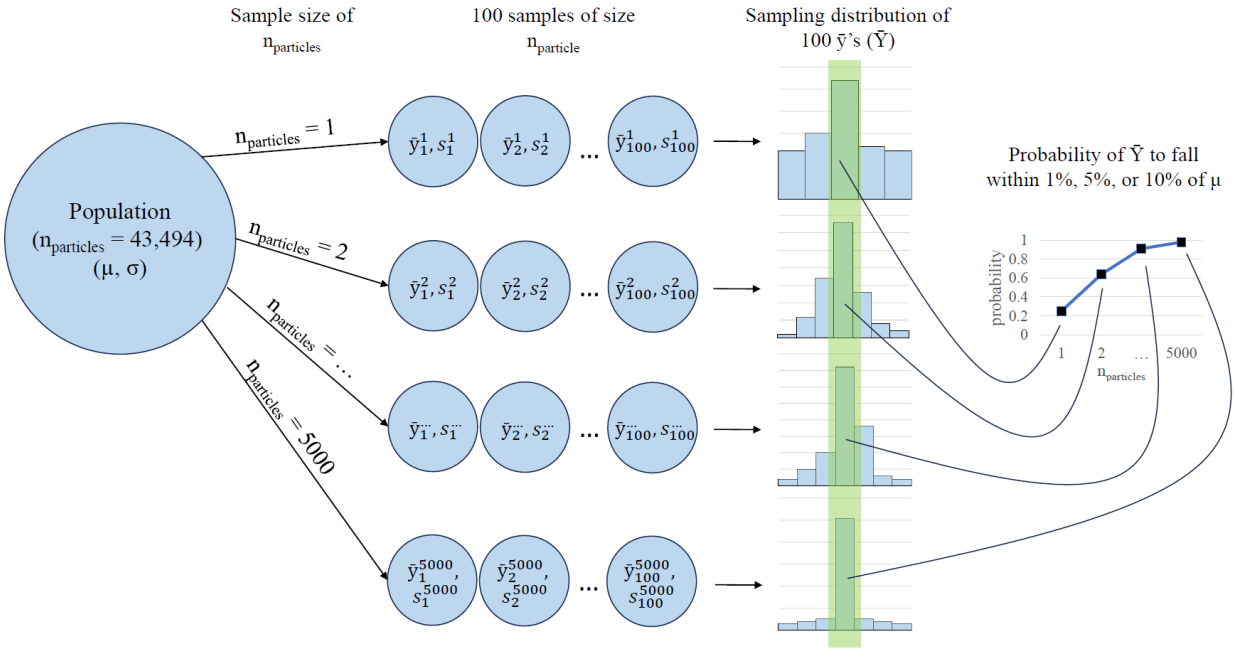

Figure S4.2. Method for HDL particle sample size simulation. Sample size ($n_{(particles)}$) from $n_{(particles)} = 1$ to $n_{(particles)} = 5000$ were randomly sampled 100 times from the population of 43,494 particles with replacement. The mean diameter of particles in each sampling event ($\bar{y}_j^i$, i = sample size; j = random sampling iteration) was calculated and summarized into a vector of sample means ($\bar{Y}^i$, i = sample size). The probability of each $\bar{Y}^i$ to fall within 1%, 5%, or 10% deviation from the population mean (μ) was plotted.

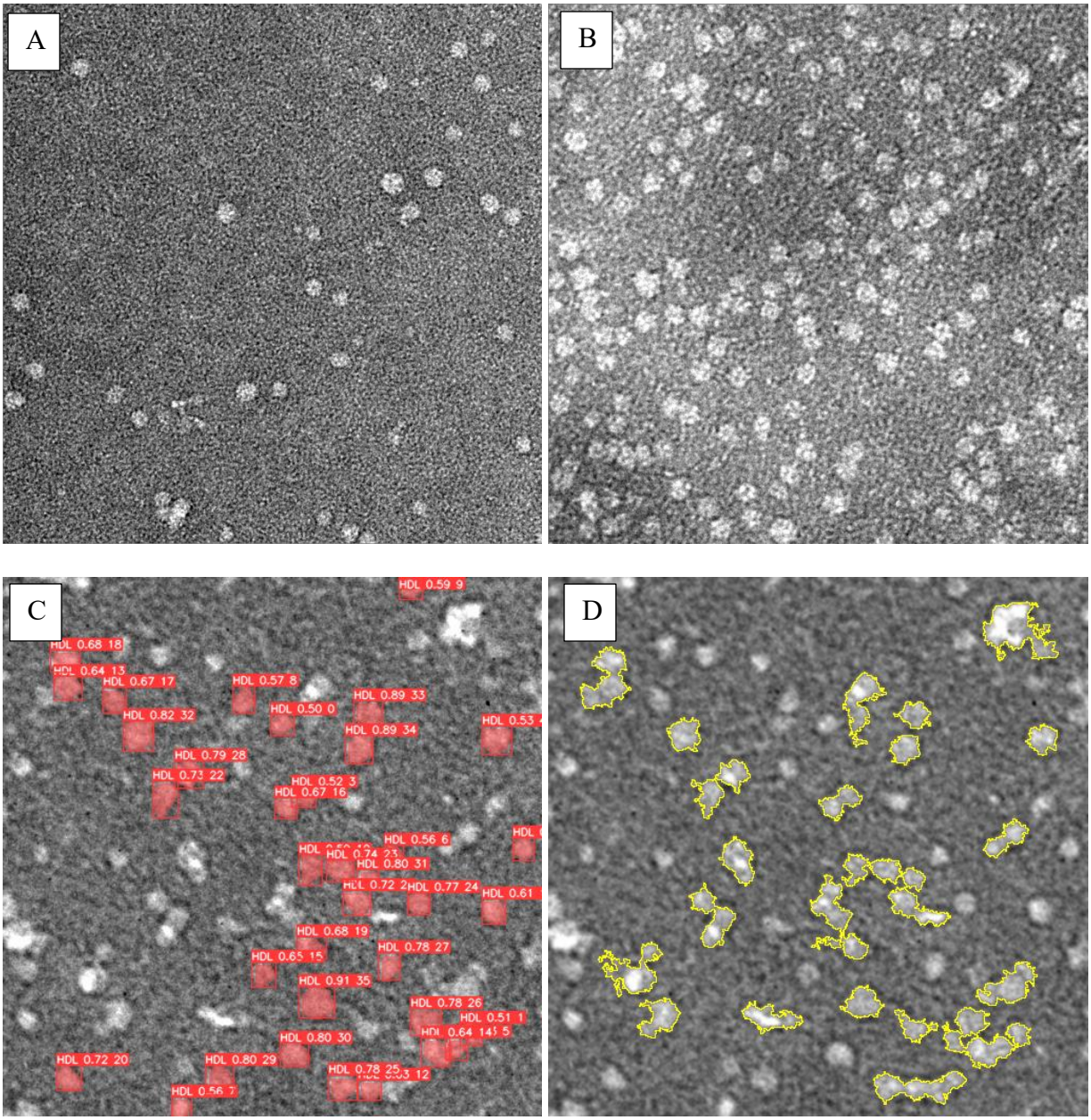

Figure S4.3. Sampled NS-TEM micrographs. (A) A normal-quality micrograph. (B) A poor-quality micrograph. (C) An example of particles predicted by the YOLOv7 model. (D) An example of particles predicted by ImageJ with the method described in this paper.

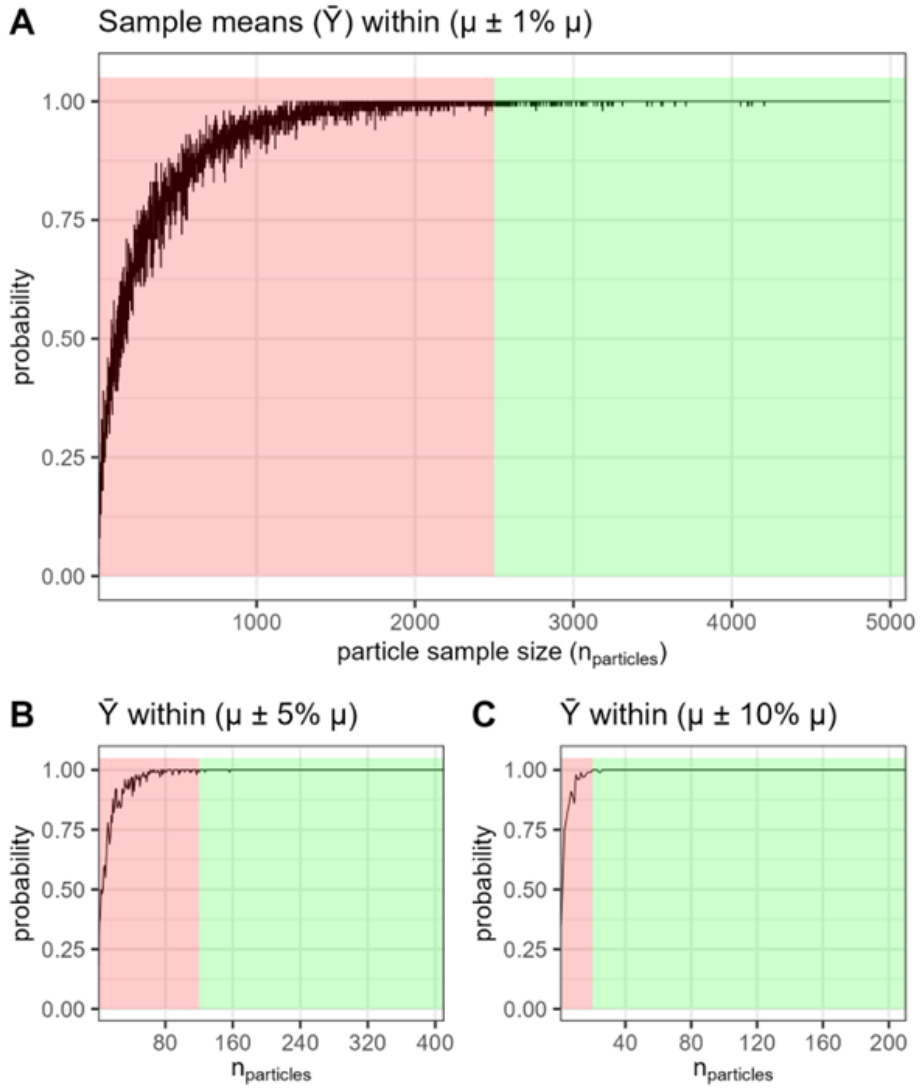

Figure S4.4. The probability of sample particle diameter means ($\bar{Y}$) to fall within A) 1% deviation, B) 5% deviation, or C) 10% deviation from the population particle diameter mean (μ) at various particle sample size ($n_{particle}$).

Table S4.1: Comparison of the HDL subgroup abundance percentage across dementia diagnoses.

HDL subgroup	HDL subgroup abundance percentage (%)			Post-hoc comparison adjusted p-value		
	Control	MCI	AD	Control vs. MCI	Control vs. AD	MCI vs. AD
All participants						
7.4 nm - 7.8 nm (H1P)	3.7 ± 2.8	7.3 ± 3.4	7.0 ± 3.2	****	****	N.S.
7.8 nm - 8.7 nm (H2P)	16 ± 9.1	24 ± 8	24 ± 8	****	****	N.S.
8.7 nm - 9.5 nm (H3P)	22 ± 7.1	23 ± 3	24 ± 2.9	N.S.	N.S.	N.S.
9.5 nm - 10.3 nm (H4P)	21 ± 4.3	17 ± 5	18 ± 4.0	****	***	N.S.
10.3 nm - 10.8 nm (H5P)	11 ± 4.2	7.6 ± 3.2	7.7 ± 3.0	****	****	N.S.
10.8 nm - 12.0 nm (H6P)	16 ± 9.7	11 ± 6	11 ± 5.2	***	***	N.S.
12.0 nm - 13.0 nm (H7P)	6.4 ± 5.1	4.2 ± 3.0	4.3 ± 3.4	N.S.	N.S.	N.S.
APOE E3E3						
7.4 nm - 7.8 nm (H1P)	4.0 ± 3.6	7.1 ± 3.3	4.3 ± 2.7	*	N.S.	N.S.
7.8 nm - 8.7 nm (H2P)	14 ± 11	25 ± 8	18 ± 7.7	**	N.S.	N.S.
8.7 nm - 9.5 nm (H3P)	17 ± 7.2	25 ± 2.7	24 ± 4.2	**	*	N.S.
9.5 nm - 10.3 nm (H4P)	19 ± 4.0	18 ± 5.4	21 ± 3.8	N.S.	N.S.	N.S.
10.3 nm - 10.8 nm (H5P)	11 ± 4.9	7.3 ± 3.3	10 ± 3.1	**	N.S.	N.S.
10.8 nm - 12.0 nm (H6P)	21 ±12	9.5 ± 4.5	14 ± 5.9	**	N.S.	N.S.
12.0 nm - 13.0 nm (H7P)	8.3 ±6.5	3.4 ± 1.9	6.4 ± 4.5	*	N.S.	N.S.
APOE E3E4						
7.4 nm - 7.8 nm (H1P)	3.4 ±2.0	7.5 ± 3.6	8.5 ± 2.3	****	****	N.S.
7.8 nm - 8.7 nm (H2P)	17 ± 7.1	23 ± 9	27 ± 5.2	*	****	N.S.
8.7 nm - 9.5 nm (H3P)	25 ± 5.0	22 ± 3.5	24 ± 2.1	*	N.S.	N.S.
9.5 nm - 10.3 nm (H4P)	23 ± 3.8	17 ± 4.9	16 ± 3.0	****	****	N.S.
10.3 nm - 10.8 nm (H5P)	10 ± 3.5	7.8 ± 3.3	6.4 ± 2.0	*	****	N.S.
10.8 nm - 12.0 nm (H6P)	13 ± 5.5	12 ± 6.6	8.8 ± 3.8	N.S.	*	N.S.
12.0 nm - 13.0 nm (H7P)	4.9 ±2.8	5.0 ± 3.8	3.2 ± 2.0	N.S.	N.S.	N.S.

Table S4.2. Spearman's correlation coefficient between HDL subclass abundance, HDL functional measurements, and participant clinical characteristics.

Parameters		HDL subclasses						
		7.4 nm - 7.8 nm (H1P)	**7.8 nm - 8.7 nm (H2P)**	**8.7 nm - 9.5 nm (H3P)**	**9.5 nm - 10.3 nm (H4P)**	**10.3 nm - 10.8 nm (H5P)**	**10.8 nm - 12.0 nm (H6P)**	**12.0 nm - 13.0 nm (H7P)**
APOE E3E3								
BMI	rho	0.07	0.11	0.13	0.00	-0.12	-0.11	-0.08
	adjusted p-value	0.15	0.16	0.13	0.23	0.19	0.20	0.19
Cholesterol efflux capacity	rho	-0.27	-0.23	-0.08	0.15	0.24	0.24	0.18
	adjusted p-value	0.01	0.01	0.01	0.06	0.01	0.01	0.01
Lecithin cholesterol acyltransferase activity	rho	-0.19	-0.24	-0.24	0.14	0.25	0.28	0.17
	adjusted p-value	0.00	0.00	0.01	0.03	0.00	0.00	0.00
Paraoxonase-1 activity	rho	-0.30	-0.33	-0.22	0.21	0.27	0.32	0.25
	adjusted p-value	0.00	0.00	0.00	0.02	0.00	0.00	0.00
Verbal memory Score	rho	-0.18	-0.19	-0.33	-0.04	0.21	0.22	0.15
	adjusted p-value	0.18	0.17	0.02	0.87	0.14	0.14	0.15
Executive Function Score	rho	-0.12	-0.13	-0.28	-0.05	0.16	0.18	0.11
	adjusted p-value	0.14	0.15	0.01	0.82	0.12	0.12	0.12
Semantic Memory Score	rho	0.19	0.19	-0.08	-0.32	-0.15	-0.14	-0.13
	adjusted p-value	0.03	0.03	0.60	0.00	0.05	0.05	0.05
Spatial Score	rho	-0.02	-0.02	-0.28	-0.22	0.05	0.05	0.00
	adjusted p-value	0.49	0.52	0.03	0.53	0.45	0.45	0.43
CDR Sum of Boxes	rho	0.11	0.16	0.45	0.10	-0.19	-0.23	-0.23
	adjusted p-value	0.13	0.13	0.00	0.79	0.10	0.10	0.10
White Matter Hyperintensity Volume	rho	0.32	0.33	0.38	-0.09	-0.31	-0.32	-0.32
	adjusted p-value	0.00	0.00	0.00	0.01	0.00	0.00	0.00
APOE E3E4								
BMI	rho	0.10	0.13	0.23	-0.06	-0.16	-0.15	-0.09
	adjusted p-value	0.02	0.01	0.10	0.04	0.01	0.02	0.04
	rho	0.24	0.16	-0.20	-0.25	-0.12	-0.05	-0.03

Cholesterol efflux capacity (CEC)	adjusted p-value	0.01	0.03	0.38	0.00	0.04	0.10	0.15
Lecithin cholesterol acyltransferase activity (LCAT)	rho	-0.02	0.05	0.29	0.08	-0.04	-0.13	-0.13
	adjusted p-value	0.87	0.44	0.02	0.91	0.48	0.28	0.21
Paraoxonase-1 activity (PON1)	rho	0.06	0.08	0.02	-0.03	-0.06	-0.10	-0.01
	adjusted p-value	0.01	0.01	0.34	0.01	0.01	0.01	0.01
Verbal memory Score (VMS)	rho	-0.58	-0.48	0.16	0.50	0.43	0.31	0.29
	adjusted p-value	0.00	0.00	0.80	0.00	0.00	0.01	0.01
Executive Function Score (EFS)	rho	-0.28	-0.26	0.15	0.26	0.20	0.12	0.11
	adjusted p-value	0.00	0.01	0.32	0.00	0.02	0.06	0.11
Semantic Memory Score	rho	-0.35	-0.37	0.01	0.39	0.34	0.20	0.09
	adjusted p-value	0.00	0.00	0.89	0.00	0.00	0.01	0.03
Spatial Score	rho	-0.22	-0.19	0.11	0.16	0.17	0.09	0.07
	adjusted p-value	0.00	0.01	0.68	0.00	0.01	0.04	0.07
CDR Sum of Boxes (CDRSOB)	rho	0.56	0.43	-0.27	-0.54	-0.39	-0.21	-0.21
	adjusted p-value	0.00	0.00	0.58	0.00	0.00	0.01	0.02
White Matter Hyperintensity Volume (WMHV)	rho	0.12	-0.01	-0.26	-0.08	0.03	0.12	0.13
	adjusted p-value	0.32	0.81	0.01	0.28	0.82	0.80	0.63

7. REFERENCES

1. Favari, E., Chroni, A., Tietge, U.J., Zanotti, I., Escolà-Gil, J.C., and Bernini, F. (2015). Cholesterol efflux and reverse cholesterol transport. High Density Lipoproteins Biol. Underst. Clin. Exploit., 181–206.
2. Kingwell, B.A., Chapman, M.J., Kontush, A., and Miller, N.E. (2014). HDL-targeted therapies: progress, failures and future. Nat. Rev. Drug Discov. *13*, 445–464.
3. Nikolic, D., Katsiki, N., Montalto, G., Isenovic, E.R., Mikhailidis, D.P., and Rizzo, M. (2013). Lipoprotein subfractions in metabolic syndrome and obesity: clinical significance and therapeutic approaches. Nutrients *5*, 928–948.
4. Stenkula, K.G., Lindahl, M., Petrlova, J., Dalla-Riva, J., Göransson, O., Cushman, S.W., Krupinska, E., Jones, H.A., and Lagerstedt, J.O. (2014). Single injections of apoA-I acutely improve in vivo glucose tolerance in insulin-resistant mice. Diabetologia *57*, 797–800.
5. Rizzo, M., Otvos, J., Nikolic, D., Montalto, G., Toth, P., and Banach, M. (2014). Subfractions and subpopulations of HDL: an update. Curr. Med. Chem. *21*, 2881–2891.
6. Rosenson, R.S., Brewer Jr, H.B., Chapman, M.J., Fazio, S., Hussain, M.M., Kontush, A., Krauss, R.M., Otvos, J.D., Remaley, A.T., and Schaefer, E.J. (2011). HDL measures, particle heterogeneity, proposed nomenclature, and relation to atherosclerotic cardiovascular events. Clin. Chem. *57*, 392–410.
7. Johansson, J., Carlson, L.A., Landou, C., and Hamsten, A. (1991). High density lipoproteins and coronary atherosclerosis. A strong inverse relation with the largest particles is confined to normotriglyceridemic patients. Arterioscler. Thromb. J. Vasc. Biol. *11*, 174–182.
8. Berneis, K.K., and Krauss, R.M. (2002). Metabolic origins and clinical significance of LDL heterogeneity. J. Lipid Res. *43*, 1363–1379. 10.1194/jlr.R200004-JLR200.
9. Davidson W. Sean, Silva R.A. Gangani D., Chantepie Sandrine, Lagor William R., Chapman M. John, and Kontush Anatol (2009). Proteomic Analysis of Defined HDL Subpopulations Reveals Particle-Specific Protein Clusters. Arterioscler. Thromb. Vasc. Biol. *29*, 870–876. 10.1161/ATVBAHA.109.186031.
10. Martinez, A.E., Weissberger, G., Kuklenyik, Z., He, X., Meuret, C., Parekh, T., Rees, J.C., Parks, B.A., Gardner, M.S., and King, S.M. (2022). The small HDL particle hypothesis of Alzheimer's disease. Alzheimers Dement.
11. Nelson, T.J., and Sen, A. (2019). Apolipoprotein E particle size is increased in Alzheimer's disease. Alzheimers Dement. Diagn. Assess. Dis. Monit. *11*, 10–18.
12. Anderson, D., Nichols, A., Pan, S., and Lindgren, F. (1978). High density lipoprotein distribution: resolution and determination of three major components in a normal population sample. Atherosclerosis *29*, 161–179.
13. Collins, L.A., and Olivier, M. (2010). Quantitative comparison of lipoprotein fractions derived from human plasma and serum by liquid chromatography-tandem mass spectrometry. Proteome Sci. *8*, 42. 10.1186/1477-5956-8-42.
14. Asztalos, B.F., Cupples, L.A., Demissie, S., Horvath, K.V., Cox, C.E., Batista, M.C., and Schaefer, E.J. (2004). High-density lipoprotein subpopulation profile and coronary heart disease prevalence in male participants of the Framingham Offspring Study. Arterioscler. Thromb. Vasc. Biol. *24*, 2181–2187.

15. Asztalos, B.F., Sloop, C.H., Wong, L., and Roheim, P.S. (1993). Two-dimensional electrophoresis of plasma lipoproteins: recognition of new apo AI-containing subpopulations. Biochim. Biophys. Acta BBA-Lipids Lipid Metab. *1169*, 291–300.
16. Forte, T.M., and Nordhausen, R.W. (1986). [26] Electron microscopy of negatively stained lipoproteins. Methods Enzymol. *128*, 442–457.
17. Jeyarajah, E.J., Cromwell, W.C., and Otvos, J.D. (2006). Lipoprotein particle analysis by nuclear magnetic resonance spectroscopy. Clin. Lab. Med. *26*, 847–870.
18. Caulfield, M.P., Li, S., Lee, G., Blanche, P.J., Salameh, W.A., Benner, W.H., Reitz, R.E., and Krauss, R.M. (2008). Direct determination of lipoprotein particle sizes and concentrations by ion mobility analysis. Clin. Chem. *54*, 1307–1316.
19. Sakurai, T., Trirongjitmoah, S., Nishibata, Y., Namita, T., Tsuji, M., Hui, S.-P., Jin, S., Shimizu, K., and Chiba, H. (2010). Measurement of lipoprotein particle sizes using dynamic light scattering. Ann. Clin. Biochem. *47*, 476–481.
20. Kim, H.-A., Seo, J.-K., Kim, T., and Lee, B.-T. (2014). Nanometrology and its perspectives in environmental research. Environ. Health Toxicol. *29*.
21. Zhang, L., Song, J., Newhouse, Y., Zhang, S., Weisgraber, K.H., and Ren, G. (2010). An optimized negative-staining protocol of electron microscopy for apoE4• POPC lipoprotein. J. Lipid Res. *51*, 1228–1236.
22. Wrigley, N.G. (1968). The lattice spacing of crystalline catalase as an internal standard of length in electron microscopy. J. Ultrastruct. Res. *24*, 454–464.
23. Kondo, A., Muranaka, Y., Ohta, I., and Kanno, T. (1999). Dynamic reaction in a homogeneous HDL-cholesterol assay visualized by electron microscopy. Clin. Chem. *45*, 1974–1980.
24. Zhu, L., Petrlova, J., Gysbers, P., Hebert, H., Wallin, S., Jegerschöld, C., and Lagerstedt, J.O. (2017). Structures of apolipoprotein AI in high density lipoprotein generated by electron microscopy and biased simulations. Biochim. Biophys. Acta BBA-Gen. Subj. *1861*, 2726–2738.
25. Nanjee, M., Cooke, C., Wong, J., Hamilton, R., Olszewski, W., and Miller, N. (2001). Composition and ultrastructure of size subclasses of normal human peripheral lymph lipoproteins: quantification of cholesterol uptake by HDL in tissue fluids. J. Lipid Res. *42*, 639–648.
26. Cabana, V., Lukens, J., Rice, K.S., Hawkins, T.J., and Getz, G. (1996). HDL content and composition in acute phase response in three species: triglyceride enrichment of HDL a factor in its decrease. J. Lipid Res. *37*, 2662–2674.
27. Zheng, J.J., Agus, J.K., Hong, B.V., Tang, X., Rhodes, C.H., Houts, H.E., Zhu, C., Kang, J.W., Wong, M., and Xie, Y. (2021). Isolation of HDL by sequential flotation ultracentrifugation followed by size exclusion chromatography reveals size-based enrichment of HDL-associated proteins. Sci. Rep. *11*, 1–15.
28. Kavo, A.E., Rallidis, L.S., Sakellaropoulos, G.C., Lehr, S., Hartwig, S., Eckel, J., Bozatzi, P.I., Anastasiou-Nana, M., Tsikrika, P., and Kypreos, K.E. (2012). Qualitative characteristics of HDL in young patients of an acute myocardial infarction. Atherosclerosis *220*, 257–264.
29. Mallol, R., Rodríguez, M.A., Heras, M., Vinaixa, M., Plana, N., Masana, L., Morris, G.A., and Correig, X. (2012). Particle size measurement of lipoprotein fractions using diffusion-ordered NMR spectroscopy. Anal. Bioanal. Chem. *402*, 2407–2415.
30. Zvintzou, E., Skroubis, G., Chroni, A., Petropoulou, P.-I., Gkolfinopoulou, C., Sakellaropoulos, G., Gantz, D., Mihou, I., Kalfarentzos, F., and Kypreos, K.E. (2014).

Effects of bariatric surgery on HDL structure and functionality: results from a prospective trial. J. Clin. Lipidol. *8*, 408–417.
31. Hinton, L., Carter, K., Reed, B.R., Beckett, L., Lara, E., DeCarli, C., and Mungas, D. (2010). Recruitment of a community-based cohort for research on diversity and risk of dementia. Alzheimer Dis. Assoc. Disord. *24*, 234.
32. Hong, B.V., Zheng, J., Agus, J.K., Tang, X., Lebrilla, C.B., Jin, L.-W., Maezawa, I., Erickson, K., Harvey, D.J., and DeCarli, C.S. (2022). High-Density Lipoprotein Changes in Alzheimer's Disease Are APOE Genotype-Specific. Biomedicines *10*, 1495.
33. Mungas, D., Reed, B.R., Marshall, S.C., and González, H.M. (2000). Development of psychometrically matched English and Spanish language neuropsychological tests for older persons. Neuropsychology *14*, 209.
34. Mungas, D., Reed, B.R., Crane, P.K., Haan, M.N., and González, H. (2004). Spanish and English Neuropsychological Assessment Scales (SENAS): further development and psychometric characteristics. Psychol. Assess. *16*, 347.
35. DeCarli, C., Maisog, J., Murphy, D.G., Teichberg, D., Rapoport, S.I., and Horwitz, B. (1992). Method for quantification of brain, ventricular, and subarachnoid CSF volumes from MR images. J. Comput. Assist. Tomogr. *16*, 274–284.
36. Zhang, L., Tong, H., Garewal, M., and Ren, G. (2013). Optimized negative-staining electron microscopy for lipoprotein studies. Biochim. Biophys. Acta BBA-Gen. Subj. *1830*, 2150–2159.
37. Wang, C.-Y., Bochkovskiy, A., and Liao, H.-Y.M. (2023). YOLOv7: Trainable bag-of-freebies sets new state-of-the-art for real-time object detectors. In, pp. 7464–7475.
38. Wang, C.-Y., Liao, H.-Y.M., and Yeh, I.-H. (2022). Designing network design strategies through gradient path analysis. ArXiv Prepr. ArXiv221104800.
39. Liu, S., Qi, L., Qin, H., Shi, J., and Jia, J. (2018). Path aggregation network for instance segmentation. In, pp. 8759–8768.
40. Lin, T.-Y., Maire, M., Belongie, S., Hays, J., Perona, P., Ramanan, D., Dollár, P., and Zitnick, C.L. (2014). Microsoft coco: Common objects in context. In (Springer), pp. 740–755.
41. Schneider, C.A., Rasband, W.S., and Eliceiri, K.W. (2012). NIH Image to ImageJ: 25 years of image analysis. Nat. Methods *9*, 671–675.
42. Holzer, M., Zangger, K., El-Gamal, D., Binder, V., Curcic, S., Konya, V., Schuligoi, R., Heinemann, A., and Marsche, G. (2012). Myeloperoxidase-derived chlorinating species induce protein carbamylation through decomposition of thiocyanate and urea: novel pathways generating dysfunctional high-density lipoprotein. Antioxid. Redox Signal. *17*, 1043–1052.
43. Carugo, O. (2003). How root-mean-square distance (rmsd) values depend on the resolution of protein structures that are compared. J. Appl. Crystallogr. *36*, 125–128.
44. R Core Team, R. (2013). R: A language and environment for statistical computing.
45. Benjamini, Y., and Hochberg, Y. (1995). Controlling the false discovery rate: a practical and powerful approach to multiple testing. J. R. Stat. Soc. Ser. B Methodol. *57*, 289–300.
46. Huang, R., Silva, R.G.D., Jerome, W.G., Kontush, A., Chapman, M.J., Curtiss, L.K., Hodges, T.J., and Davidson, W.S. (2011). Apolipoprotein AI structural organization in high-density lipoproteins isolated from human plasma. Nat. Struct. Mol. Biol. *18*, 416–422.
47. Kontush, A. (2015). HDL particle number and size as predictors of cardiovascular disease. Front. Pharmacol. *6*, 218.

48. Dullaart, R.P., Otvos, J.D., and James, R.W. (2014). Serum paraoxonase-1 activity is more closely related to HDL particle concentration and large HDL particles than to HDL cholesterol in Type 2 diabetic and non-diabetic subjects. Clin. Biochem. *47*, 1022–1027.
49. Sokooti, S., Flores-Guerrero, J.L., Kieneker, L.M., Heerspink, H.J., Connelly, M.A., Bakker, S.J., and Dullaart, R.P. (2021). HDL particle subspecies and their association with incident type 2 diabetes: the PREVEND study. J. Clin. Endocrinol. Metab. *106*, 1761–1772.
50. Parish, S., Offer, A., Clarke, R., Hopewell, J.C., Hill, M.R., Otvos, J.D., Armitage, J., and Collins, R. (2012). Lipids and lipoproteins and risk of different vascular events in the MRC/BHF Heart Protection Study. Circulation *125*, 2469–2478.
51. Davidson, W.S., Silva, R.G.D., Chantepie, S., Lagor, W.R., Chapman, M.J., and Kontush, A. (2009). Proteomic analysis of defined HDL subpopulations reveals particle-specific protein clusters: relevance to antioxidative function. Arterioscler. Thromb. Vasc. Biol. *29*, 870–876.
52. Pedrini, S., Hone, E., Gupta, V.B., James, I., Teimouri, E., Bush, A.I., Rowe, C.C., Villemagne, V.L., Ames, D., and Masters, C.L. (2020). Plasma high density lipoprotein small subclass is reduced in Alzheimer's disease patients and correlates with cognitive performance. J. Alzheimers Dis. *77*, 733–744.